UNIVERSITY OF TURIN
Università degli Studi di Torino

DOCTORAL SCHOOL
Scuola di Dottorato in Scienza e Alta Tecnologia
Indirizzo: Fisica ed Astrofisica
XXIII Ciclo

P H D T H E S I S

Tesi di Dottorato di Ricerca

to obtain the title of

PhD of Science

of the University of Turin
Specialty : High Energy Physics

Defended by

Martin Alfonso Subieta Vasquez

Measurements of the μ^+/μ^- ratio for vertical and horizontal atmospheric muons with ALICE detector

Thesis Advisors: Prof. O. Saavedra
Dr. B. Alessandro

prepared at INFN Turin University, ALICE Team

defended on March 25th, 2011

Introduction

ALICE (A Large Ion Collider Experiment) is one of the four experiments of the LHC (Large Hadron Collider) at CERN. It is mainly dedicated to study a new phase of matter, called QGP (Quark Gluon Plasma), created in heavy-ion collisions at very high energies up to $\sqrt{s} = 14$ TeV. Although its main purpose is the study of QGP, it can also operate to detect atmospheric muons produced by meson decays ($\pi^{\pm}, \kappa^{\pm}$) at high altitudes in the atmosphere. The good capabilities of the ALICE detectors make possible very accurate measurements involving cosmic ray physics.

Since ALICE is located 40 m underground with 30 m of rock above (molasse), at this depth only muons with an energy larger than 15 GeV can reach the apparatus. The central detectors of ALICE : ACORDE (Alice COsmic Ray Detector), TOF (Time Of Flight), TPC (Time Projection Chamber) and SPD (Silicon Pixel Detector) have been employed to study the so-called *near-vertical muons*, namely, muons in the zenith angle range $0^o - 20^o$. In addition, with the Forward Muon Spectrometer (FMS) high energy muons with large zenith angles, within the range $70^o - 85^o$, and called *near-horizontal muons* have been detected and analysed.

In 2008 I have worked in the commissioning of the SDD (Silicon Drift Detector) of the ITS (Inner Tracking System), participating also in the cosmic data taking.

During the commissioning period (2008-2010), were taken a large amount of data with atmospheric muons in order to align and calibrate the various detectors of ALICE. A small sample of these data with the proper characteristics to perform studies on cosmic ray has been analysed by me.

Thereby, from the good quality of the data collected were distinguished three main event types: single muon events (one single muon track), multi-muon events (muon bundles) and muon interaction events (muon interacting with the iron magnet). All these type of events could be subject of further studies.

I have mainly focused on the research of single muon events in order to study the charge muon ratio which is one of the most important measurements connecting cosmic rays and particle physics. In this thesis, the analysis to measure the muon charge ratio for *near-vertical muons* and *near-horizontal muons* is discussed in detail, and the results are compared with other measurements.

In the first and second chapter is given a brief description of cosmic ray physics with emphasis on measurements performed with apparatus designed for accelerator experiments.

The third chapter summarizes the general characteristics of the ALICE detectors involved in the analysis, while in the fourth is given a detailed description of the

tracking performances of these detectors for atmospheric muons.

In the fifth chapter the muons detected in the central barrel of ALICE are analysed. The muon multiplicity distribution and the angular directions of all the data have been studied, as a preliminary work, to demonstrate the capabilities in the reconstruction of the muons. Then, a sample of single muon events has been analysed for the measurement of the ratio between positive and negative muons.

The sixth chapter is focused on the Forward Muon Spectrometer for the detection of *near-horizontal muons* and the μ^+/μ^- ratio measurement at surface level.

Finally, our results concerning *near-vertical muons* are compared with the recent muon ratio measurements done by the CMS (Compact Muon Solenoid) experiment at LHC and previously by the L3+C experiment at LEP. Moreover, *near-horizontal muons* ratio measurements at surface level are compared with old measures done by MUTRON experiment.

Acknowledgments

The present thesis is the result of arduous work's years at the prestigious University of Turin (Università Degli Studi di Torino) and INFN (istituto Nucleare di Fisica), Italy. By the participation in ALICE experiment through the Italian team, was possible to carry out the very important program of the ALICE experiment concerning cosmic ray physics.

I am very happy to participate in one of the four big experiments at LHC, CERN. The experience and new knowledge acquired will be very useful in my future researches.

I would like to thank all people of the ALICE team, and specially to my tutor Alessandro Bruno, for his support and very useful suggestions during the last three years of my PhD.

I do not have enough words to thank professor Oscar Saavedra for his continuous help and support, thank you very much dear professor to believe in me. Finally, I would like to thank to my family, whose in spite to the very large distance between Italy and Bolivia, they always gave me all their love and support when I needed, and specially to my wife for her continuous love and support.

Contents

Chapter 1

Cosmic Ray Physics

Contents

In this chapter some general topics of cosmic rays physics will be briefly described. We will focus in the production of muons in the atmosphere by decay of hadronic showers created in the interactions of primary cosmic rays with atmosphere nuclei. Furthermore, the final section is dedicated to describe the recently muon charge ratio studies done, in particular by MINOS and OPERA experiments.

1.1 Introduction

Cosmic rays are ionized atomic nuclei with lifetimes of order 10^6 years or longer, which reach the upper atmosphere of the Earth from outside of the solar system. Although already discovered in 1912 by V. F. Hess during several ascends with hydrogen-filled balloons up to altitudes of 5 km, their sources and propagation mechanisms are still a subject of research.

The solar system is permanently exposed to a flux of these cosmic rays where their energies extend from the MeV range to at least 10^{20} eV. The energy spectrum (see Fig. 1.1) falls steeply as a function of the energy, decreasing by a factor 500 per decade in energy. The flux also decreases from more than 100 particles per second and square meter at GeV energies to about one particle per m^2 and per year at a PeV, and further to less than one particle per km^2 and per century above 100 EeV.

The energy spectrum follows a power law $dN/dE \propto E^{\gamma}$ over a wide energy range. The index of the spectrum is $\gamma \approx$ -2.7 at energies up to several PeV. After a steepening is observed, the so-called *knee*, where the index is $\gamma \approx$ -3.1 at higher energies. A further steepening, beginning the second *knee*, occurs around $4{\times}10^{17}$ eV. And finally, at $\sim 4{\times}10^{18}$ eV, at the so-called *ankle*, the spectrum flattens again (see Fig. 1.1).

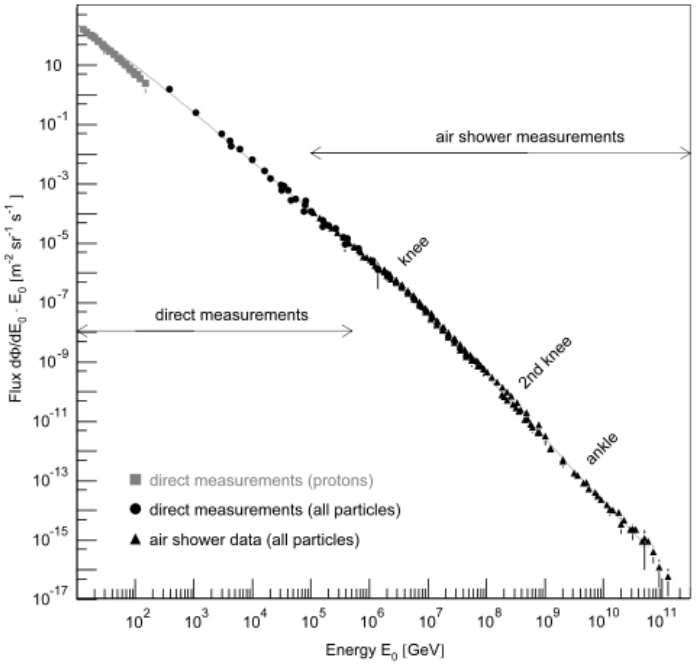

Figure 1.1: All-particle energy spectrum of cosmic rays. The data was measured directly with detectors above the atmosphere as well as with air shower detectors [Blümer 2009].

Furthermore, the energy spectrum obtained by direct measurements above the atmosphere by ATIC [Ahn 2003], PROTON [Grigorov 1970], and RUNJOB [Derbina 2005] experiments are shown in the Fig. 1.2. Also are shown results from air shower experiments in comparison with hadronic interaction models like Tibet ASγ with SIBILL 2.1 [Amenomori 2008], KASCADE with QGSJET01 [Antoni 2005], KASCADE-GRANDE [Arteaga-Velazques 2008] and Akeno data [Nagano 1984]. At high energies the measurements are presented by HiRes-MIA [Abu-Zayyad 2001],[Abu-Zayyad 2000], Hires I and II [Abbasi 2008] and Auger [Abraham 2008] experiments. In addition, in the figure the energy is compared with the equivalent energy of the center of mass for p-p collisions $\sqrt{s_{pp}}$ in GeV.

Primary cosmic ray are near 79% free protons and about 70% of the remnant are nucleons bound in the helium muclei. The major components of the cosmic rays

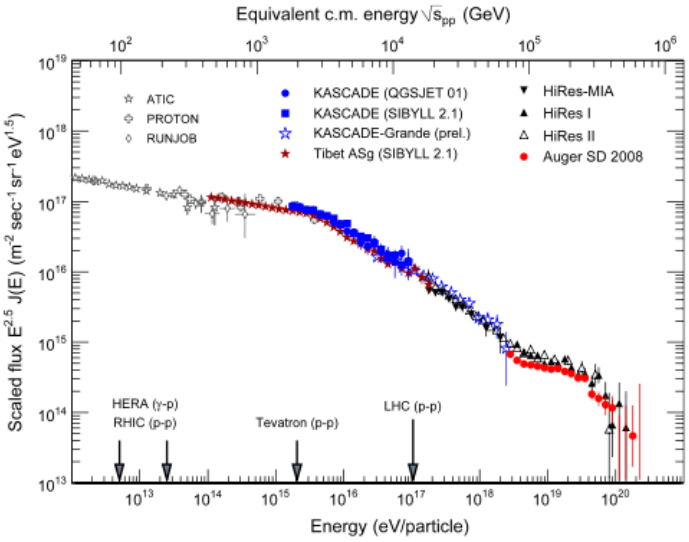

Figure 1.2: Energy spectrum of cosmic rays obtained from measurements above the atmosphere as well as from air shower experiments and comparison with some hadronic interaction models. The equivalent energy of the center of mass for p-p collisions in GeV is shown [Blümer 2009].

are shown in the Fig. 1.3 as a function of their kinetic energy per particle.

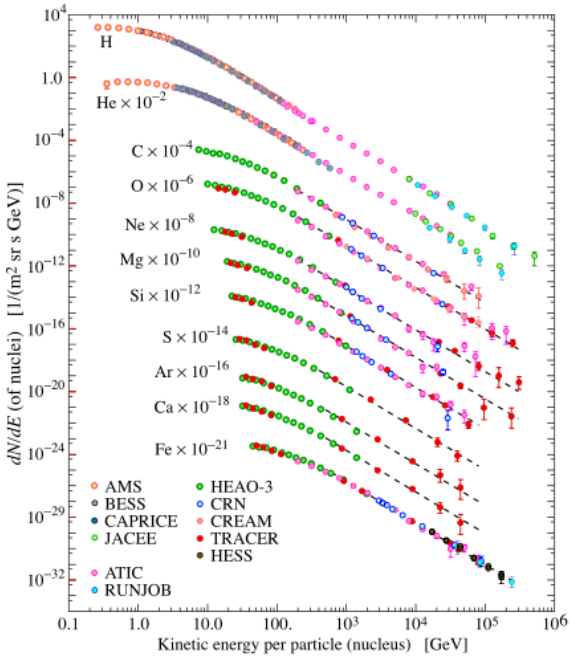

Figure 1.3: Major components of the primary cosmic radiation [Gaisser 2007].

1.2 Cosmic rays at the atmosphere

In the Fig. 1.4 is shown the vertical fluxes of the cosmic ray components in the atmosphere in the energy region where the particles are most numerous. All particles are secondaries produced from interactions of the primary cosmic rays with the air nuclei, except for protons and electrons near the top of the atmosphere. The decay of charged mesons are muons and neutrinos, while electrons and photons are produced in decays of neutral mesons. Thus showers initiated by electrons or photons are called electromagnetic showers.

Electromagnetic showers (EMS) are governed mainly by the particle production processes as bremsstrahlung of electrons and pair production of electrons-positrons by photons. Some properties of it can be understood within the very simple model of Heitler [Heitler 1944]. Such model assumes that the incoming particle interacts with the atmosphere nuclei after travelling a certain depth λ_{ems} and produces two new particles with half the energy of the initial particle. Then these new particles interact again at a distance λ_{ems} from their production point. After n generations of successive interactions the number of the particles would be 2^n. Thus the number of the particles as a function of depth X is $N(X) = 2^{X/\lambda_{ems}}$. The production of new particles continues till the energy of the secondary particles is smaller than their critical energy E_c, where absorption processes arise below E_c. The maximum number of particles in the shower will be $N_{max} = E_o/E_c$ and the depth of the shower maximum is given by $X_{max} = \lambda_{ems} \log(E_o/E_c)$, where E_o is the primary particle energy.

Although Heitler's model is simplified, it gives two important features. The number of particles at shower maximum is approximately proportional to the primary energy and the depth of the shower increases logarithmically with energy.

The differences between photon and hadron initiated showers are mainly related to the fact that hadronic showers develop a significant muon component, whereas there are few muons in purely EMS.

Hadronic showers (HS) can be modeled with a similar to that from Heitler's model in order to understand the basic properties of hadronic showers [Matthews 2005]. Hadronic interaction of a particle with energy E produces N_{tot} new particles with energy E/N_{tot}, two thirds of which being charged particles N_{ch} (charged pions) and one third being neutral particles N_{neu} (neutral pions). Neutral particles decay suddenly into electromagnetic particles ($\pi^o \rightarrow 2\gamma$). Charged particles interact again with the air nuclei if their energy is greater than their decay energy E_d or decay otherwise. Thus the number of generations of the hadronic interactions n, follows from $E_d = E_o/(N_{tot})^n$. Then if we considering that one muon is produced in the decay of each charged $\pi^{\pm}$, we can write the following relation:

$$N_\mu = (N_{ch})^n = \left(\frac{E_o}{E_d}\right)^\alpha , \tag{1.1}$$

where $\alpha = \ln N_{ch}/\ln N_{tot} \approx 0.86....0.93$. This numerical values of α and E_d depend on the muon energy thresholds, which are given in Ref. [Alvarez 2002] for different hadronic interaction models. The number of muons produced in an air shower increases almost linearly with the primary energy and also of the air density, on the other hand, the charged and the number of particles (i.e. muon multiplicities) depends of the hadronic interactions.

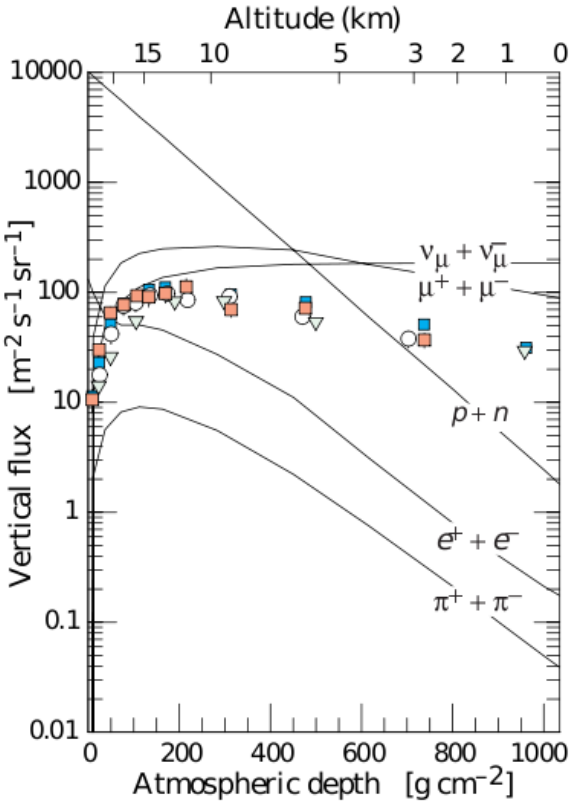

Figure 1.4: Cosmic rays in the atmosphere at vertical direction for $E > 1$ GeV estimated from the nucleon flux. The points show measurements of negative muons with $E_\mu > 1$ GeV [Gaisser 2007].

Most measurements of cosmic rays in atmosphere are made at ground level and also at the top of the atmosphere (as seen in the previous section), but there are also measurements of muons and electrons made in airplanes and balloons. The Fig. 1.4 includes recent measurements of negative muons [Bellotti 1996, Bellotti 1999, Boezio 2000, Coutu 2000]. Since $\mu^+(\mu^-)$ are produced together with $\nu_\mu(\bar{\nu}_\mu)$, the measurement of muons from the parent pions serves to

calibrate the atmospheric ν_μ beam [Sanuki 2007]. The muons typically loss almost two GeV in passing through the atmosphere, the comparison near the production altitude is important in the Sub-GeV range of $\nu_\mu(\bar{\nu}_\mu)$ energies.

The flux of cosmic rays in the atmosphere is described by cascade equations with boundary conditions at the top of the atmosphere to match the primary spectrum. The decay and energy-loss processes, and the energy dependences of the cross section are described by numerical Monte Carlo calculations of the primary spectral index γ. Approximate analytic solutions are, however, useful in limited regions of energy [Gaisser 1990, Lipari 1993].

1.3 Cosmic rays at the surface

1.3.1 Electromagnetic component

The component consisting of electrons, positrons, and photons which arose from electromagnetic cascades initiated by decay of neutral is at the ground the electromagnetic component. Muon decay is the dominant source of low-energy electrons at sea level. Due to decay of neutral pions is very short its contribution are more important at high altitude or when the energy threshold is high. Knock-on electrons due to the passage of muons through atmosphere give a small contribution at low energy [Hayakawa 1969]. The integral vertical intensity of electrons plus positrons is near 30, 6, and 0.2 $m^{-2}s^{-1}sr^{-1}$ above 10, 100, and 1000 MeV respectively [Grieder 2001, Daniel 1974], but it depends on altitude, and the angular dependence is complex because of the different altitude dependence of the different sources of electrons [Hayakawa 1969, Beuermann 1968]. The ratio of photons to electrons plus positrons is approximately 1.3 above 1 GeV and 1.7 below the critical energy [Beuermann 1968]. This ratio depends on the altitude and on the primaries energies.

1.3.2 Hadronic component

The primary cosmic radiation passing through the atmosphere interact with the air nuclei in consequence they loss energy, then nucleons above 1 GeV are the remnant of the primaries. At this energy the intensity is approximately $I_N(E,0) \times e^{-X/\cos\theta\Lambda}$ for $\theta < 70°$. At sea level, also neutrons produced by successive cascades are 1/3 of the nucleons in the vertical direction. The integral intensity of vertical protons above 1 GeV/c at sea level is $\approx 0.9\ m^{-2}s^{-1}sr^{-1}$ [Grieder 2001, Diggory 1974].

1.3.3 Muonic component

High energy muons are produced mainly at high altitude in the atmosphere ($\sim$ 15 Km) while intermediate and low energy muons are created at lower altitude and consist the most important component at the ground level. A muon passing through the whole atmosphere loss $\sim$ 2 GeV by ionization. The energy and angular distribution

of the muons at ground level reflect a convolution of production spectrum, energy loss in the atmosphere, and decay. The mean energy of the muons at the ground is ≈ 4 GeV. The energy spectrum is almost flat below 1 GeV and reflects the primary spectrum in the 10-100 GeV range, while the spectrum appears to be much more steep at higher energies, because pions with $E_\pi > \varepsilon_\pi$(critical energy) tend to interact in the atmosphere rather than decay. Asymptotically ($E_\mu > 1$ TeV), the index of the energy spectrum of atmospheric muons is $\gamma + 1$ where γ is the primary spectrum index. The integral intensity of vertical muons above 1 GeV/c momentum at sea level is 70 $m^{-2}s^{-1}sr^{-1}$ [Pascale 1993, Grieder 2001], with recent measurements [Kremer 1999, Archard 2004] that tend to give lower normalization by 10-15%. We can take this number in the form $I \approx 1\ cm^{-2}min^{-1}$ for horizontal detectors. The overall angular distribution of muons at the ground is $\propto \cos^2\theta$, which is characteristic of muons with $E_\mu \sim 3$ GeV. The angular distribution at lower energies becomes more steeply, while at higher energy it approach to $\sec\theta$ distribution for $E_\mu \gg \varepsilon_\pi$ and $\theta < 70°$.

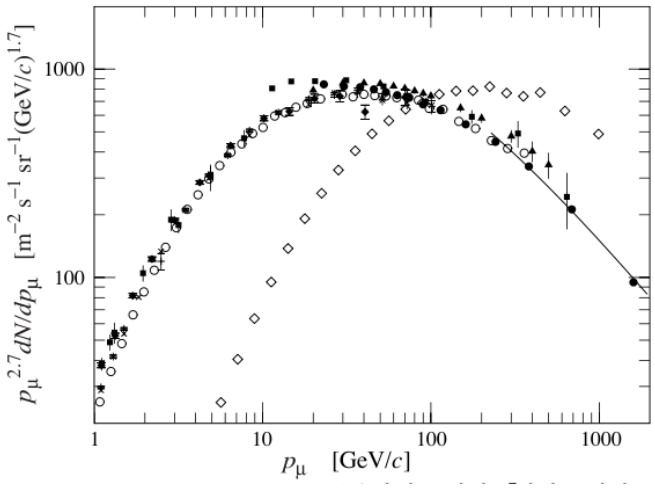

Figure 1.5: Spectrum of muons at $\theta = 0^0$ (⧫ [Pascale 1993], ■ [O.C. Allkofer 1971], ▼ [Rastin 1984], ▲ [Ayre 1975], $\times, +$ [Kremer 1999], ○ [Haino 1999], and • [Archard 2004] and $\theta = 75^0$ ◊ [Jokisch 1979]). The line plots the result from Eq. 1.2 for vertical showers (the figure was taken from [Gaisser 2007]).

In the Fig. 1.5 is shown the muon energy spectrum at sea level for two angles. At large angles low energy muons decay before reaching the surface and high energy pions decay before they interact. An approximate extrapolation formula valid when muon decay is negligible ($E_\mu > 100/\cos\theta$) GeV and the curvature of the Earth can be neglected ($\theta < 70°$) is:

$$\frac{dN_\mu}{dE_\mu d\Omega} \approx \frac{0.14 E_\mu^{-2.7}}{cm^2 \times s \times sr \times GeV} \times \left(\frac{1}{1 + \frac{1.1 E_\mu \cos\theta}{\varepsilon_\pi}} + \frac{0.054}{1 + \frac{1.1 E_\mu \cos\theta}{\varepsilon_\kappa}} \right). \qquad (1.2)$$

The two values of ε_i where $i = \pi, \kappa$ are the critical energies which means that the probability of meson interaction in the atmosphere and decay are equal, $\varepsilon_\pi = 115$ GeV and $\varepsilon_k = 850$ GeV. Eq. 1.2 neglects small contribution from charm and heavier flavours which are negligible except at very high energy [Costa 2001].

The muon charge ratio $R(\mu^+/\mu^-)$ reflects the excess of π^+ over π^- and K^+ over K^- in the forward fragmentation region of proton initiated interactions together with the fact that there are more protons than neutrons in the primary spectrum. The increase with energy of $R(\mu^+/\mu^-)$ reflects the increasing importance of kaons in the TeV range [Adamson 2007] and indicates a significant contribution of associated production by cosmic-ray protons ($p \to \Lambda + K^+$).

1.4 Atmospheric muons underground

The penetrate component consists on muons and neutrinos which can reach to significant depths underground. On other hand, the muons can produce flux of photons, electrons and hadrons through photonuclear process.

Muons loss energy by continuous ionization and by stochastic radiative process: bremsstrahlung, direct production of e^+e^- pairs, and photonuclear interactions. The total muon energy loss may be expressed as a function of the amount of the matter traversed as:

$$-\frac{dE_\mu}{dX} = a + bE_\mu, \tag{1.3}$$

where a is the ionization loss and b is the fractional energy loss by the three radiation processes mentioned above. Both are slowly varying functions of energy. The quantity $\varepsilon \equiv a/b \approx 500$ GeV in standard rock, defines a critical energy below which continuous ionization loss is more important than radiative losses. In the Tab. 1.1 are shown a and b values for standard rock as a function of muon energy. The second column shows the muon range in standard rock ($A = 22$, $Z = 11$, $\rho = 2.65\ g\ cm^{-3}$). These parameters are quite sensitive to the chemical composition of the rock, which must be evaluated for each location. As we can see in Tab. 1.1 the most important energy loss for our purpose is due to the ionization loss being radiative loss negligible.

The intensity of muons underground follows the relation between the energy $E_{\mu,0}$ of a muon at production in the atmosphere and its average energy E_μ after traversing a thickness X of rock:

$$E_\mu = (E_{\mu,0} + \varepsilon)e^{-bX} - \varepsilon. \tag{1.4}$$

For high energies must be taking into account fluctuations, because are important, and then an accurate calculation is required by simulations that accounts for stochastic energy-loss processes [P.Lipari 1991].

E_μ	R	a	b_{brems}	b_{pair}	b_{nucl}	$\sum b_i$	$\sum b(ice)$
GeV	km.w.eq.	MeV $g^{-1}cm^2$	$---$	$----$	$10^{-6}g^{-1}cm^2$	$----$	$------$
10	0.05	2.17	0.70	0.70	0.50	1.90	1.66
100	0.41	2.44	1.10	1.53	0.41	3.04	2.51
1000	2.45	2.68	1.44	2.07	0.41	3.92	3.17
10000	6.09	2.93	1.62	2.27	0.46	4.35	3.78

Table 1.1: In the table are presented the average muon energy loss parameters calculated for standard rock [Groom 2001],[Amsler 2001].

1.5 Muon Charge Ratio

1.5.1 The importance of charge ratio measurements

As it was shown in the previous section the primary cosmic rays are dominantly high energy protons, alpha particles and heavier nuclei in a relative amount decreasing with the atomic number. When they penetrate from the outer space into the Earth's atmosphere they initiate the development of an Extensive Air Shower (EAS) cascades. The muonic component contributes only to few per cent in the single shower. At lower primary energies, which are dominating due to the steeply falling primary spectrum (see Fig 1.1), or in the case of very inclined showers the electromagnetic shower component is completely absorbed during the travel through the atmosphere, while the muons survive the propagation through even larger slant depths. Hence the inclusive secondary radiation flux in the atmosphere comprises mainly muons. The cosmic ray muons, usually called atmospheric muons, originate from decay of secondary hadrons produced in an EAS by primary cosmic rays. The are mainly produced through the following reactions:

$$\pi^+ \rightarrow \mu^+ + \nu_\mu(100.0\%(\tau_\pi = 2.6 \times 10^{-8}s)) \tag{1.5}$$

$$K^+ \rightarrow \mu^+ + \nu_\mu(63.5\%(\tau_\kappa = 1.2 \times 10^{-8}s)) \tag{1.6}$$

The muons decay with larger life time (2.2 μs) through the following reactions:

$$\mu^+ \rightarrow e^+ + \nu_e + \overline{\nu}_\mu \tag{1.7}$$

$$\mu^- \rightarrow e^- + \overline{\nu}_e + \nu_\mu \tag{1.8}$$

The ratio of positive to negative muons, the so called muon charge ratio $R_\mu(\mu^+/\mu^-)$ is a significant quantity which reflects important features of the hadronic meson production in cosmic ray collisions and can help to discern the primary mass composition [Adir 1977]. It is immediately obvious that the muon flux in the atmosphere is strongly related to neutrino flux and the muon charge ratio: $R_\mu(\mu^+/\mu^-) \sim R_(\nu_e/\overline{\nu}_e)$ provides relevant information for neutrino anomaly.

The effect of the influence of the Earth's magnetic field on muon fluxes is also considered in [P.Lipari 2000]. At lower energies, the fluxes of primaries and secondaries are influenced by the Earth's magnetic field, in particular by a magnetic rigidity cut-off of the primary cosmic ray penetrating the Earth's atmosphere from the cosmos, resulting in latitude dependence and in an East-West asymmetry of the incident flux. The influence of geomagnetic field leads an azimuth dependence on the muon charge ratio, in particular for low energy muons, which are dominant in EAS due to very low primary energies.

The muon charge ratio at sea level was extensively studied in the past, and as we can infer it is an indicator of important aspects of cosmic rays and particle physics.

An exhaustive compilation of measurements in a wide energy range is reported in [M.Ambrosio 1999]. In the interval from few hundred MeV to 200 GeV the muon charge ratio R_μ stays around 1.27. At higher energies several competing processes can affect its value. It is know that the component $K^\pm$ increases with energy, going from 10% at low energies to 25% at high energies. Since strong interaction production channels lead to a K^+/K^- ratio higher than the p^+/p^- ratio and the fraction of muons from kaon decay increases with the energy, then the muon charge ratio is expected to rise as the energy increases.

On the other hand, as the zenith angle increases, since κ mesons have a higher probability to decay in the less dense layers of the high atmosphere, the fraction of muons from pion decay increases and the muon charge ratio decreases.

The measurements of muon charge ratio at very large zenith angle (from 86^o to 90^o) were performed in the 70's by the 800 ton cosmic-ray spectrograph (MUTRON) at sea level in Japan in the momentum region of 100-20.000 GeV/c. The solid iron magnet spectrometer included a calorimeter of 120 tons of iron target. The momentum spectrum and charge ratio of cosmic rays muons have been measured by the magnetic spectrometer while the details of interactions of muons of known momenta have been studied in the calorimeter. The muon charge ratio at energies up to 15 TeV for $86^o - 90^o$ shows a small enhancement with increasing energy.

Similar results were obtained with DEIS large aperture, high resolution magnet spectrometer [Allkofer 1985] for very large zenith angle. The energy muon momentum interval is from 10 GeV to 10 TeV in the angular range $78^o - 90^o$.

1.5.2 The MINOS and OPERA experiments

In the recently years two experiments, dedicated to the neutrino oscillation search, are running in underground laboratories. Both designed to study the phenomena of

neutrino oscillation by using a beam of neutrino particles produce by the beamline facilities one at Fermilab in USA and the other at CERN, Geneve, Switzerland. In the case of USA experiment the beam of neutrinos is study through the two MINOS detectors, one situated at Fermilab (MINOS near) and the second one in the Soudan Mine (MINOS far) in the northern Minnesota. The relevant results are given by MINOS far located at 2070 m w.e. underground. The Fig. 1.6 shows the MINOS results on the ratio $R(\mu^+/\mu^-)$ compared with L3+C results and the fit with the Pika's model taking into account the pions and kaons corrections due to He and CNO production (see Ref. [Schreiner 2009] for more details). It shows a clear increase of the ratio with the muon momentum which ranges in the interval of 100 GeV/c to $\sim$ 2000 GeV/c.

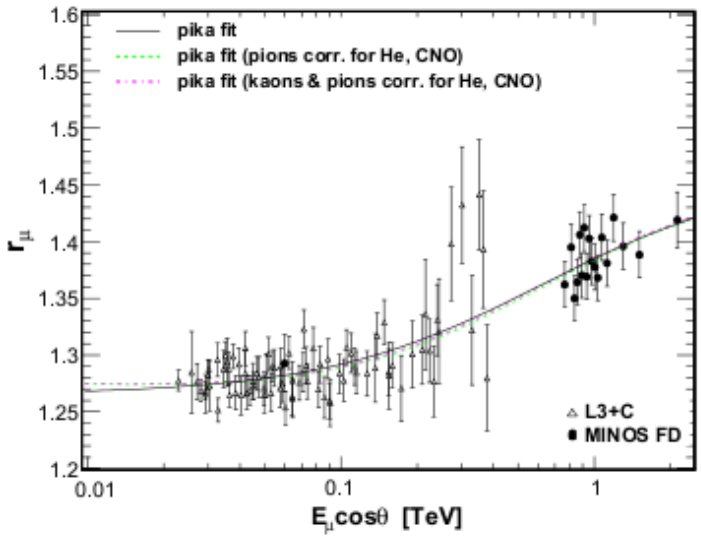

Figure 1.6: Muon Charge ratio measurement in comparison with L3+C experiment [Schreiner 2009].

In another hand, the charge ratio measured at MINOS near (at 225 m.w.e) and at MINOS far (at 2070 m.w.e) shows an increase in the charge ratio as a function of depth which is consistent with an increase in the fraction of muons arising from kaon decay for increasing muon surface energies [P.Adamson 2010].

The second experiment OPERA is running at Gran Sasso Laboratory at 3800 m.w.e. The minimum cosmic muon energy to reach OPERA is 1.5 TeV. Since Gran Sasso laboratory is much deeper and then the corresponding energy of muons higher, other contributions could be added to the study of the ratio R_μ. In particular at very high energy the contribution from charmed particle decays (prompt muons) must be taking into account. The results of OPERA for single (n_μ=1) R_μ integrated over the underground muon spectra is $R_\mu(n_\mu = 1) = 1.377 \pm 0.014$

to be compared to $R_\mu(n_\mu > 1) = 1.23 \pm 0.06$ for muon bundles. The difference of about $\sim 2.4\ \sigma$ supports the hypothesis of the decrease of the muon charge ratio with increasing the primary mass due to the presence of neutrons enhancement.

In Fig. 1.7 are shown the recent results of OPERA compared with other experiments and a model of pion, kaons contributions as well as models for prompt muon production in the atmosphere [N.Agafonova 2010].

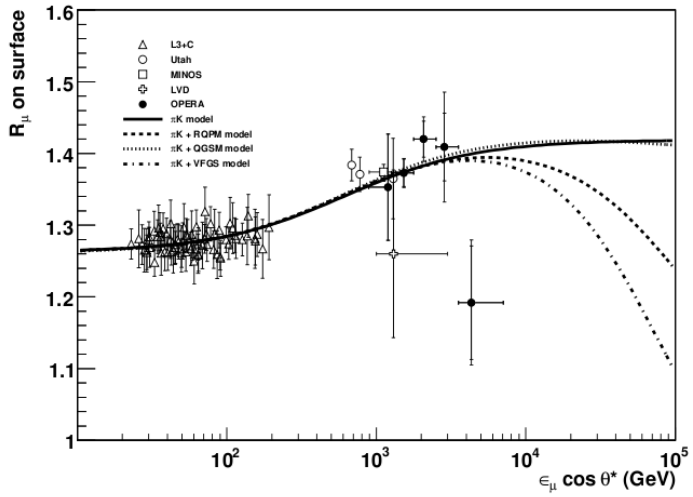

Figure 1.7: Muon Charge ratio as a function of the muon momentum from Ref. [N.Agafonova 2010]. R_μ values measured in bins of $E_\mu \cos(\theta^*)$ (black points). Also plotted are the data in low energy region from MINOS-ND [MINOS-Collaboration 2007] and L3+C experiment [Archard 2004] and in the high energy region from UTAH [G.K.Ashley 1975], MINOS and LVD [Aglietta 1995] experiments. The result of the fit of OPERA and L3+C data is shown by the continuous line. Dashed, dotted and dash-dot lines are, respectively the fit results with the inclusion of the RQPM, QGSM and VFGS models for prompt muon production in the atmosphere [N.Agafonova 2010]

Chapter 2

Cosmic Ray Physics with Accelerator Detectors

Contents

2.1 Introduction

When CERN (*the European Organization for Nuclear Research*) came into being in the early 1950s, a lot of changes were taking place in particle physics research. Until then, cosmic rays had provided most of the basic particle physics discoveries, in fact till then most elementary particles (pions, kaons, lambdas, etc.) were discovered by cosmic ray experiments.

Experiments in accelerators made their first contributions at Berkeley in 1949, with the Chicago and Carnegie synchrocyclotrons . In 1953, the Cosmotron, so named because it was the first accelerator to attain cosmic ray energies, began operation at Brookhaven and provided physicists with the first laboratory made strange particles.

At the Bagnères-de-Bigorre, France conference in 1953, leading cosmic-ray physicists, Cecil Powell, who had been awarded the 1950 Nobel Prize for the discovery (with G. Occhialini and C. Lattes) of the pion, introduced for the first time the new particle discovered in cosmic rays to accelerator physics. Although many of CERN's first-generation physicists starts their research on cosmic rays, for more than 40 years after the France conference all the new discoveries on particle physics arose from accelerators. With cosmic rays reporting particles beyond 10^{20}

eV, thousands of times as high as the highest laboratory energies, particle physicists are rediscovering again the attractions of natural sources of high-energy particles.

2.1.1 Cosmic ray revival

There are several motivations for this cosmic ray revival. On one hand, results from underground experiments like Super-Kamiokande in Japan, about of neutrinos produced by cosmic-ray collisions in the atmosphere, strongly suggest that the different kinds of neutrinos transform into each other or oscillate. In this case it requires accurate knowledge of the cosmic-ray muon spectrum in order to confirm the neutrino oscillation phenomena.

On the other hand, due the very close link between the astrophysics and particle physics have lead to the creation of new branch of physics science which is called the astroparticle physics.

With a relatively modest investiment, accelerators detectors can be exploited for cosmic-ray physiscs in parallel with their main purposes with no loss efficiency.

For example at CERN's LEP collider was taken place the L3 collaboration whose has formed the L3+Cosmics group, using new electronics to enable the muon spectrometer drift chambers to be read out independently of LEP data collection. An array of about 200 m^2 of scintillators has been installed over the top of the magnet to provide a reference time signal for cosmic-ray data collection (more details will be given in Section 2.3).

In the following section will be described the most relevant results of cosmic rays measurements done by the accelerators experiments and in particular we will focus on the muon measurements.

2.2 Cosmo-ALEPH Experiment

It is located at the deepest LEP point, 140 m underground, corresponding to a energy threshold of 70 GeV for vertical muon incidence. The magnetic solenoidal magnet together with the large *time-projection-chamber* (TPC) provides excellent pattern recognition , and tracking resolution. They recorded for example, muon bundles with densities up to 20 muons/m^2. The identification of muon induced showers (electromagnetic and hadronic) are possible due the high resolution of the TPC, which is surrounded by electromagnetic and hadronic calorimeters with tracking capabilities and by an outer shell of muon chambers (see Fig. 2.1).

The excellent resolution of the TPC enables an angular determination to better than 5 mrad, the average multiple scattering angle of the muons in the 140 m

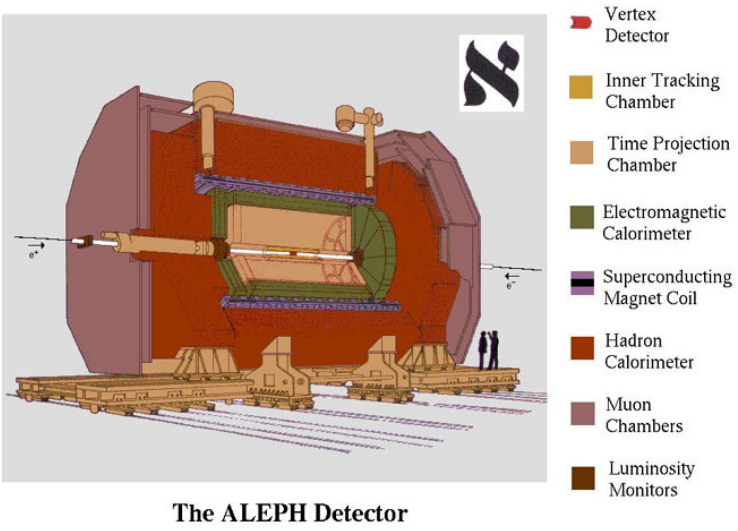

Figure 2.1: ALEPH experiment hall [Avati 2003].

overburden. Further information about the muon density is given by the forward calorimeters and muon chambers.

In the selection criteria were taking into account all muons in the event, with a track length larger than 0.5 m and at least four hits per track, which were reconstructed and their common arrival time was determined either from the electromagnetic calorimeter or from tracks crossing the central barrel of the TPC.

About 580 000 cosmic ray events were selected from the LEP data taking periods during the years 1997−99, corresponding to an effective data taking time of 1.7×10^6 $s \sim 20$ days.

2.2.1 Results

In principle, transverse size of muon-bundles and the muon multiplicity distributions (number of muons in the bundles) are sensitive to the mass number A of the initiating primaries cosmic rays. A clear difference of the radial muon distribution ($p_\mu > 70$ GeV/cos(θ)) produced by proton and iron induced air showers for various primary energies is predicted by the QGSJET CORSIKA simulation. The basic features of these distributions were, as the authors show in [Avati 2003]:

- the central muon density grows almost linearly with the primary energy and depends only slightly on the mass of the primary particle for energies above 10^{15} eV,

- the muon density falls rapidly with radius from the shower centre, dropping

by an order of magnitude over $15 - 20$ m. Its radial dependence is almost independent of energy for $E \geq 10^{15}$ eV,

- for primary energies exceeding 3×10^{14} eV the radial dependence of the muon density becomes flatter with increasing mass of the primary particle, leading to twice as many muons for iron induced showers compared to proton-induced events of the same total energy.

The TPC was the ideal detector to measure the local muon density at the highest observed values of 20 muons/m^2 and above. Fig. 2.2 shows the measured distribution of the muon multiplicity in the TPC and the QGSJET CORSIKA simulation for proton and iron primary particles [Avati 2003]. While The TPC itself is too small to contain a fraction of muon bundles and then to measure the radial dependence

Up to a multiplicity of 20, the proton curve describes the observed data well over several orders of magnitude, suggesting that the primary spectrum is dominated by lighter elements at energies corresponding to these multiplicities.

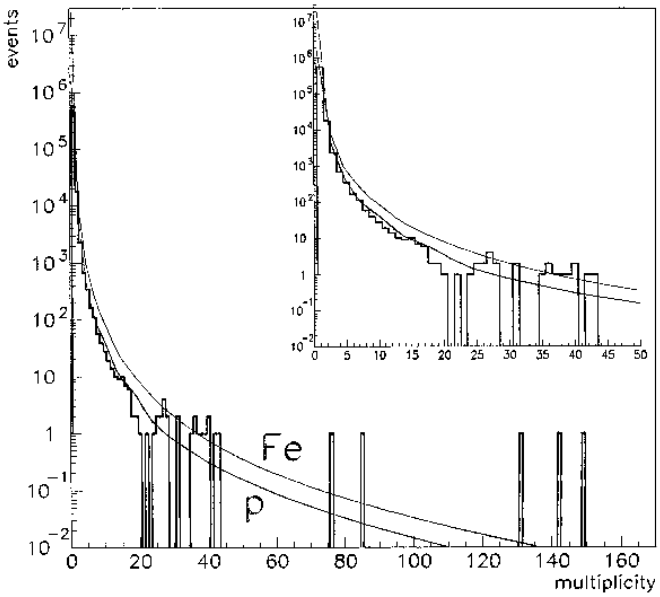

Figure 2.2: Multiplicity distribution of muons in the TPC compared to CORSIKA MC simulations for proton and iron as primary particle.

If we taking into account the superposition approximation of primary nuclei of mass A we can treated as A independent nucleons in consequence such nuclei will produce higher multiplicities of pions and then higher number of muons. Since the iron nuclei have larger cross sections it interacts higher in the atmosphere.

The simulation agrees with the data over a wide multiplicity range, however, it fails to describe the highest multiplicities, even under the extreme assumption of a pure iron composition. It is worth noting that four of the five highest multiplicity events have zenith angles beyond 30°. The highest multiplicity event displayed in Fig. 2.3, contains about 150 muons.

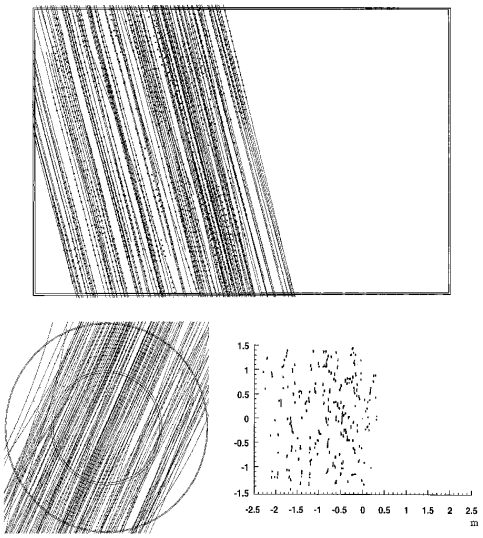

Figure 2.3: Event with the highest multiplicity (about 150 tracks, in half of the TPC) in three different views: longitudinal, transverse and along the shower axis. Reconstructed tracks are shown as lines.

2.2.1.1 Charge ratio measurement

The muon charge ratio has been measured by Cosmo-ALEPH and presented at the 28th ICRC [D.Zimmermann 2004]. Their results showed a general agreement with world average obtained by Hebbeker and Timmermans [Hebbeker 2002]. They obtained a value of 1.278±0.011 in the range of 80 to 2500 GeV/c.

2.3 L3+C Experiment

The muon flux and the charge ratio have been extensively studied by L3+C experiment and its results is presented using the precise spectrometer of L3 detector which was located at the LEP collider at CERN.

In The Fig. 2.4 is sketched a muon passing through the rock overburden, (molasse) till L3 apparatus. In addition, an array of 34 scintillators were placed on top of the L3 detector which covered an area of 202 m^2.

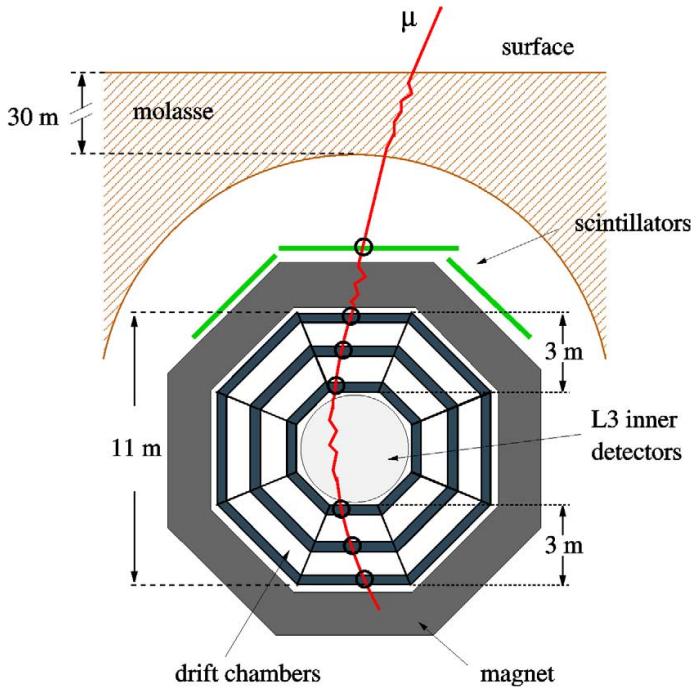

Figure 2.4: Schematic view of experimental setup [L3Collaboration 2004].

The large data recorded was about 1.2×10^{10} atmospheric muons during its operation in the years 1999 and 2000. Since, L3+C experiment was located $\sim$ 40 m underground, vertically incident muons, they calculated an mean energy loss in the molasse (X=6854gcm^{-2} $\sim$ 13.7 GeV).

2.3.1 Results

The measured muon fluxes, conventionally multiplied by the third power of the momentum, at the L3+C altitude are shown in Fig. 2.5 for each zenith angle bin from 0^o to 58^0 divided in eight $\cos\theta$ zenith angle bins. Since there was not previous measurements of the continuous zenith angle in the large energy range examined, only the vertical flux was compared to other experiments (see Fig. 2.6). The comparison to low energy experiments shown in Fig. 2.6 gives a good agreement between the analysis done by the experiment L3+C and previous measurements above about 40 GeV. At lower momenta, a systematic slope difference seems to be present, which corresponds to 2.5 standard deviations of the systematic molasse uncertainty estimated.

Only two previous experiments, both of them iron spectrometers, measured a normalized spectrum at high energies. As shown in Fig. 2.6, the shape of the Kiel measurements [L3Collaboration 2004] was in agreement with this result over

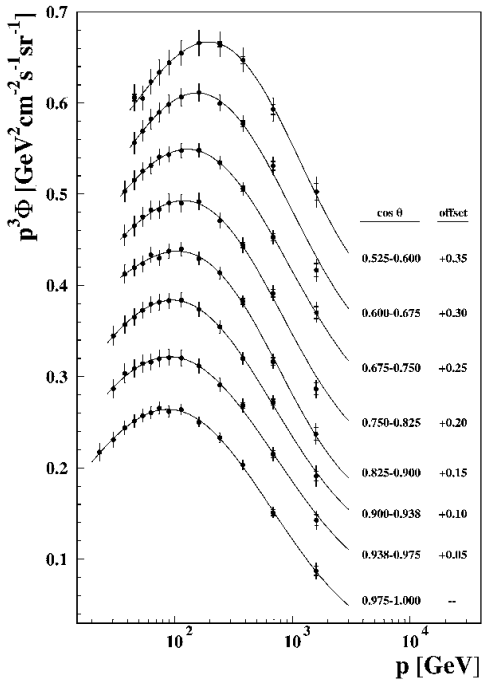

Figure 2.5: The measured muon flux for zenith angles ranging from 0^o (bottom) to 85^o (top). The inner bars denote the statistical uncertainty, the full bars show the total uncertainty. [L3Collaboration 2004].

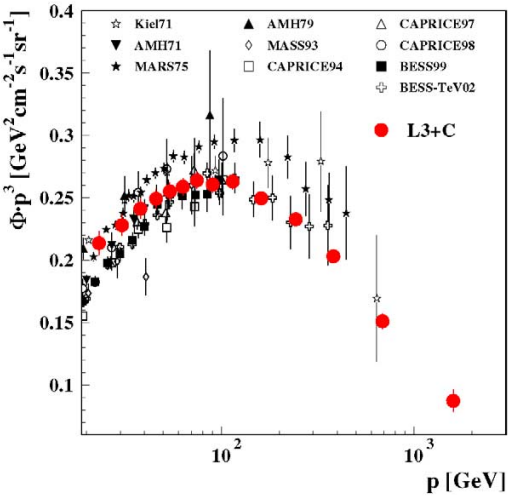

Figure 2.6: The L3+C vertical muon spectrum compared to previous direct measurements at low momenta providing an absolute flux normalization. All data are extrapolated to sea level. [L3Collaboration 2004].

the full momentum range, but a lower flux normalization is determined by L3+C experiment. The data obtained with the MARS apparatus significantly disagree with the L3+C.

The measured μ^+/μ^- ratios at the L3+C level are shown in Fig. 2.7 for each zenith angle bins up to momenta of 500 GeV/c. In the considered momentum range, the charge ratio is independent of the momentum within the experimental uncertainties. The μ^+/μ^- ratio reported in the vertical direction was 1.285±0.003(stat.)±0.019(syst.) [Archard 2004], which is in good agreement with the average of all previous measurements done, and even recent measurement done by CMS.

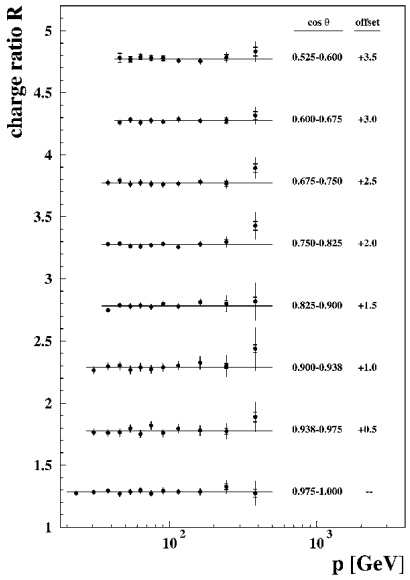

Figure 2.7: The measured muon charge ratio for zenith angles ranging from 0^o (bottom) to 58^o (top). The inner bars denote the statistical uncertainty, the full bars show the total uncertainty. [L3Collaboration 2004].

2.4 CMS Experiment

Recently results of the muon charge ratio was published for the Compact Muon Solenoid (CMS) at the Large Hadron Collider (LHC) at CERN (Geneve, Switzerland) [CMS-Collaboration 2010].

The CMS detector is installed in an underground cavern at 89 meters. A large superconducting solenoid with four-Tesla, hosts a high precision tracking system enclosed in electromagnetic and hadron calorimeters. Outside the magnet, the large muon detector is interleaved with the steel absorber plates that act as the

return yoke of the magnet.

During the commissioning period of CMS were collected cosmic muon runs, most of data-taking was devoted to test the detector: magnet, readout electronics, trigger and data acquisition system (DAQ), as well as alignment, calibration and event reconstruction algorithms. Thus high energy muons from cosmic rays were used for these tests. Although physics studies were not among the primary goals of the cosmic runs, these tests provided high quality data which can be used to perform measurements of physical quantities related to cosmic muons and in particular the μ^+/μ^- ratio.

2.4.1 Results

The measurements of the μ^+/μ^- ratio were given in the momentum region P <100 GeV/c in six P bins. The three lower bins are covered by all three analysis considered (for details see [CMS-Collaboration 2010]), with the surface-based MTCC analysis extending the reach to three lower momentum bins. These twelve data points yields a charge ratio of about 1.2766±0.0032(stat.)±0.0032(syst.) which is in good agreement with previous measurements.

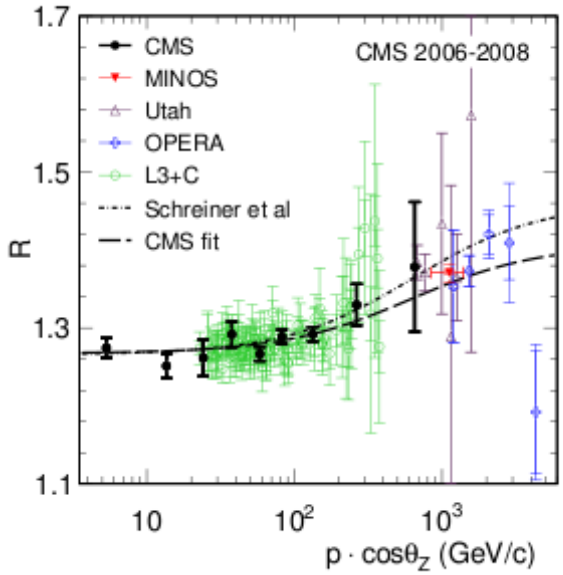

Figure 2.8: The CMS charge ratio measurement result as a function of the vertical component of the muon momentum, together with the some previous measurements and a fit of the pion-kaon model to the CMS data [CMS-Collaboration 2010].

Considering the pion-kaon model fit done by the CMS in the $p\cos(\theta_z)$ region below 100 GeV/c, this yields a charge ratio of 1.2772±0.0032(stat.)±0.0036(syst.).

Considering the full $p\cos(\theta_z)$ range, a rise in the charge ratio can be observed, as shown in Fig. 2.8. Comparing to previous measurements in the same momentum ranges, the CMS results are in good agreement in particular with the L3+C measurements [Archard 2004] below 400 GeV/c, and with the UTAH [G.K.Ashley 1975], MINOS [MINOS-Collaboration 2007], and OPERA [N.Agafonova 2010] measurements above 400 GeV/c.

Chapter 3

The ALICE Experiment

Contents

This chapter will briefly introduce the ALICE (A Large Ion Collider Experiment) experiment at the LHC (Large Hadron Collider) accelerator at CERN by describing the main subdetectors with emphasis to those that are used for the analysis described in this thesis.

3.1 Introduction

ALICE is the experiment dedicated to the heavy-ion program at the LHC (see Fig. 3.1). Its main purpose is to study nuclear matter at temperatures beyond the critical value, where QCD predicts a transition toward the deconfined phase of freely moving quarks and gluons. The energy densities reached at LHC exceeds those attained at SPS and RHIC giving the opportunity to explore the properties of nuclear matter at extremely high energy density and to study the transition from deconfined matter to ordinary hadronic matter. The collisions with protons are also taken into account and analysed as a reference for the heavy-ion measurements, and to pursue a dedicated p-p scientific program, complementary to the programs addressed by the ATLAS and CMS experiments.

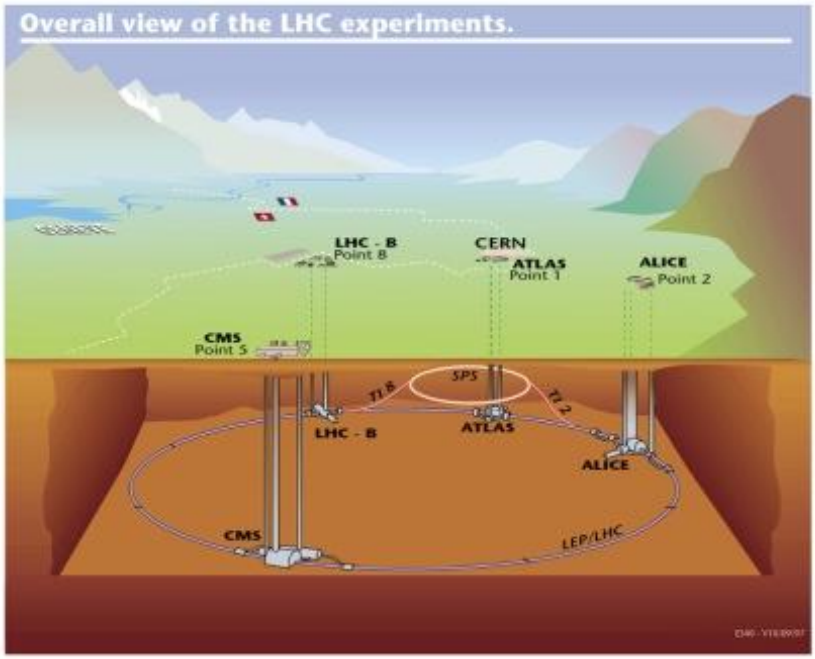

Figure 3.1: A schematic view of the LHC experiments.

To achieve these purposes, the experiment has been designed with the objective to measure most of the particles which emerge from heavy-ion collisions around mid-rapidity. An accurate determination of their momenta as well as their identification is required. Long lived charged hadrons are identified through energy-loss and time-of-flight measurements while short lived hadrons through the identification of their decay products. Measurements with the electromagnetic calorimetry of the transition radiation and photons identify the leptons. The momentum is obtained in the central-rapidity domain ($|\eta|$ <0.9), with a good resolution at very low momenta ($\sim$ 100 MeV/c) up to higher momenta by tracking charged particles within a magnetic field B = 0.5 T. Since in heavy-ion collisions an environment of extremely large particle densities was foreseen, such as 8000 particles per rapidity unit, a sophisticated system of detectors capable of tracking 15000 particles per event has been built.

All these peculiar capabilities can be exploited in the detection of atmospheric muons to study different topics connected with cosmic ray physics. In particular the possibility to measure events with very high muon density and for each muon to measure the momentum, the charge, the arrival time, the direction and the spacial coordinates make it unique for a multicomponent analysis. In this thesis, as a starting point, a study of the performances in measuring some of these observables have been done, focussing our attention on the charge ratio measurement. At this purpose some extensions of the features of the experiment, especially in the software,

have been developed to specific detect atmospheric muons. These development will be described in the next chapter, while in the next sections we will describe the main characteristics of the ALICE detectors involved in cosmic ray physics.

3.2 The central barrel detectors of ALICE for atmospheric muon tracking

ALICE consists of a central barrel part, which measures hadrons,electrons and photons, and a Forwad Muon Spectrometer (FMS) to measure the muons emitted in the forward region . The central barrel, embedded in a large solenoid magnet reused from the L3 experiment at LEP, is composed by a series of cylindrical detectors containing from the inside out an Inner Tracking System (ITS) of six planes of high-resolution silicon pixel (SPD), drift (SDD), and strip (SSD) detectors, a cylindrical Time Projection Chamber (TPC), three particle identification arrays of Time-of-Flight (TOF), Ring Imaging Cherenkov (HMPID) and Transition Radiation (TRD) detectors, and two electromagnetic calorimeters (PHOS and EMCal) see Fig. 3.2.

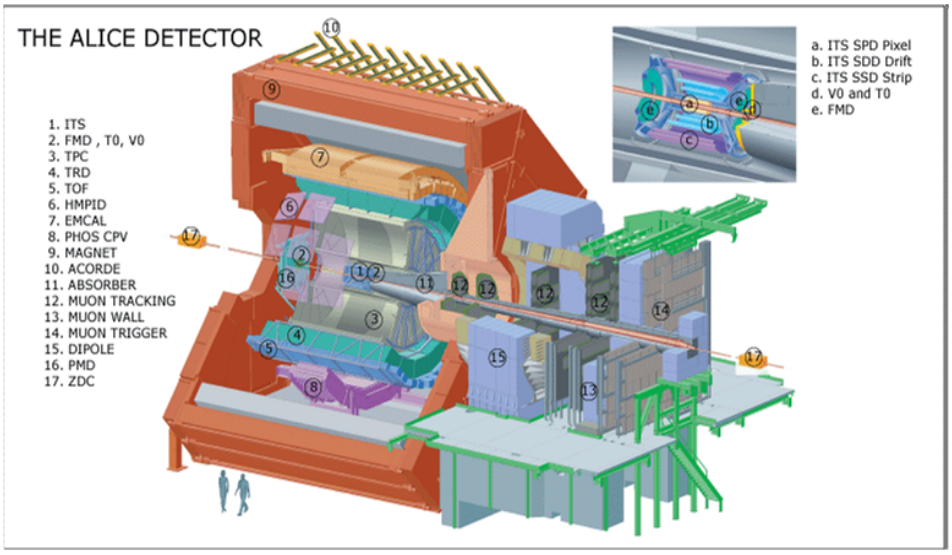

Figure 3.2: A schematic view of the ALICE detectors.

The Forward Muon Spectrometer $2^o - 9^o$ with respect the beam direction (z axis) consists of a complex arrangement of absorbers, a large dipole magnet, ten planes of tracking chambers and four planes of triggering chambers. Several smaller detectors (ZDC,PMD,FMD,TO,VO) for global event characterization and triggering are located at small angles. An array of 60 scintillators (ACORDE) on top of the L3 magnet is used to trigger on cosmic rays.

Some of the detectors of the central barrel have been used for the trigger of the atmospheric muons (ACORDE, TOF and SPD) while the tracking system has been provided by the TPC. These detectors have been mostly dedicated to the study of near-vertical muons, while the the FMS has been devoted at the detection of the horizontal muons.

3.2.1 Inner Tracking System (ITS)

Closest to the interaction point ($4cm \leq R \leq 44cm$) six layers of Si (silicon) detectors constitute the inner tracking system (ITS). The ITS has the function to track the particles near the collision point in which the density is very high and to extend the measurement of the transverse momentum below 100 MeV/c. In addition, in cooperation with the other tracking detectors, the ITS will determine with high accuracy ($<100\mu m$) the position of the primary vertex and of secondary vertexes for the identification of short-lived particles, such as hyperons, D and B mesons. The ITS will significantly improve the momentum resolution of the ALICE tracking system when used in conjunction with the TPC. The first two layers participate in the trigger by providing a fast hit-multiplicity measurements. To cope with the extremely high particle density expected (up to 90 particles/cm^2 in the first layer) in heavy-ion collisions, the ITS is made up by 6 layers of Si detectors of three different technologies, pixel, drift and strip detectors as shown schematically in Fig. 3.3. Located at radii between 4 and 43 cm. It covers the rapidity range of ($|\eta| < 0.9$) for all vertices located within the length of the interaction diamond ($\pm 1\sigma$,i.e.$\pm$5.3 cm along the beam direction). The number, position and segmentation of the layers were optimized for efficient track finding and high impact parameter resolution. In particular, the outer radius is determined by the necessity to match tracks with those from TPC, and the inner radius is the minimum allowed by the radius of the beam pipe.

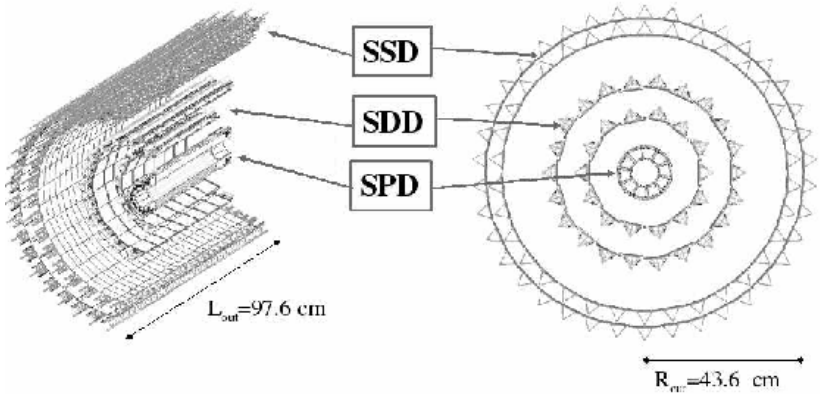

Figure 3.3: Layout of the ITS.

The four innermost layers, pixel and drift, provide true two-dimensional localization of the traversing particles and the four outer ones, drift and strip, have analog readout which provides particle identification through energy-loss measurements in the $1/\beta^2$ region. The geometrical dimensions and technology used in the various layers of the ITS are summarized in Table 3.1.

Layer	Type	r(cm)	±z(cm)	Area(m^2)	Channels
1	pixel	3.9	14.1	0.07	3276800
2	pixel	7.6	14.1	0.14	6553600
3	drift	15.0	22.2	0.42	43008
4	drift	23.9	29.7	0.89	90112
5	strip	38.0	43.1	2.20	1148928
6	strip	43.0	48.9	2.80	1459200

Table 3.1: Dimensions of the ITS detectors (active areas).

In our actual analysis the ITS was not employed in cooperation with the TPC for tracking the muons, because the small size of the detector would have considerably reduced the sample of the events. In a next future, with an increased statistics, it will be possible to built a special sample of muons crossing both TPC and ITS obtaining a very precise measurement of the whole track and strongly improve the resolution of the momentum. The SPD was instead used as one of the trigger detectors and the events analysed in the cosmic sample.

3.2.1.1 Silicon Pixel Detector (SPD)

The Silicon Pixel Detector (SPD) is based on hybrid silicon pixels, consisting of a two-dimensional matrix (sensor ladder) of revers-biased silicon detector diodes bump-bonded to readout chips. The signals are taken out from the pixel chips and transported to the readout electronics by a 3 layer flexible printed circuit, wire bonded to the chips. The SPD constitutes the two innermost layers of the ITS. It is a fundamental element for the determination of the primary vertex and of the impact parameter of secondary tracks originating from the weak decays of strange, charm and beauty particles. The SPD will operate in a region where the track density could be as high as 50 tracks/cm^2. It is also used as a trigger system for its rapidity to detect and elaborate a particle signal. The trigger is flexible and allows a different topology of events, such as high multiplicity from proton-proton collisions but also single muon for cosmics. In our cosmic runs it was inserted in the trigger logic to select muons crossing the detector, and it worked with a very high efficiency ($\sim 99\%$) and good purity.

3.2.1.2 Silicon Drift Detector: (SDD)

Silicon Drift Detector (SDD) constitutes the two intermediate layers of the ITS, where the density of the charged particles can reach up to 7 cm^{-2}. It is composed from 260 modules of silicon drift detectors with their front-end electronics. The modules are mounted on linear structures called ladders. The third layer of ITS is composed from 14 ladders each with 6 modules, the fourth from 22 ladders with 8 modules each. The space precision along the drift direction in around 40 μm and along the anode (z-axis) is around 30 μm.

3.2.1.3 Silicon Strip Detector: (SSD)

The two outermost layers of the ITS constitute the Silicon Strip Detector (SSD). It consist of 34 and 36 ladders each equipped with 23 and 26 double-sided silicon strip modules. These two layers, providing a two dimensional measurement of the track position, are fundamental to match the tracks from the TPC to the ITS. The spatial resolution is around 20 μm in the $r\Phi$ direction and 820 μm along the z-axis.

3.2.2 Time-Projection Chamber (TPC)

The Time-projection Chamber is the main tracking detector of the central barrel. It is designed, in cooperation with other central barrel detectors, to have good performances in the charge particle momentum measurements with high capabilities in the two track separation, particle identification and vertex determination.

The phase space covered by the TPC in pseudo-rapidity is $|\eta| < 0.9$ for tracks with full radial track length matching the ITS. But most of the atmospheric muons cross the TPC with a reduced track length and then reduced momentum resolution and do not cross the ITS. An acceptance up to about $|\eta| > 1.5$ is anyway accessible and a full coverage in the azimuth with the exception of some dead zones. A large p_t range is covered from low p_t of about 0.1 GeV/c up to 10 GeV/c with very good momentum resolution, while an extension to higher momentum (100 GeV/c) with particular track reconstruction codes has been introduced for the cosmic studies or for the particles crossing also the ITS.

A summary of the main parameters of the TPC is given in Table 3.2.

The TPC has a cylindrical shape with an inner radius of about 85 cm, an outer radius of 250 cm, and a length along the beam direction of 500 cm. The detector is made of a large cylindrical field cage, filled with 90 m^3 of $Ne - CO_2 - N_2$ gas mixture. The primary electrons, created from the ionization of a charged particle, are transported over a distance of up to 2.5 m on both sides from the central electrode to the end plates. The two end-caps of the TPC are instrumented with multi-wire proportional chambers with cathode pad readout mounted into 18 trapezoidal sectors at each end plate, for an overall active area of 32.5 m^2

Pseudo-rapidity coverage	-0.9< η <0.9 for full radial track lenght
	-1.5< η <1.5 radial track lenght
Aziuthal coverage	360^o
Radial position (active volume)	848< r <2466 mm
Radial size of vessel (outer dimensions)	606.5< r <2780 mm
Radial size of vessel (drift gas volume)	788< r <2580 mm
Length (active volume)	2×2500 mm
Segmentation in ϕ	18 sectors
Segmentation in r	2 chambers per sector
Total number of readout chambers	2×2×18=72
Inner readout chamber geometry	trapezoidal, 848< r <1321 mm active area
pad size	4×7.5 mm (ϕ×r)
pad rows	63
total pads	5504
Outer readout chamber geometry	trapezoidal, 1346< r <2466 mm active area
pad size	6×10 and 6×15 mm (ϕ×r)
pad rows	64+32=96 (small and large pads)
total pads	5952+4032=9984 (small and large pads)
Detector gas	Ne/CO_2/N_2 90/10/5
Gas volume	$90m^3$
Drift length	2×2500 mm
Drift field	400V/cm
Drift velocity	$2.7cm/\mu s$
Maximum drift time	$92\mu s$
Total HV	100kV
Diffusion	D_L=D_T=$220\mu m\sqrt{cm}$
Material budget	X/X_0=3.5% near $\eta = 0$
Front-End Cards (FEC)	121 per sector × 36 = 4356
Readout Control Unit (RCU) scheme	6 per sector,18 to 25 FEC per RCU
Total RCUs	216
Totla pads-readout channels	557568
Pad occupancy (for dN/dy=8000)	40 to 15% inner/outer radius
Pad occupancy (for pp)	5 to 2×10^{-4} inner/outer radius
Event size (for dN/dy=8000)	∼90MB
Event size (for pp)	∼1-4 MB (depending on pile-up and moise threshold)
Total bandwidth	∼30 GB/s
Trigger rate limits	300 Hz Pb-Pb central events
	1000 Hz proton-proton events
ADC	10 bit
Sampling frequency	5-10 MHz
Time samples	500-1000
Conversion gain	6 ADC counts/fC
Position resolution (σ) in rϕ	1100 to 800 μm inner/outer radii
in z	1250 to 1100 μm
dE/dx resolution, isolated tracks	5.0%
dN/dy=8000	6.8%

Table 3.2: Summary of the TPC parameters.

[H.Stelzer 2003],[Frankenfeld 2002]. Because of the radial dependence of the track density, the readout is segmented radially with slightly different wire geometry adapted to the varying pad sizes. The radial range of the active area for the inner chamber is from 84.8 cm to 132 cm and for the outer chamber from 134.6 cm to 246.6 cm.
A schematic view of the TPC structure is shown in the Fig. 3.4.

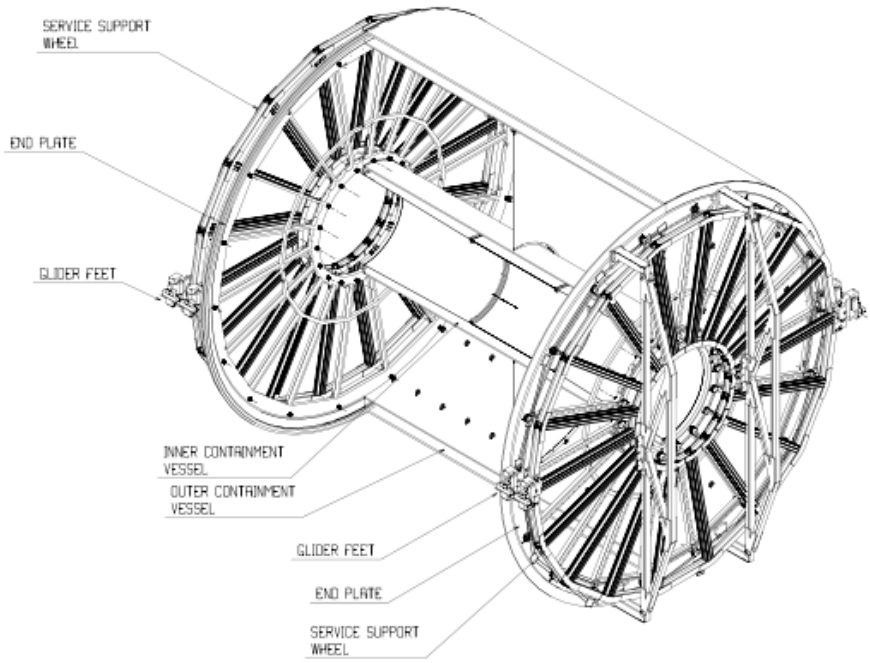

Figure 3.4: A schematic view of the TPC field cage and service support wheels.

The central electrode operates with a high voltage of 100 kV corresponding to a voltage gradient of 400 V/cm in the filed cage. The maximum drift time, for electrons travelling the entire length of half TPC (250 cm), is $\sim$ 90 μs. The gas mixture is chosen in a proper way to optimize the drift speed with low diffusion, low multiple scattering and radiation length, small space-charge effect, ageing and stability properties. The N_2 admixture improves the quenching and allows maximum gas gains [C.Gabaratos 2004]. The drawback of $Ne - CO_2$ is that this mixture is a cold gas, with a steep dependence of drift velocity on temperature [J.Wiechula 2005]. For this reason, the TPC is equipped with a system for a thermal stability of ΔT <0.1 K in the drift volume. The gas system circulates and purifies the gas mixture with very low fresh gas injection. The pressure follows the ambient pressure. The CO_2 and N_2 fractions are kept stable to 0.1% to ensure stable drift velocity and gas gain of the readout chambers.

3.2.3 Time-Of-Flight detector (TOF)

The Time-Of-Flight (TOF) detector is a large area array that covers the central pseudo-rapidity region $|\eta| < 0.9$. It was designed for particle identification in the intermediate momentum range, that is 2.5 GeV/c for pions and kaons, up to 4 GeV/c for protons,and a π/K and K/p separation better than 3σ [Alessandro 2006],[Akindinov 2004]. It can be used in conjunction with TPC and ITS for and event-by-event identification of pions, kaons and protons, for tracking particles giving a large lever arm and for vertex reconstruction. In addition, at the inclusive level, identified kaons will allow invariant mass studies, in particular the detection of open heavy-flavoured states and vector-meson resonances such as the ϕ meson. Details on the physics observables that can be addressed and the expected performance are detailed in references [Collaboration 1995],[Alessandro 2006],[Akindinov 2004],[Akindinov 2006]. Since the TOF surrounds the TPC cylinder it is very useful as a trigger detector for cosmic muons crossing the TPC.

The detector covers a cylindrical surface with a modular structure corresponding to 18 sectors in Φ and to 5 segments in z direction. The inner radius of the cylinder is 370 cm while the outer is 399 cm. The basic unit of the TOF is a 10-gap double-stack MRPC (Multigap Resistive Plate Chamber) strip see Fig. 3.5.

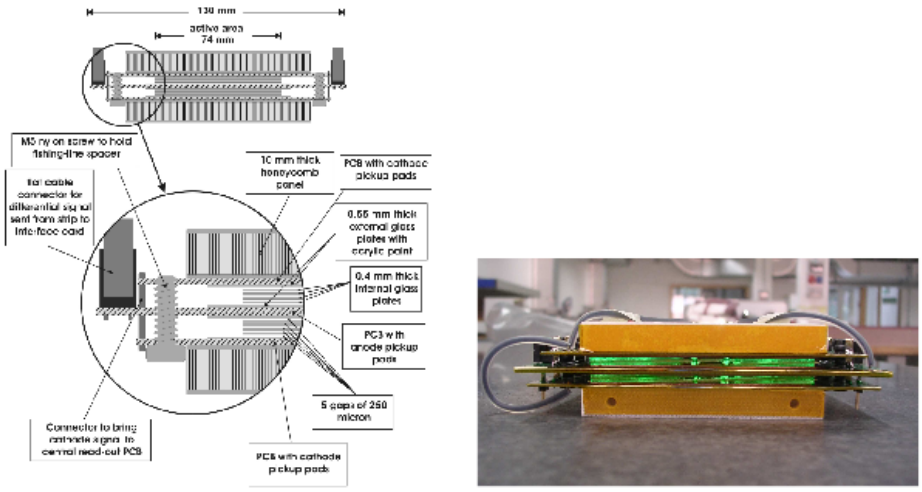

Figure 3.5: Schematic cross section (left) and the photograph (right) of a 10-gap double-stack MRPC strip.

The strip is 122cm long and 13cm wide, with an active area of $120\times7.4cm^2$ subdivided into two rows of 48 pads of $3.5\times2.5cm^2$. An overall view of a strip is shown in Fig. 3.6. The strips are placed inside gas-tight modules and are positioned transversely to the beam direction (z-axis). Five modules of the three

different types cover the full cylinder along the z direction. They have the same structure and a width of 128 cm but the central module has a length of 117 cm, the intermediate 137 cm, and the external 177 cm. The overall TOF barrel length has 741 cm of active region. Every module of the TOF detector consists of a group of MPRC strips : 15 in the central modules, 19 in the intermediate and in the external modules. The complete TOF has 90 modules. Five modules are inserted in a supermodule framework for each of the 18 sectors see Fig. 3.7.

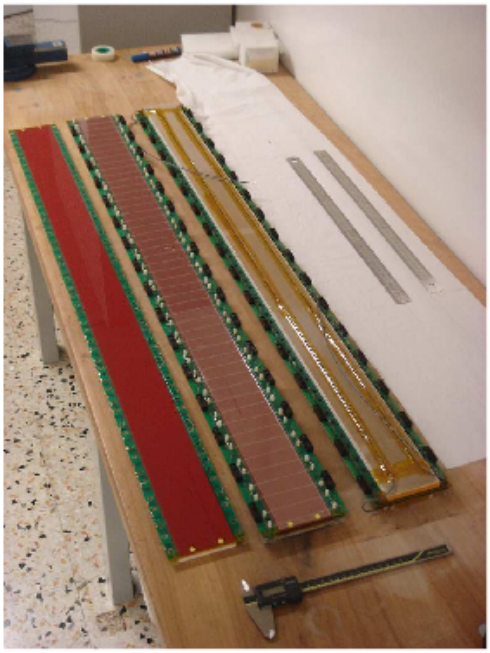

Figure 3.6: Photograph of an MRPC strip.

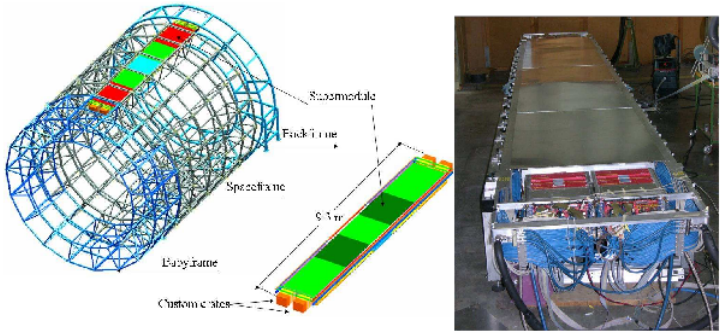

Figure 3.7: Schematic drawing of one TOF supermodule, consisting of 5 modules, at the ALICE spaceframe (left panel). A supermodule after assembly; in the foreground, the two custom crates with electronics (right panel).

An overview of the TOF detector parameters is shown in Table 3.3.

Pseudo-rapidity coverage	-0.9< η <0.9
Aziuthal coverage	360^o
Radial position	370< r <399cm
Length (active volume)	741cm
Segmentation in ϕ	18-fold
Segmentation in z	5-fold
Total number of modules	90
Central module (A)	$117\times128cm^2$
Intermediate module (B)	$137\times128cm^2$
External module (C)	$177\times128cm^2$
Detector active area (total area)	$141m^2(171m^2)$
Detector radial thickness	X/X_o=29.5%
Number of MPRC strips per module	15 (A), 19 (B),19 (C)
Number of readout pads per MRPC strip	96
Module segmentation in ϕ	48 pads
Module segmentation in z	30 (A),38 (B),38 (C) pads
Readout pad geometry	$3.5\times2.5cm^2$
Total number of MRPC strips	1638
Total number of readout pads	157248
Detector gas	$C_2H_2F_4/i-C_4H_10/SF_6$ 90%/5%/5%
Gas volume	$17.5m^3$
Drift length	2×2500 mm
Total flow rate	$1m^3$/h
Working overpressure	<3 mbar
Fresh gas flow rate	$0.02m^3$/h
Number of readout channels	157248
Number of front-end analogue chips (8-ch)	19656
Number of front-end boards	6552
Number of HPTDC chips (8-ch,24.4ps bin width)	20520
Number of HPTDC readout boards (TRM)	684
Number of readout boards (DRM) and crates	72
Occupancy for dN_ch/dη=8000	14% (B=0.5 T)
Occupancy for pp	10^{-4} (B=0.5 T)
π/K identification range (with contamination < 20%)	0.5-3.0 GeV/c
proton indentification range (with contamination <15%)	0.5-6.0 GeV/c
electron identification range in pp (with contamination <10%)	0.3-0.5 GeV/c
Event size (for dN/dy=8000)	110 kB
Event size (for pp)	24 kB

Table 3.3: Overview of the TOF parameters.

3.2.4 ALICE COsmic Ray DEtector (ACORDE)

ACORDE, the ALICE cosmic ray detector, is an array of plastic scintillator counters placed on the upper surface of the L3 magnet. The main task of ACORDE is to provide a fast trigger signal (level-0), for the commissioning, calibration and alignment procedures of the tracking detectors of the central barrel. The trigger is given when an atmospheric muon crosses and fires one of the plastic modules. For this reason it has been used for cosmic studies. A feasibility and performance study is detailed in references [Carminati 2004],[Alessandro 2006],[Fernandez 2007],[Adriani 2002].

An ACORDE module consists of two scintillator counters, each one with $190\times20cm^2$ effective area, placed on top of each others and readout in coincidence see Fig 3.8. The signal coincidence of two counters reduces the background and gives an almost uniform efficiency higher than 90% along the whole length of the module. The ACORDE array, which includes 60 scintillator counter modules is shown in Fig. 3.8. The main parameters of this detector are summarized in Table 3.4.

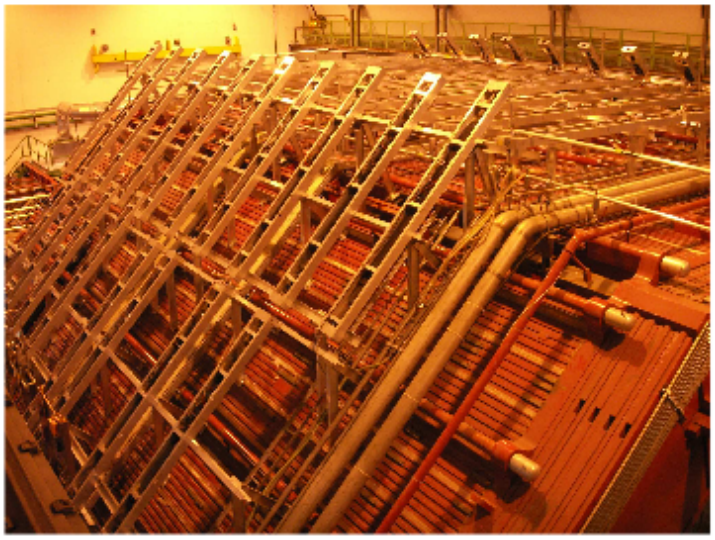

Figure 3.8: Photograph of the ACORDE scintillators modules array on the upper faces of the octant magnet yoke of ALICE. An ACORDE module unit includes two overlapping scintillator counters, each with $190\times20cm^2$ effective area, and 10 mm thickness, plus two PMTs placed at the end of each scintillator, with optic guide and iron magnetic shielding. All components are attached to an aluminium structure, assembling a 40 kg robust box. There are 20 modules on each one of the three upper faces.

The typical rate for a single atmospheric muons reaching the ALICE detector is relatively low (4.5 Hz/m^2, on top of the magnet), the ACORDE rate for single muon is around 100 Hz (one module fired) that drastically decreases at less than 1 Hz for a two-fold coincidence, a rate compatible with a possible cosmic trigger

Pseudo-rapidity coverage	-1.3< η <1.3
Aziuthal coverage	$-60^o < \phi < 60^o$
Radial position	r = 8.5 m
Total number of detector modules	60
Module size	$300\times26\times10cm^3$
Active detector area	$190\times20cm^2$
Radial detector thickness	X/X_0=4.7%
Module segmentation	30 in ϕ, 2 in z
Number of readout channels	120
Number of readout boards	60
Trigger time delay electronics for single muon coincidence	220 ns
multi-muon coincidence	270 ns
TRD wake-up	170 ns
Rate for cosmic single muon events	4.5 Hz/m^2
Rate for cosmic 5-fold coincidence module events	5×10^{-3} Hz

Table 3.4: Overview of the ACORDE detector parameters.

during LHC operations and normal ALICE data taking.

3.3 The Forward Muon Spectrometer (FMS) for horizontal atmospheric muon detection

The Forward Muon Spectrometer is located outside the central barrel and has been designed to detect muons in the pseudo-rapidity region -4.0< η <-2.5 to measure the heavy-quark resonances like the J/Ψ, $\Psi^{'}, \Upsilon, \Upsilon^{'}$ and $\Upsilon^{''}$), as well as the ϕ meson in the $\mu^+\mu^-$ decay channel. The comparison of the production rate of the various quarkonia species, in function of the centrality of the events or transverse momentum, is one of the purpose of this apparatus as well as the study of the production of open flavours from their semi-leptonic decays.

Since it detects the muons in the forward region, the detector can also be employed to trigger on atmospheric muons with large zenith angles (horizontal muons) and track them.

The layout of the muon spectrometer is shown in Fig. 3.9 and Fig. 3.10. The spectrometer consists of the following components:

- a passive front absorber to absorb hadrons and photons from collision point
- five chambers each with two planes of RPC to track the muons
- a large dipole magnet,
- a passive muon-filter wall,
- two trigger chambers each with two planes of RPC

- an inner beam shield to protect the chambers from particles with high rapidity.

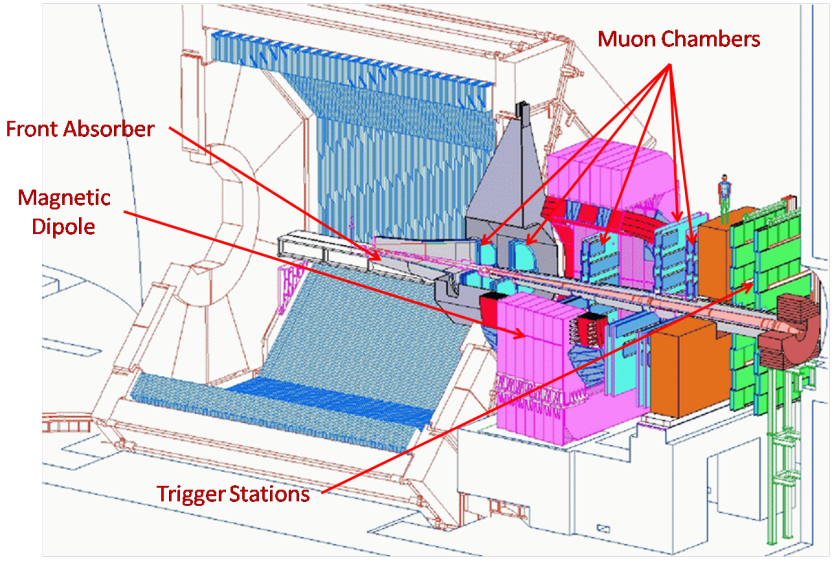

Figure 3.9: Layout of the muon spectrometer.

Great care was taken both in the design of the absorber, which have to provide strong absorption of the hadron flux coming from the vertex and of the detectors ,which must be able to sustain the remaining high multiplicity. The main challenge for the muon spectrometer results the high particle multiplicity per event rather than from the event rate, which is modest. These problems are irrelevant for the cosmic muon detection, because the multiplicity is very close to one and the rate is very low. Only in the eventuality of taking cosmic events during standard running of LHC these peculiarities should become necessaries.

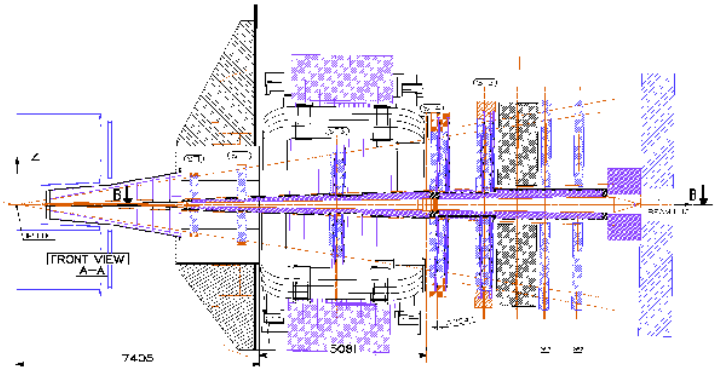

Figure 3.10: Muon spectrometer longitudinal section; according to the adopted numbering scheme station 1 (ST1) is the closest to the central barrel.

3.3.1 Absorbers

The front absorber, whose length is 4.13 m ($\sim 10\lambda_{int}$,$\sim 60X_0$), is located inside the solenoid magnet. The fiducial region of the absorber is made predominantly out of carbon and concrete to limit multiple scattering and energy loss by traversing muons while the front absorber is designed to protect the other detectors from secondaries produced within the absorbing material itself [Grigoryan 2002]. The spectrometer is shielded throughout its length by a dense absorber tube made of tungsten, lead and stainless steel surrounding the beam pipe. It has a conical geometry to reduce background particle interaction along the length of the spectrometer (see Fig. 3.9). The trigger chambers are additionally protected from a muon filter, i.e. an iron wall 1.2 m thick ($\sim 7.2\lambda_{int}$), placed after the last tracking chamber, in front of the first trigger chamber. The front absorber and filter stop muons with momentum less than 4 GeV/c.

3.3.2 Tracking system

Tracking chambers were designed to achieve a spatial resolution of about $100\mu m$, necessary for an invariant-mass resolution of the order of 100 MeV/c^2 at the Υ mass [Rimai 1997],[Wurzinger 1997]. They can sustain a very high hit density of about $5\times 10^{-2} cm^{-2}$ necessary for heavy-ion central collisions. The tracking system covers a total area of 100 m^2.

The spectrometer is composed from five stations of cathode pad chambers as shown in Fig. 3.9: two are placed before, one inside and two after the dipole magnet. Each station is made of two chambers planes. Each chamber has to cathode planes, which are both readout to provide two-dimensional hit information. Multiple scattering of the muons in the chambers is minimized by using composite materials (e.g. carbon fibre). Additional information about the muon tracking system can be found in references [Chabratova 2003a],[Zintchenko 2003].

The chambers have different size ranging from few square metres for the station 1 to more than 30 m^2 for the station 5. The first station is located close behind the absorber to measure the exit points of the muons. Since the hit density decreases with the distance from the beam,larger pads are used at larger radii, keeping the total number of channels at about one million. The first two stations are based on a quadrant structure [Peyré 1998], with the readout electronics distributed on their surface (see Fig. 3.11), while the other stations have a slat architecture (see Fig. 3.12). The maximum size of the slat is $40\times 280 cm^2$ and the electronics is implemented on the side of the slats. The slats and the quadrants overlap to avoid dead zones on the detector. The main parameters of the muon spectrometer are summarized in Table 3.5.

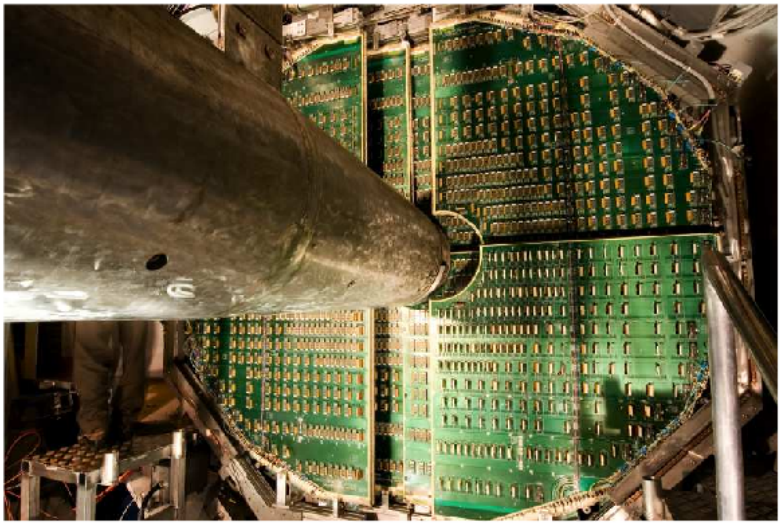

Figure 3.11: Layout of the station 2 of tracking system. Readout electronics is distributed on the surface of a quadrant structure.

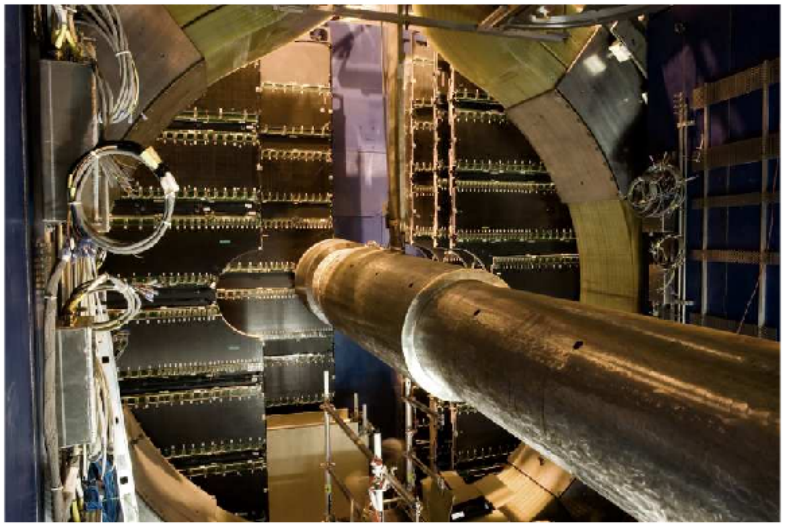

Figure 3.12: Layout of the stations 4 and 5 of tracking system.

3.3.3 Geometry monitoring system

The alignment of the spectrometer tracking chambers is crucial to achieve a good momentum resolution especially at high momenta. Dedicated runs without magnetic field are carried out at the beginning of the each data taking period in order to align the ten tracking chambers with straight muon tracks. When magnetic field is switched on a slight displacement and deformation affects the

Pseudo-rapidity coverage	-4.0< η <-2.5
Polar,azimuthal coverage	$171^o < \theta < 178^o$,360^o
Minimum muon momentum	4 GeV/c
Front absorber	
Longitudinal position (from IP)	-5030mm$\leq z \leq$-900mm
Total thickness (materials)	($\sim 10\lambda_{int}, \sim 60X_0$) (carbon-concrete-steel)
Dipole magnet	
Nominal magnetic field, integral field	0.67 T,3 Tm
Free gap between poles	2.972-3.956 m
Overall magnet length	4.97 m
Longitudinal position (from IP)	-z = 9.94 m (centre of the dipole coils)
Tracking chambers	
Number fof stations, and of planes per station	5,2
Longitudinal position of stations	-z=5357,6860,9830,12920,14221 mm
Gas mixture	80%Ar/20%CO_2
Pad size st. 1 (bending plane)	4.2×6.3,4.2×12.6,4.2×25.2 mm^2
Pad size st. 2 (bending plane)	5×7.5,5×15,5×30 mm^2
Pad size st. 3,4,5 (bending plane)	5×25,5×50,5×100 mm^2
Max. hit dens. st. 1-5 (central Pd-Pd×2)	5.0,2.1,0.7,0.5,0.6×10^{-2}hits/cm^2
Spatial resolution (bending plane)	$\simeq 70\mu m$
Tracking electronics	
Total number of FEE channels	1.08×10^6
Shaping amplifier peaking time	1.2μs
Trigger chambers	
Number of stations, number of planes per station	2,2
Longitudinal position of stations	-z = 16120,17120 mm
Total number of RPCs, total active	72,$\sim 140m^2$
Gas gap	single,2mm
Electrode amterial and resistivity	$Backelite^{TM}$,ρ=2-8×$10^9\omega$cm
Gas mixture	Ar/$C_2H_2F_4$/i-buthane/SF_6 (50.5/41.3/7.2/1)
Pitch of readout strips (bending plane)	10.6,21.2,42.5 mm (for trigger st. 1)
Max. strip occupancy bend. (non bend.) plane	3% (10%) in central Pb-Pb
Max. hit rate on RPCs	3(40) Hz/cm^2 in Pb-Pb (Ar-Ar)
Trigger electronics	
Total number of FEE channels	2.1×10^4
Number of local trigger cards	234+8

Table 3.5: Summary of the main characteristics of the muon spectrometer.

chambers, these effects are measured and recorded during data taking by the Geometry Monitoring System (GMS).

The GMS is an array of 460 optical sensors which are installed on platforms placed at each corner of the tracking chambers. A detailed description of these devices can be found in references [Tieulent 2005],[Pillot 2005]. The requirement is to monitor the position of all the tracking chambers with a resolution better than $40\mu m$.

3.3.4 Tracking electronics

The design of the electronics of the tracking system was driven to read about one million channels up to a rate of the order of kHz and to achieve a space resolution of the tracking chambers of at least $100\mu m$. The electronics chain is divided in three parts: the front-end boards, the readout system, and the interface with the general ALICE trigger[Courtat 2004].

Chapter 4

Reconstruction of Atmospheric Muon Tracks

Contents

This chapter focuses on the reconstruction of atmospheric muon tracks crossing the TPC for the detection of *near-vertical muons*, and crossing the Forward Muon Spectrometer (FMS) for *near-horizontal muons*. The standard tracking code for particle passing through the TPC is optimized for p-p or Pb-Pb collisions in the LHC. The tracks, hence, are forced to pass at the collision point located near the center of the TPC, and each track is developed only in one half of the TPC, the upper part or the lower part. Atmospheric muons have a complete different topology. They do not have an interaction point and usually they cross the entire cylinder of the TPC from up to down. Therefore the standard tracking algorithms have been adapted and integrated with special codes for reconstructing the atmospheric muon tracks. In the FMS minor changes have been done in order to adapt the standard reconstruction for *near-horizontal muons*. The difference is only in the requirement that atmospheric muons are not forced to pass in the interaction point.

4.1 Muon Reconstruction in the TPC

4.1.1 Track reconstruction in the TPC

The standard method to find and fit a particle track in the TPC employs the Kalman filter. The Kalman filter is a method that uses measurements done over time in a system with noises and inaccuracies to correct the raw measurement. It gives an estimate of true values of the measurements in a recursive way. Suppose to measure at time t_1 some variables of a physical system determined by a state vector

$\mathbf{v}_1$. The state vector varies in time according to some physical laws and at time t_2 we do another measurement on the same variables. To obtain a better evaluation of these variables at time t_2 with respect the crude measurement corrupted by the noise, the inaccuracy and other effects, the Kalman filter starts from time t_1 and does a theoretical evaluation of the values at time t_2 (predicted a priori values) and an estimate of the covariances (predicted a priori covariances). In the following phase the predicted values are combined with the measured values at time t_2 to give values that should be closer to the true values. The same procedure will be applied recursively for the other times. The values obtained should be closer to the true values for the following reasons. The estimate values are given using physical models to evolve the system keeping into account noises, accuracies and other properties of the system. The covariance is an estimate of the uncertainty of the values and the Kalman filter weights the values obtained with their covariance, favouring the values with a lower uncertainty.

Applied to the track reconstruction problem this method allows simultaneous track recognition and fitting reducing the reconstruction time. The standard procedure begins searching and reconstructing the clusters (a set of adjacent digits) of the TPC. The space point positions are calculated from the center of gravity of these clusters in two dimensions, pad-row and time directions. >From these points the method searches the track candidates starting from the outer radius of the detector and proceeding towards the smaller TPC radius. New points, when found, are added at the track candidate, and the track parameters are refined with the Kalman filter method up to the inner limit of the TPC. The method determines, for each track, a set of values for the track parameters and their covariance matrix.

In standard reconstruction it is assumed that the track originates from a primary vertex while for atmospheric muons this assumption in not valid and the track can originate elsewhere. The efficiency in the reconstruction of the tracks of this method for very low density events, as the case of atmospheric muons, is around 100%.

4.1.2 The algorithm to match the muon tracks in the TPC

Atmospheric muons usually cross the entire length of the TPC from up to down. In the previous section we have seen that the standard reconstruction method, optimized for particles coming from p-p collisions, reconstructs two tracks for each trajectory : one in the upper semi-cylinder of the TPC that we call track up, and the other in the lower semi-cylinder (track down) as shown in a single muon event of Fig. 4.1.

In order to obtain the whole track of the muon, and count the exact number of them, especially in high multiplicity events, we have implemented an algorithm to match the two tracks corresponding to an atmospheric muon. The main property of these muons is the parallelism, then the tracks are required to be parallel.

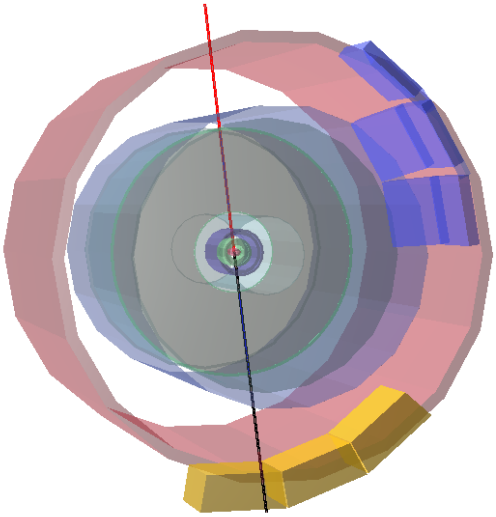

Figure 4.1: A single muon crossing the TPC. The standard TPC method reconstructs the muon trajectory with two tracks: 'track up' in the upper part (red line) and 'track down' in the lower part (black line).

The track matching algorithm implemented is briefly described from the following steps :

- Only tracks with more than 30 clusters are considered.
- For each track we do a loop over the others to mark and count the tracks parallel to the current track. Two tracks are defined parallel if $cos\Psi > 0.990$ where Ψ is the spatial angle between the two tracks.
- We choose as "main track" of the event, obtaining also the main direction, the track that has the greatest number of parallel tracks.
- We select all the tracks parallel to the main track and discard the others.
- We perform the matching among all the parallel tracks. We take a "track up" and look for the closest "track down". The two tracks match if the maximum distance between them is less than 2 cm. These two tracks are considered the track of a muon.

The total number of muons and their identification is obtained from the number of matched tracks (up and down counted once) plus all the single tracks, that is, not matched tracks. An additional cut of 50 clusters (instead of 30) is requested for the single tracks.

This method has been tested with good results for low and high muon multiplicity (up to 200 muons) and compared with a visual scan using the standard ALICE event display. The efficiency in matching two tracks belonging to a single muon event is close to 100%.

During these studies we have noted that some high multiplicity events are not due to atmospheric muon bundles, but to an interaction of an high energetic muon with the iron structure of the magnet (see Fig. 4.2), which can be confused with a multi-muon event. This interaction creates a shower of particles crossing the TPC and some particles can satisfy all the above matching criteria in such a way that the algorithm consider it like a multi-muon event. Since these events have a very different topology with respect multi-muon events, as we can see in Fig. 4.3, some additional variables have been introduce to distinguish them.

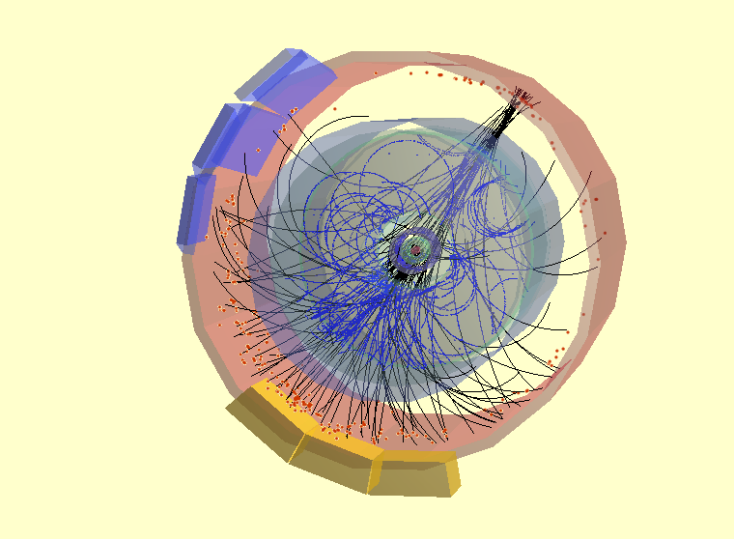

Figure 4.2: An example of event in which an atmospheric muon interacts with the iron structure of the magnet magnet and generates a shower of particles crossing the TPC.

In particular the average distance between the main track (as defined above) and all the others is considerable smaller in interaction events. The value of the ratio 'Number of tracks' over 'Number of muon reconstructed' is, on the contrary, greater in interaction events. After a detailed study of these variables we have been able to distinguish these two types of events applying some cuts to these variables. The two separate regions corresponding to interaction and multi-muon events are shown in Fig. 4.4 in which is plotted the correlation between Ntracks/Nmuons and Average Distance.

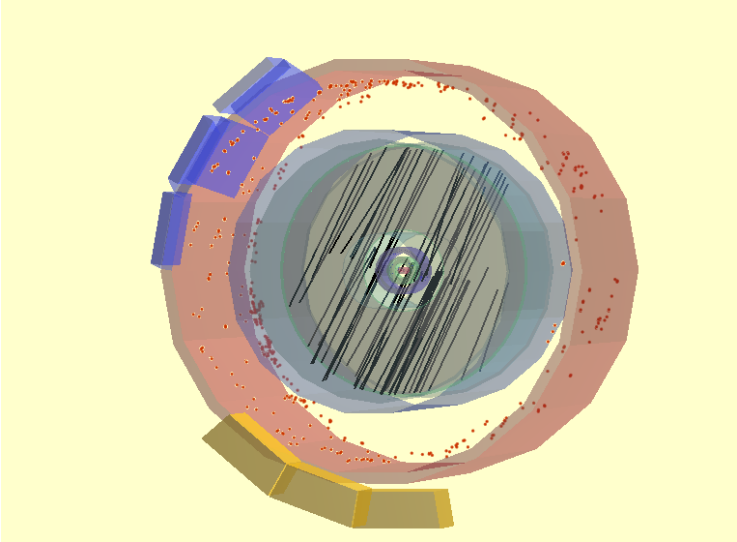

Figure 4.3: An example of multi-muon event. The reconstructed muon tracks in black cross the TPC.

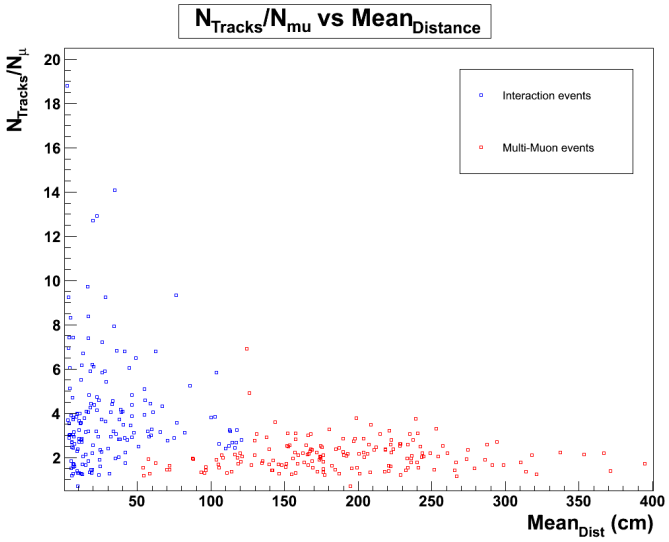

Figure 4.4: Ratio Number of tracks/Number of muons vs Average Distance between the main track and the other parallel tracks.

4.2 Track Reconstruction in the FMS

When a muon enters into the spectrometer and interacts with the tracking chambers, it generates a distribution of charge spread among several pads in both cathode planes. The charge collected by each individual strip is read-out by the front end electronic of the tracking system and stored in the Root format in the

raw data objects. The aim of the muon reconstruction code is to reconstruct the kinematics of the muon (position, orientation, momentum) from the raw data. It is a multistage process, which is divided into three stages: the digitization of raw data, the clustering of the digits to locate the crossing point of the muon with the chamber, and the track reconstruction of the trajectory of the muon in the spectrometer from which we can extract the muon momentum.

Digitization and Clustering. The first part of the reconstruction is the conversion of raw-data into digits. The digits are then calibrated by subtracting pedestals and multiplying by gains. All the calibration parameters (pedestals, gains, capacitances and HV) are read from the Offline Calibration DataBase (OCDB). Those parameters are also used to build the digit status word providing information about the quality of the digit. We can define quality criteria in the reconstruction parameters to select the digits to be used during the clustering. The calibrate digits and their status can be saved in root files format. The digit is converted into pad, which contain information about the position of the digit in the detection element reference frame, and then the
clustering is performed in two steps: the pre-clustering then the clustering itself.

During the pre-clustering stage, we loop over pads in the bending and non-bending planes of the detection elements to form groups of contiguous pads. The overlapping groups of pads are merged from both cathodes to build the pre-clusters that are the objects to be clustered. The aim of the algorithm is then to unfold each pre-cluster in order to extract the number and the position of individual clusters merged in it. Several algorithms are available, with different degrees of complexity and performed.

Track reconstruction. The MUON code provides two different algorithms to reconstruct a muon trajectory. In both cases the general tracking procedure is the same, the only difference being the way the track parameters are computed from the cluster positions. The "original" algorithm performs a fit of the tracks parameters using the MINUIT package of Root, while the Kalman algorithm [Chabratova 2003a],[Chabratova 2003b] computes them using analytical formulae. The second (used by default) is faster than the first one, but it's also more sensitive to the correctness of the estimated cluster resolution.

The general tracking procedure is as follows:

1. Built primary track candidates using clusters on station 4 and 5. Make all combinations of clusters between the two chambers of stations 5 (4). For each combination, compute the local position, direction and impact parameter of the tracklet at vertex, and estimate its bending momentum assuming that the track is coming from the interaction vertex. Compute the corresponding error and covariances of these parameters. Then select the pairs of clusters for which

the estimated bending momentum and the non-bending impact parameter at vertex are within limits defined in the reconstruction parameters, taking into account the errors.

2. Extrapolate the primary track candidates from station 5 (4) to station 4 (5), look for one compatible cluster to validate them, recompute the track parameters and covariances. The new cluster(s) to be attached to the track are selected according to their local χ^2. If several compatible clusters are found on the same chamber, the track candidate is duplicated to consider all the possibilities.

3. Remove the identical track candidates (i.e. those sharing exactly the same clusters), and the ones whose bending momentum and non-bending impact parameter at vertex are out of given limits.

4. Propagate the track to station 3, 2 then 1 and, at each step, ask the "Cluster Server" to provide clusters in the region of interest defined in the reconstruction parameters, and select the one(s) compatible with the track. The track is validated if we find at least 1 cluster per station and if its re-computed bending momentum and non-bending impact parameter at vertex are within given limits taking into account the errors.

5. Remove the connected tracks, (i.e. the ones sharing one cluster or more) keeping the one with the larger number of clusters. Then recompute the track parameters and covariances at each attached cluster with Kalman tracking method[Chabratova 2003b]).

6. The reconstructed tracks are finally matched with the trigger tracks to identify the muon(s) responsible for the trigger signal. The χ^2 cut for trigger track matching is also part of the reconstruction parameters.

Also atmospheric muon tracks crossing the FMS are reconstructed following the procedure now described with some variations to keep into account that they do not have an interaction vertex point like particles in p-p collisions. One single muon track will be reconstructed only if it has at least nine clusters, therefore it has to cross all the five stations of the spectrometer plus the two trigger chambers (see Fig. 4.5). Their angular acceptance, following the coordinate system for cosmic convention (see appendix A), is given by a zenith angle Θ within the range 60^o to 90^o and azimuth angle Φ within the range 70^o to 105^o.

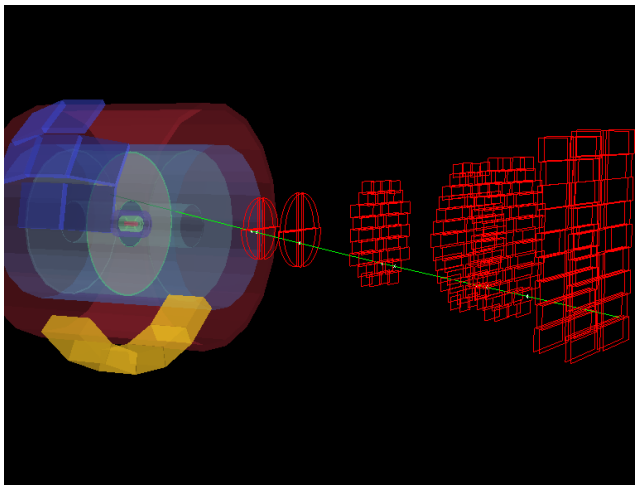

Figure 4.5: A single muon track (green line) crossing all the chambers of the FMS.

4.3 Momentum Measurement of Atmospheric Muons

4.3.1 Muon momentum measurement in the TPC

Since the TPC is embedded in a magnetic field B parallel to its electric field, the transverse momentum of any charge particle traversing the gas volume can be determined through the curvature C of the track projection on the pad plane provided by the x and y coordinates measured by the read-out chambers (for a schematic view see Fig. 4.6) according to:

$$p_T(GeV) = 0.3 \cdot \frac{B}{C}(Tm); \tag{4.1}$$

The transverse momentum error is given by the azimuthal resolution of a single space point, $r\delta\phi$, calculated in the local frame which approximates the particle trajectory with a parabola. It can be described by [Gluckstern 1963]:

$$\frac{\Delta p_T}{p_T^2} = \frac{r\delta\phi}{0.3 \cdot B \cdot L^2}\sqrt{\frac{720}{n_{cl}+4}}; \tag{4.2}$$

where L is the total visible track length and n_{cl} denotes the number of track points. Whereas B and L are given by the overall design of the ALICE TPC, the azimuthal position resolution $r\delta\phi$ is influenced by [W. Blum 2008]:

- The amount of ionization contributing to the individual space point measurements.
- The diffusion broadening of the electron cloud during drift.
- Fluctuations in the gas amplification of single electrons, which effectively enhance the delocalization caused by diffusion by a factor $\sqrt{2}$.

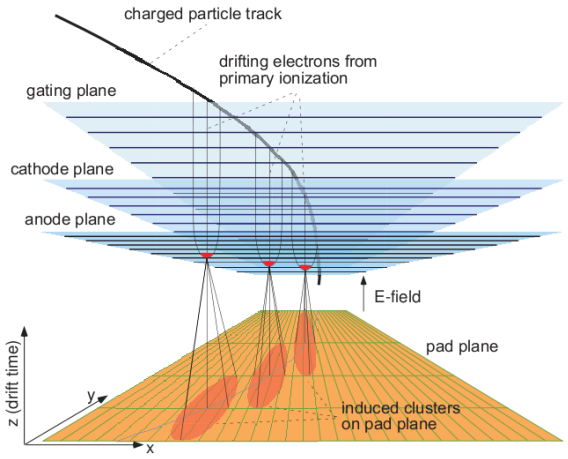

Figure 4.6: Schematic illustration of the working principle of a multiwire proportional chamber with segmented cathode.

- E and $E \times B$ effects due to the non-homogeneity and muon-parallelism of the fields.

All these effects decrease the momentum resolution. Also a poor track point determination, as the case for high momentum particles, leads to a worse momentum resolution.

More than 70% of the atmospheric muons reaching ALICE have a momentum less than 100 GeV/c. As a first approach we can foresee to perform measurements up to this value. Since the TPC standalone is optimized for lower momentum values, of the order of less than 10 GeV/c, a detailed study of the performances of the detector for high momentum muons will be necessary to understand the limits in the measurements and in case how to improve them.

As described before, most of the muons crossing the TPC have two tracks (up and down, see section 4.1.1) and the matching algorithm reconstructs one muon track from them. In order to have an estimate of the momentum resolution using a sample of real data we have selected only events with two tracks and one muon reconstructed. In this way the sample to be analysed is very clean.

Using real data we have two possibilities to define the value of the total momentum P. Taking advantage that each muon is composed by two tracks and that TPC standard tracking method assigns a momentum and its error for each track (p_{up},σ_{up} and p_{down},σ_{down}) we define :

$$P_{mean} = \frac{p_{up} + p_{down}}{2}; \tag{4.3}$$

and,

$$P_{weight} = \sqrt{\frac{\sigma_{up}^2}{\sigma_{up}^2 + \sigma_{down}^2}} \cdot P_{up} + \sqrt{\frac{\sigma_{down}^2}{\sigma_{down}^2 + \sigma_{up}^2}} \cdot P_{down} \tag{4.4}$$

where, P_{mean} is the standard mean value between up and down momentum, while P_{weight} weights the two momenta keeping into account their errors.

The correlation between these two momenta is good, as we can see from Fig. 4.7 in which is plotted P_{mean} vs P_{weight}, therefore in the following we choose P_{weight} as measurement of the muon momentum.

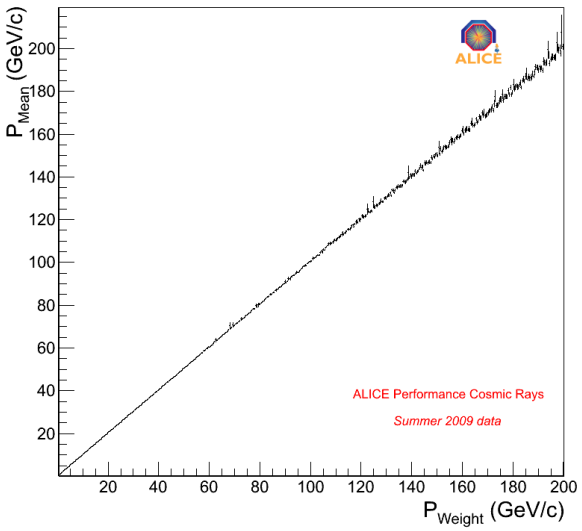

Figure 4.7: Correlation between P_{mean} and P_{weight} defined from Eq. (4.3) and (4.4) as a measurement of the momentum of a muon reconstructed from two tracks in the TPC.

In order to estimate the resolution (R_μ) of the momentum using experimental data, we define:

$$R_\mu = \frac{1/p_{T_{up}} - 1/p_{T_{down}}}{(1/p_{T_{up}} + 1/p_{T_{down}})/2}; \tag{4.5}$$

where $p_{T_{up}}$ and $p_{T_{down}}$ are the transverse momentum of up and down tracks. The resolution is defined as a function of $1/p_T$ because (as described before) it is proportional to the curvature of the track (see Eq. 4.2) and its probability density function should be Gaussian. Thus, the resolution value is given as the Gaussian width of the R_μ variable for different interval of the momentum (P_{weight}) and it is shown in Fig. 4.8 for some experimental data runs. The error is stable and do not depend on the run, its value is around 50% at $P_{weight} = 100$ GeV/c.

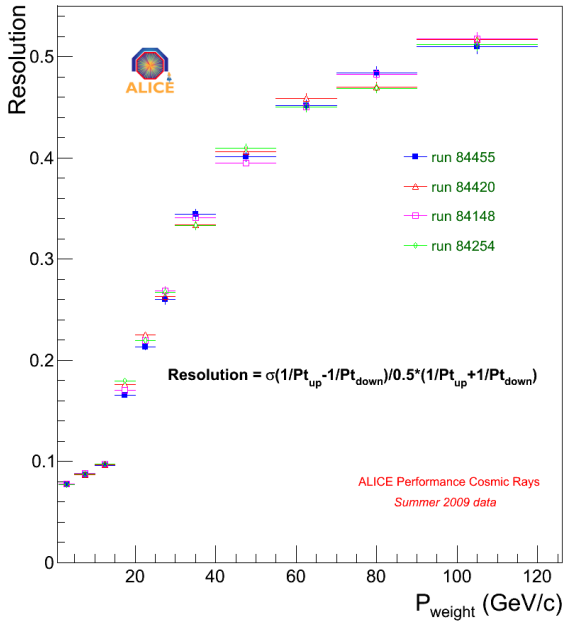

Figure 4.8: Muon momentum resolution $\sigma_{P_{weight}}$ for various runs.

Although a cut on the minimum number of clusters of the track can improve the momentum resolution, nevertheless its effect is also to remove real muon crossing a limited part of the TPC or a region of inefficient detection. To improve the momentum resolution especially, at high momenta, we have to use the total length of the muon track (up and down) and perform a fit of this long track (refit) taking advantage that an atmospheric muon usually crosses the whole diameter of the TPC cylinder.

Since the standard method measures the momentum up and down separately a new method written specifically for atmospheric muons has been developed to calculate the momentum employing the whole length of the track. Some simulations have been performed to perform and study this method.

The simulation has been done with the following steps :

- Simulation of the points of the muon tracks in the TPC. The points start in the top of the TPC, and are propagated up to the central longitudinal plane of the TPC cylinder (track up). The points start in the central plane for the track down of the muon.
- Adding to the space points smearing and misalignment according to the TPC spatial resolution.

- Fitting the space points to reconstruct the whole track.

The normal fitting procedure using only the point of the track up or the track down separately has been changed to fit all the points together and obtaining a momentum that we define as (P_{refit}). This measurement of the momentum has a better resolution than the previous ones because uses the whole track of the muon but has the disadvantage that all the reconstructed tracks previously obtained with the standard method of the TPC have to be recalculated starting from raw data.

Another method giving the same results of the refitting algorithm but without using the raw data has been developed and studied with Monte Carlo simulations. Starting with the event summary data (ESD), in which all the parameters of the reconstruction track has been given in the frame of the Kalman filter, the new calculus keep into account all these information written in the covariant matrix of the track up and track down. In this way the algorithm update the parameters of the covariant matrix of track up with the covariant matrix of the track down, giving a result equivalent to fit the whole TPC track (refitting method) but without using the raw data.

The goodness of this method is visible in Fig. 4.9 in which the inverse of transverse momentum obtained with the covariant matrices P_{cov} is compared with the momentum given by P_{refit}.

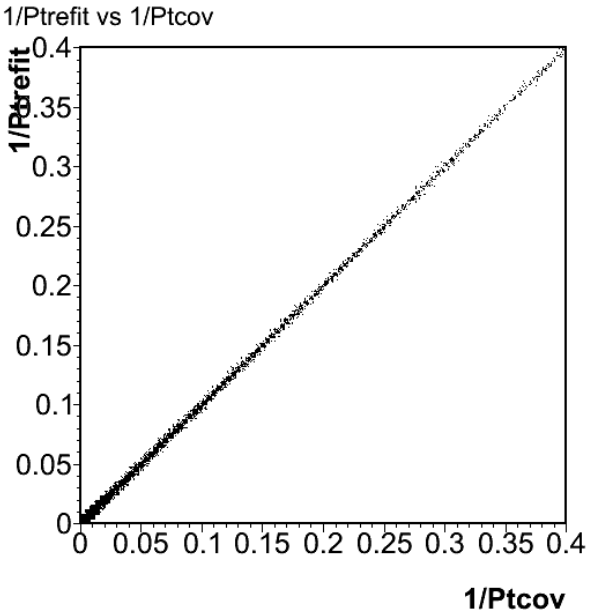

Figure 4.9: Correlation between $1/Pt_{refit}$ and $1/Pt_{cov}$. The two methods of measuring the momentum give the same results.

The momentum resolution of P_{cov} has been studied simulating single muon events of different energies and comparing this value with the momentum simulated P_{sim}. The whole chain of detection and reconstruction in the TPC for real data has been used and the results are summarize in Fig. 4.10. The resolution at $P_{cov} = 100$ GeV/c is about 30% with a gain of a factor 1.7 with respect the standard method (P_{weight}).

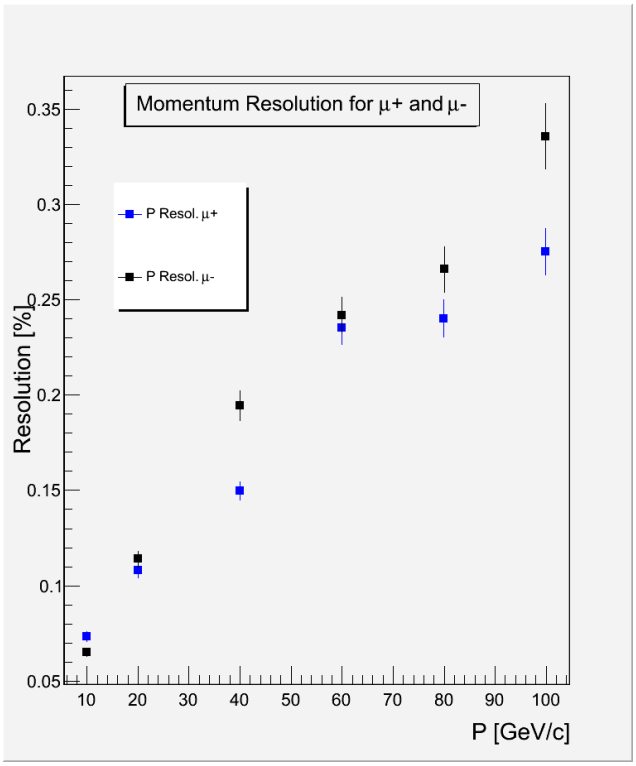

Figure 4.10: P_{Cov} resolution for μ^+ and μ^- as a function of the momentum up to 100 GeV/c, obtained by MC studies.

4.3.2 Momentum measurement in the FMS

The FMS has a dipole magnet with a maximum central field $B = 0.7$ T and an integral field of 3 Tm, oriented along the X axis (see appendix A). The deflection of the muon is in the yz plane (see Fig. 4.11). The Lorentz force provides a centripetal acceleration v^2/ρ directed along the bending radius. Since incident muons into the spectrometer are parallel to the z axis, i.e. $|\vec{p}| = p_z = p$, where $\vec{p}$ is the momentum of the muon to be measured. Then one can get (for $\vec{p} \perp \vec{B}$),

$$\frac{mv^2}{\rho} = evB_y, \tag{4.6}$$

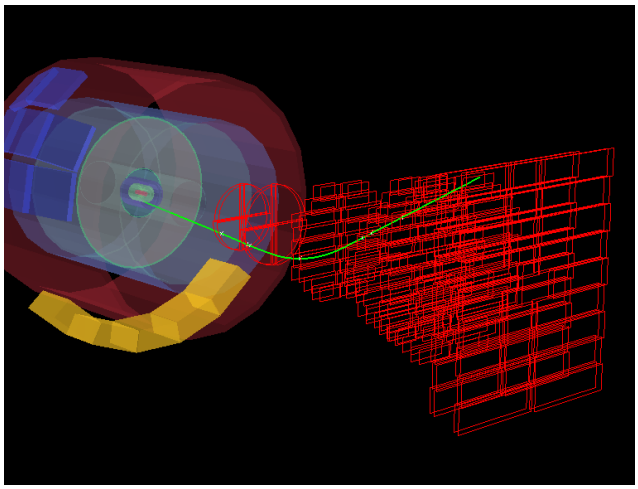

Figure 4.11: An horizontal muon track bending in the yz plane.

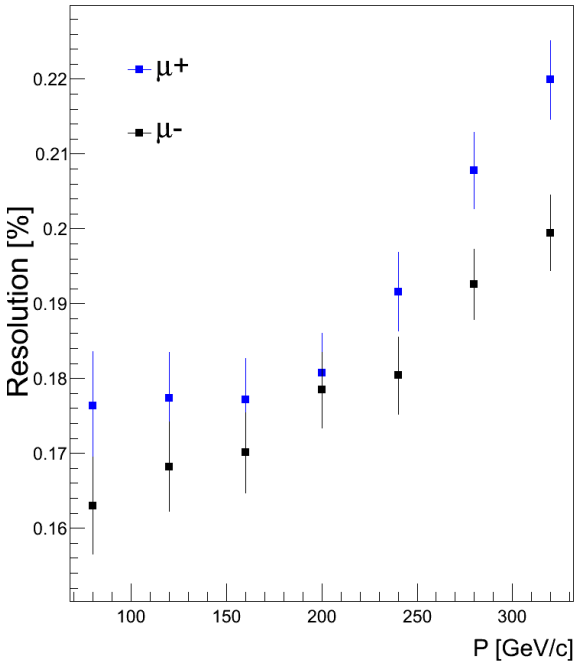

Figure 4.12: The momentum resolution up to 320 GeV/c at surface level for horizontal muons.

where, m is the mass, v the muon velocity and ρ the bending radius of the muon track in the magnetic field. Then the *bending radius* ρ will be,

$$\rho = \frac{p}{eB_y}. \tag{4.7}$$

We have estimated with simulations (see Fig. 4.12) a resolution better than 18% for horizontal muons with momentum of 100 GeV/c.

Chapter 5

Analysis of Atmospheric Near-Vertical Muons

Contents

In this chapter the analysis of atmospheric muons collected in the central barrel of ALICE in Summer 2009 and February 2010 is presented. In particular the *near-vertical muons*, defined as those events in which the muon directions is within zenith angle range $0^0 - 20^0$ will be studied in detail. A preliminary ALICE measurement of the muon charge ratio $R_\mu(\mu^+/\mu^-)$ will be given.

5.1 Introduction

The calibration, alignment and commissioning of most of the detectors of ALICE have required a large amount of cosmic events taken during Summer 2009. Most of these data have been analysed from various working groups to understand and improve the performances of the involved detectors while only a little sample had the characteristics necessary to perform some measurements on atmospheric muons. To fit these features the run must have :

- the highest magnetic field possible (B = 0.5 T) in such a way to sweep away the low momentum particles from TPC and allows a good matching between track up and down of the muons, and to achieve the best momentum resolution especially for high momentum particles.
- at least one hour of data taking to check the stability and quality of the run.
- good calibration and alignment of the detectors involved to reduce the systematic errors and to have reasonable resolution in the observables.

Since during this period the main works were focused on detector performances and continuous changes of the run conditions were adopted to improve them, only short periods of data taking have, at the end, the required characteristics for cosmic studies. The runs with these qualities, collected during Summer 2009 and February 2010 have been analysed for cosmic studies.

The trigger conditions, the data sample and the event selections will be described in the following two sections. Some characteristic of the events like muon and angular multiplicity will be given and discussed with the purpose to introduce the proper selections to measure with a good precision the μ^+/μ^- ratio. Finally, and extended description of the analysis performed to obtain the preliminary measurement of this ratio will be given.

These results are considered preliminary for two reasons : the first is that the statistics collected (only 2.5 days) has to be increased, the second is due to the necessity to take data reversing the magnetic field in such a way to better evaluate its effect on the ratio and decrease the systematic errors. At this purpose this year (2011) is planning to take cosmic data during ALICE standard data taking with multiple benefits : collection of a large number of events, very good calibration and alignment of the involved detectors continuously checked, alternate periods with magnetic field in one direction and in the opposite.

5.2 Description of the triggers for atmospheric muons

Specific triggers have been implemented to detect atmospheric muons crossing the apparatus. As described in a previous chapter, three detectors have been used at this purpose : ACORDE, TOF and SPD.

ACORDE has 60 scintillator modules located on the top of the three upper side octants of the L3 magnet structure. It can give a flexible trigger with a coincidence of the signals in various modules or also a single hit coincidence (one module fired). The rate for single hit is about 100 Hz while the rate in a two-fold coincidence (two modules fired) decreases at around 1 Hz. In the data of Summer 2009 the detector was implemented with a double coincidence and this trigger is called ‘ACORDE MULTIMU (AMU)‘ (see Fig. 5.1a). With this trigger the 7% of the recorded events have at least one muon crossing the TPC (purity of the trigger).

The TOF is a cylindrical MRPC array with a very large area surrounding completely the cylinder of the TPC. For these characteristics it is the ideal detector for triggering the atmospheric muon crossing the ALICE central detectors. The trigger conditions are very flexible and can be easily changed by software. In our cosmic data two types of triggers were implemented. The first called ’TOF SINGLE (OB3)‘ requires one pad fired in the upper part of the TOF and the corresponding

opposite pad in the down part plus the three closest down pads in the opposite sides (3+central+3) as shown in Fig. 5.1b. This configuration is necessary to take into account the curvature of the muon in the magnetic field. This trigger selects mainly single muon. The second trigger called 'TOF COSMIC (OCP)' is given by the coincidence of the signal in four pads regardless of their position (Fig. 5.1c). It is a compromise to get a low trigger rate, good purity and full efficiency for high multiplicity events (> 3 muons).

The last trigger is given by the SPD, composed from two layers of a silicon pixel modules located very close to the interaction point of the p-p collisions. It is a very small size detector, in these data mainly used for the alignment of the ITS detectors. The trigger is given by the coincidence of two signals in the opposite half of the external layer (Fig. 5.1d). It is seldom used in our analysis for its small size giving a poor statistics, but it could be important for selecting, with a very large statistic data, a sample of events in which the muon can be tracked with the TPC and ITS together. This sample should be very clean and with very high resolution of the quantities measured.

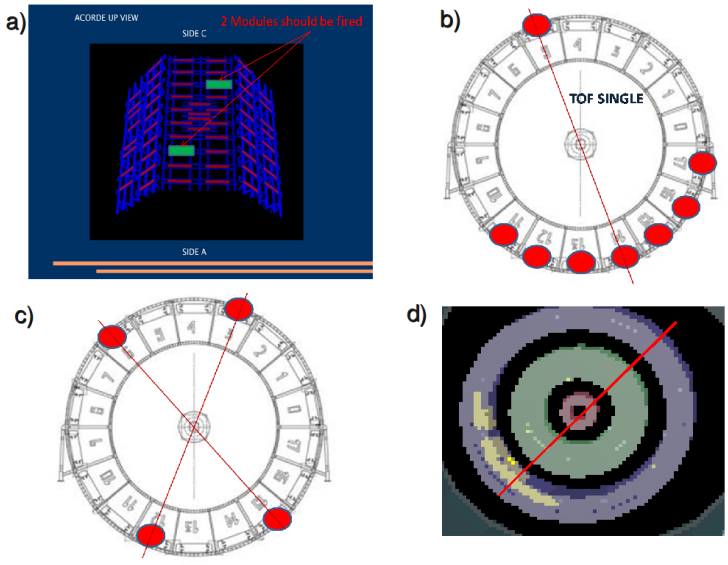

Figure 5.1: A schematic view of the four triggers implemented to detect atmospheric muon crossing the ALICE central detectors : *a*) ACORDE (AMU), *b*) TOF (OB3), *c*) TOF (OCP) and *d*) SPD (SCO).

In Fig. 5.2 is given the distribution of the trigger types for all the sample of events taken in Summer 2009. The correspondence of the type number and the main triggers is the following :

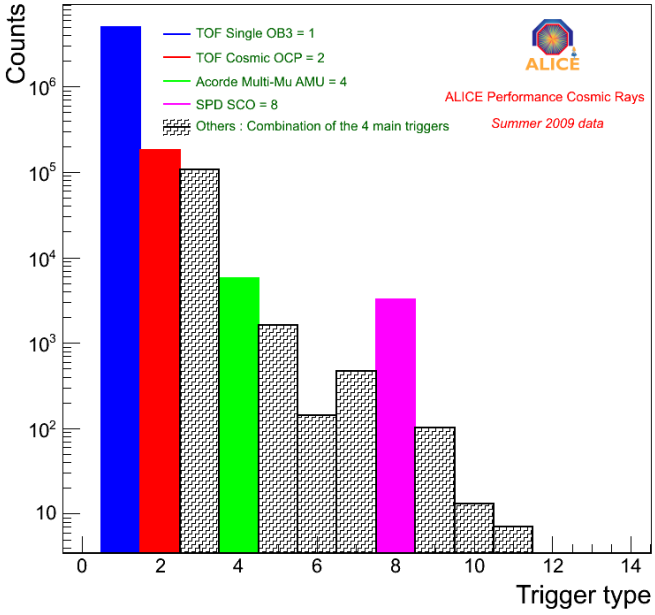

Figure 5.2: Trigger type distribution for the four main triggers and combinations of them.

- OB3 in blue with trigger type = 1
- OCP in red with trigger type = 2
- AMU in green with trigger type = 4
- SCO in violet with trigger type = 8

The others are a combination of these main triggers, for example trigger type = 3 is OB3 AND OCP).

Most of the events are given by 'TOF SINGLE (OB3)' trigger, while 'TOF COSMIC (OCP)' selects a slightly higher multiplicity but its rate is a factor 20 lower than OB3. 'ACORDE MULTIMU' has a very low rate because requires a coincidence of two scintillators while 'SPD TRIGGER' rate is low for the small size of the detector.

5.3 Data sample

The data taken in Summer 2009 and February 2010 with the triggers described in the previous section are summarized in Table 5.1 and Table 5.2 respectively. In particular it is given : the number of the run, the duration, the total number of events collected, the number of events with at least one muon in the TPC, the number of events per second with at least one muon in the TPC for each trigger, the number of events in which the muon interacts in the iron structure or everywhere creating a shower of particles, the number of multimuon events (number of muons > 3).

We can see that in 2009 about 2.5 days of live time for cosmics were collected with more than half million events with muons in the TPC and around 2 days in 2010 with only about 25000 events. The difference is due to the absence of the TOF in the trigger detectors in 2010. Most of the 2009 statistics is given by the trigger 'TOF SINGLE (OB3)' and 'TOF COSMIC (OB3)', with a rate of muon events of 25 Hz and 1.5 Hz respectively while the other triggers have a rate much lower than 1 Hz.

N.Run	Time[h.m]	N.Events	N.Events $N\mu > 0$	Rate[Hz] $N\mu > 0$ OB3	Rate[Hz] $N\mu > 0$ OCP	Rate[Hz] $N\mu > 0$ AMU	N.Inter. Events	N.Multimu Events $N\mu > 3$
83811	9.48	3422599	719832	20	1.0	0.03	152	152
83775	1.27	580925	148666	30.1	1.8	0.05	29	19
83802	1.05	382985	81830	20.5	1.1	0.03	18	15
84148	6.40	2720090	682773	28	1.6	0.04	103	98
84205	4.50	1681171	424331	24.7	1.4	0.04	84	76
84254	7.00	2330994	587554	22	1.3	0.03	99	81
84389	2.23	599723	151642	17.8	1.0	0.03	33	34
84420	5.12	1958776	495292	25.4	1.4	0.04	80	92
84455	4.43	1883982	478493	28.3	1.6	0.04	98	82
84479	1.00	377985	96761	25.4	1.5	0.04	19	18
84993	1.52	460389	120291	20.7	1.2	0.03	17	24
85024	1.35	493870	128554	24.9	1.4	0.04	18	18
85031	0.51	304872	79945	41	2.4	0.06	9	10
85032	0.43	14388	3759	2.3	0.13	0.004	1	0
85034	11.00	3906585	1023590	24.4	1.4	0.04	197	161
Total	57.29	21119334	5223313				957	880

Table 5.1: Summary of the main characteristics of data collected in Summer 2009 with central detectors : ACORDE, TOF and SPD for trigger and TPC for tracking.

In the analysis below we analyse only the standard events (single muon or multimuon), discarding the interaction events with the method described before.

N.Run	Time[h.m]	N.Events SCO AMU	N.Events $N\mu > 0$ SCO AMU	Rate[Hz] $N\mu > 0$ SCO	Rate[Hz] $N\mu > 0$ AMU
109432	12.9	11070	6043	0.12	0.01
109477	3.4	3010	1653	0.12	0.01
109547	5.2	4601	2476	0.12	0.01
109576	2.3	2032	1075	0.12	0.01
109580	4.6	3732	1985	0.11	0.01
110499	4.8	2604	1869	0.10	0.003
110519	1.4	643	460	0.10	0.002
110520	7.3	4679	3305	0.12	0.004
110651	4.2	2610	1846	0.12	0.004
110865	6.3	13595	4353	0.19	0.004
Total	52.4	48576	25065		

Table 5.2: Summary of the main characteristics of data collected in February 2010 with central detectors : ACORDE and SPD for trigger and TPC for tracking.

5.4 Muon multiplicity distribution and angular distribution

Adopting the tracking algorithms and the selection criteria previously explained we have studied our samples of data. The muon multiplicity distribution of 2009 data is shown in Fig. 5.3 for the four trigger types ACORDE (AMU), TOF (OB3), TOF (OCP), SPD (SCO) (see Section 5.2). The maximum number of muons found in this period is 35.

Since the statistics of our sample is given by only two days and half of live time, a period too short to perform composition analysis with these distributions, we have limited ourselves to compare the sample with some simulations to check the consistency. We have simulated a greater statistics with respect real data, in order to find possible anomalies in the muon multiplicity of some events, as reported by previous experiments [Avati 2003],[Abdallah 2007]. We have written a simplified simulation to estimate the multiplicity distribution expected in ALICE for 30 days of data taking. Supposing pure proton and pure iron composition and adopting Corsika code and QGSJET2 [D.Heek 1998],[N.N.Kalmykov 1989] as hadron interaction model the result of the simulation is given in Fig. 5.4 and compared with real data suggests a standard behavior of our 2009 sample.

The muon multiplicity distribution for the period February 2010 shows instead two events with very high multiplicity that appear somewhat anomalous, as we can see in Fig. 5.5 . These events seem difficult to explain with actual Monte Carlo simulation as we can deduce comparing the simulated and the real multiplicity distribution. One event has 89 muons with a density of $\sim 6\mu/m^2$ and the other 182 muons with a density of $\sim 12\mu/m^2$. We have estimated that both these events

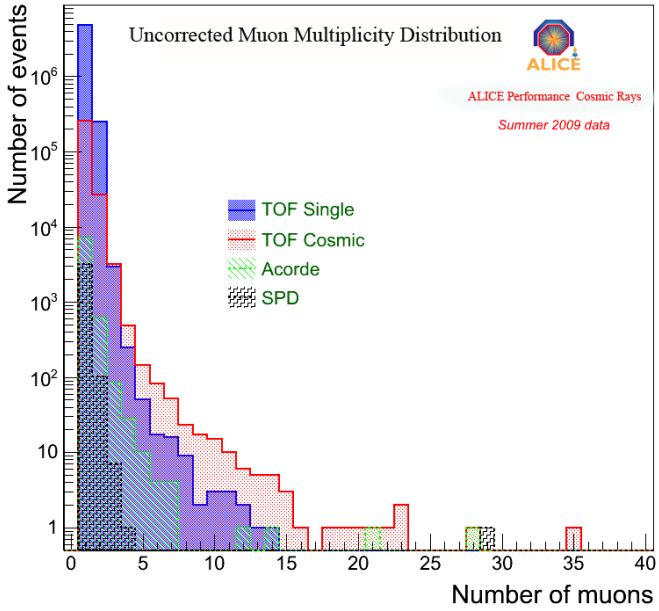

Figure 5.3: Muon multiplicity distribution of data sample of summer 2009 for the four trigger types ACORDE (AMU), TOF (OB3), TOF (OCP), SPD (SCO).

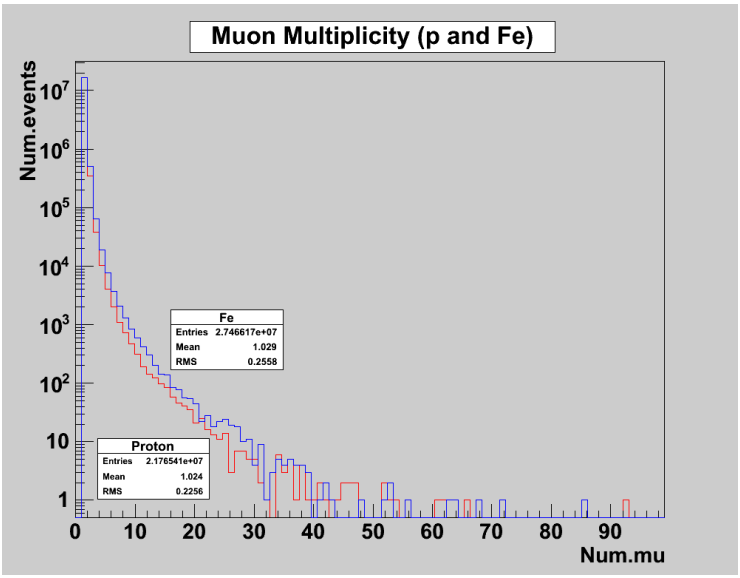

Figure 5.4: Simulation of the muon multiplicity distribution in ALICE in 30 days of data taking supposing a pure proton or pure iron composition.

should be generated from a primary with an energy greater than 10^{16} eV. The

probability to detect such high multiplicity in less than 5 days of data is very low, especially for the highest multiplicity for which we estimate one event in three years of live time. It is probable that these events give an indication of the difficulties of current hadronic interaction models to reproduce data of such energies.

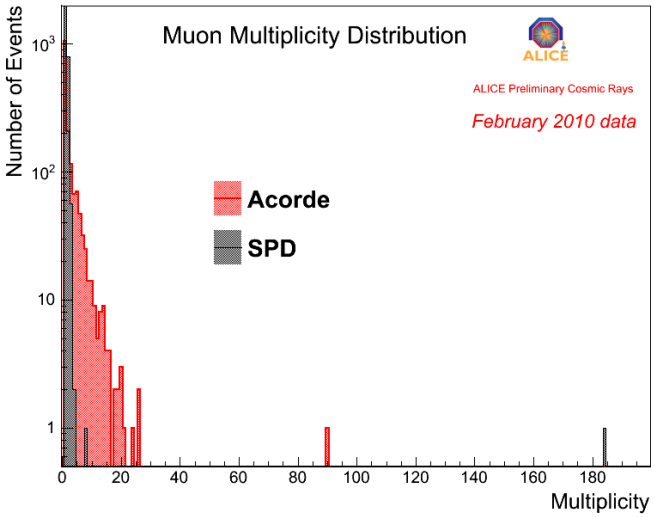

Figure 5.5: Muon multiplicity distribution of data sample of February 2010 for the trigger types ACORDE (AMU) and SPD (SCO).

The reconstruction of multi-muon events and the study of the multiplicity distribution has assured us on the correctness of the whole procedure of finding and selecting muon tracks for high muon density events. With the same procedure we have selected and reconstructed single muon events to a first and preliminary measurement on the μ^+/μ^- ratio. The direction of these events has been studied in order to perform the appropriate cuts on the angles and limit our analysis, with the central detectors, to *near-vertical muons*.

In the ALICE reference system two angles are defined : Θ_x and Θ_y while for cosmic events we define two new angles : θ_c and ϕ_c, where θ_c is the zenith angle and ϕ_c the azimuth angle starting from positive X axis and turning clockwise. A vertical muon crossing the apparatus has $\theta_c = 0^o$ while a horizontal muon has $\theta_c = 90^o$. In Appendix A the reference system and the definition of the angles is explained more extensively.

The θ_c vs ϕ_c distribution for muons selected with 'TOF SINGLE (OB3)' trigger is given in Fig. 5.6. The correlation between these two angles shows an increase in the number of the muons in the direction corresponding to the two shafts PX24 and

PM25 located near the apparatus and shown in the schematic view of the ALICE cavern of Fig. 5.7. The energy loss of a vertical muon crossing the whole length of the rock (molasse) above ALICE is around $15 - 16$ GeV/c and decreases when the muon passes through the shafts increasing the number of the detected muons in these directions (green, yellow and red regions in the figure). Considering that the muons with the zenith angle θ_c in the range $0^o - 20^o$ are not affected by the shafts structure, regardless from the azimuth angle, we define *near-vertical muons* these events.

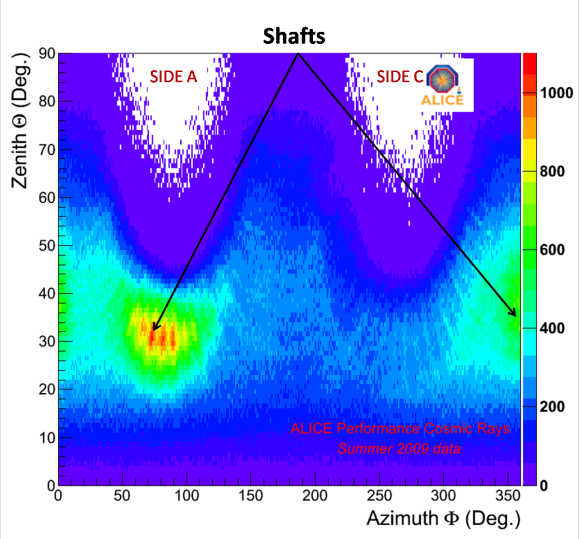

Figure 5.6: Zenith angle vs azimuth angle of the muons arriving in ALICE. The structure of the shafts is visible as an increase of the number of muons in correspondence of their directions.

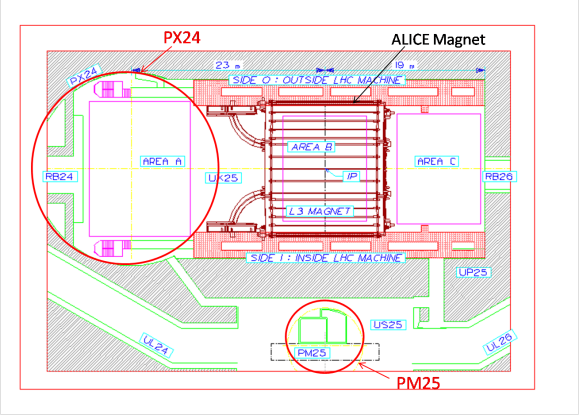

Figure 5.7: Schematic view of the shafts PX24 and PM25 in the ALICE cavern.

We also note a lack of muons at large zenith angles, corresponding to quasi horizontal muons, in two regions (white in the figure) in the corrispondence of the two bases of the cylinder of the TOF (side A and side C in the ALICE convention). Since the TOF do not cover these regions and the trigger is given only from ACORDE at very low rate, the detected events are very rare.

5.5 Measurement of the μ^+/μ^- Ratio

In this section we explain the analysis of the data to obtain the ratio $R_\mu(\mu^+/\mu^-)$ of positive to negative muon numbers for atmospheric muons reaching the ALICE central barrel.

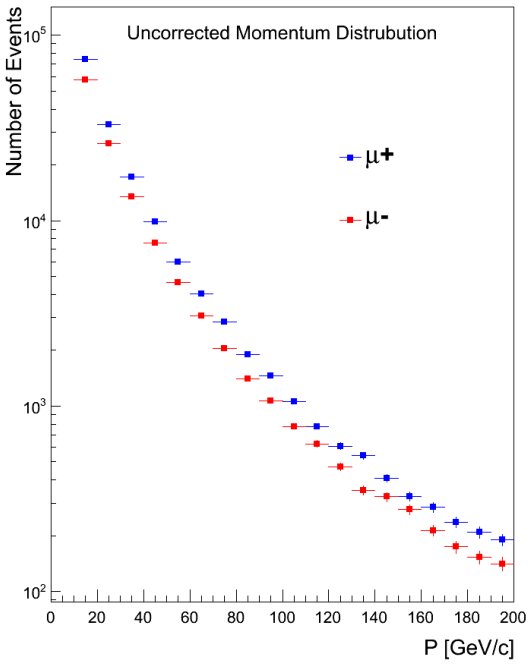

Figure 5.8: Uncorrected momentum distributions for μ^+ and μ^-.

In order to have a sample of events in which all the measured quantities are well understood we will do some cuts after keeping into account the studies described in the previous sections and chapters. In particular we analyse only events with trigger 'TOF SINGLE (OB3)' that has the largest number of events. Single muon events with only two tracks (up and down) in the TPC and satisfying all the matching criteria have been chosen. In this way we eliminate all the problems connected with multi-muons (choosing single muon) and with muons not crossing large part of the TPC (choosing two tracks). Since we want to study only *near-vertical muons* we

require directions in the range of the zenith angle $0^o < \theta_c < 20^o$ in which the effects of the shafts are absent as discussed before. We can deduce from Fig 5.8, in which is plotted the uncorrected muon momentum distribution for μ^+ and μ^- at ALICE level up to $P = 200$ GeV/c, that with these cuts we select a good sample of events in which we do not introduce anomalous behaviours for both the charges.

Conservatively we will study the ratio $R_\mu(\mu^+/\mu^-)$ in the momentum range $10 < P < 100$ GeV/c at ALICE level. We select muons with $P > 10$ GeV/c in order to eliminate the threshold effects of the rock above ALICE, and the large differences in the efficiencies between μ^+ and μ^- at low momentum due to the large curvature of the tracks in the magnetic field. We limit the measurement up to $P = 100$ GeV/c in which the resolution is reasonable $(30\% - 35\%)$ and the effects of the migration of entries from bin to bin are low.

The uncorrected value of the ratio $R_\mu(\mu^+/\mu^-)$ at ALICE level in the range $10 < P < 100$ GeV/c is then given by the ratio between the number of positive muons $N_{\mu^+} = 179456 \pm 424$ and negative muons $N_{\mu^-} = 139550 \pm 374$, therefore $R = 1.286 \pm 0.006$ where the error is only statistical.

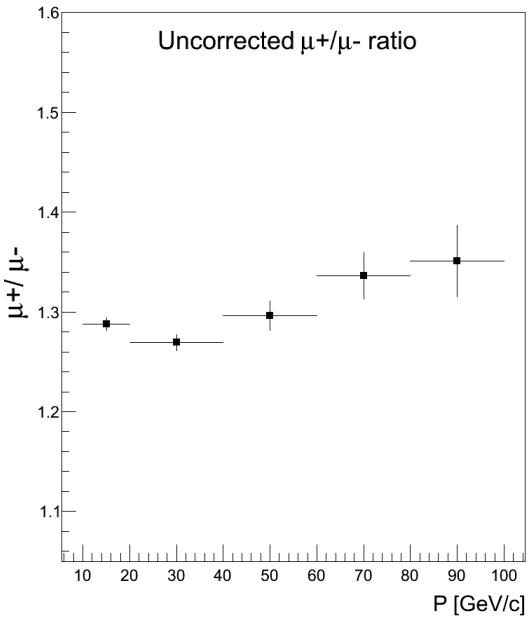

Figure 5.9: Uncorrected μ^+/μ^- ratio for *near vertical muons*.

The uncorrected value as a function of the momentum is given in momentum bins of $\Delta P = 20$ GeV/c (except the first bin $(P = 10 - 20)$ GeV/c) and is shown in

Fig. 5.9.

5.5.1 Corrections for momentum resolution, efficiency and charge misassignment

Since we are studying a ratio, we are not interested in obtaining absolute values in the chosen observables, but it is fundamental to analyse the differences in the detections and measurements between μ^+ and μ^-.

The error in the measurement of the muon momentum increases with the momentum and it is slightly different for μ^+ and μ^-. The effect of the migration of the entries from bin to bin due to momentum resolution has to be evaluated and the values of the ratio corrected.

Monte Carlo simulations generating muons at fixed momentum have been done to obtain the momentum resolution for both μ^+ and μ^-. The events have been detected and reconstructed with the same codes used for real events, that is the chain using ROOT, GEANT3 and AliRoot in which are described in detail all the detectors and their reconstruction methods. In Fig. 5.10 these resolutions are given for both the charges. The estimate of the errors in the whole range of our analysis ($P = 10 - 100$ GeV/c) have been obtained by fitting the points of the resolution at fixed momentum.

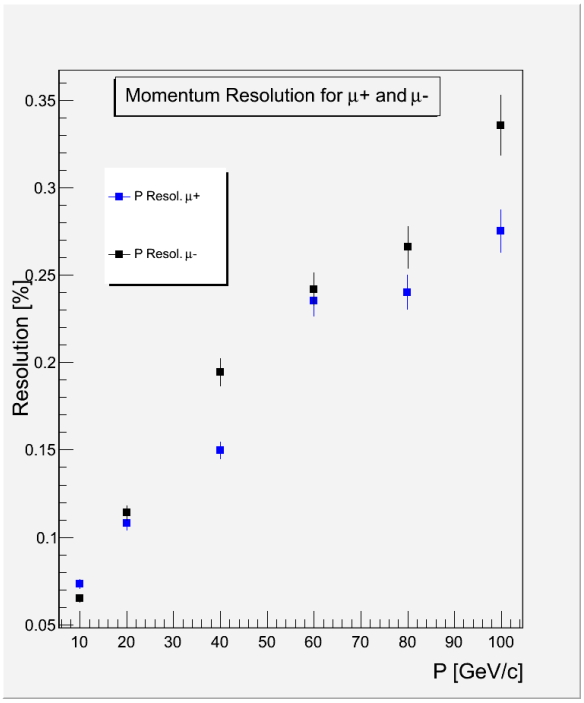

Figure 5.10: Momentum resolution for μ^+ and μ^-.

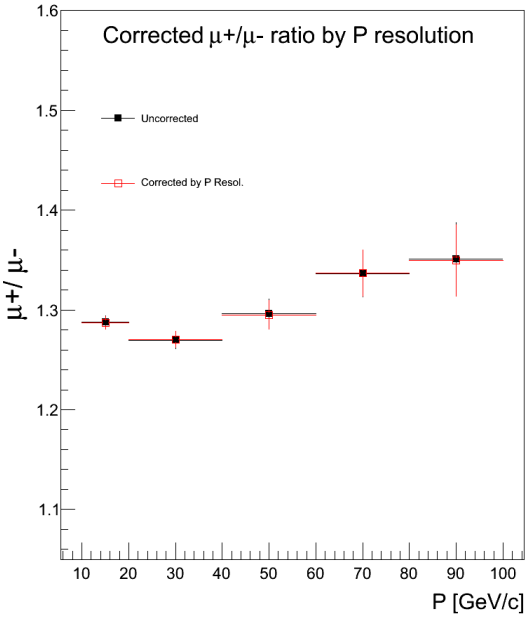

Figure 5.11: Comparison between the uncorrected and corrected (for migration effect) μ^+/μ^- ratio.

The method to correct the migration effect reprocesses the real data, and for each value of the measured momentum applies a correction keeping into account its resolution previously estimated. The new value of the momentum is taken to fill the correspondent bin. The effect of this correction is given in Fig. 5.11, in which the ratio $R_\mu(\mu^+/\mu^-)$ obtained is compared with the uncorrected one. We can see that the migration affects weekly the ratio.

The reconstruction efficiencies as well as the effects of the charge mis-assignment have to be evaluated for further corrections.

High momentum muons have an low curvature and the tracks are almost straight, for these reason the probability to assign a different charge between the track up and the track down is not negligible and these events are eliminated from the analysis. The effect is not only to decrease the efficiency but also to increase the difference in the efficiency between μ^+ and μ^- with the momentum as we can see in Fig. 5.12, making necessary corrections for this effect.

Simulation events in which the two reconstructed charges (up and down) are the same but with the wrong charge with respect on the generated muon give and estimate of the probability to have a charge mis-assignment for different momentum. For the same reason explained above the charge mis-assignment

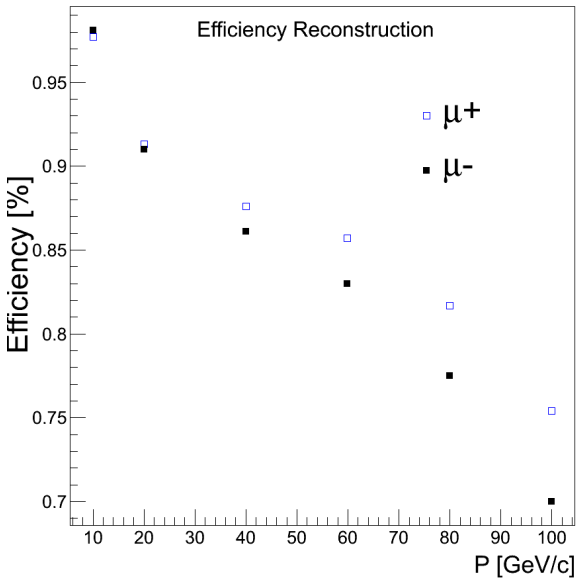

Figure 5.12: μ^+/μ^- efficiencies as a function of the momentum.

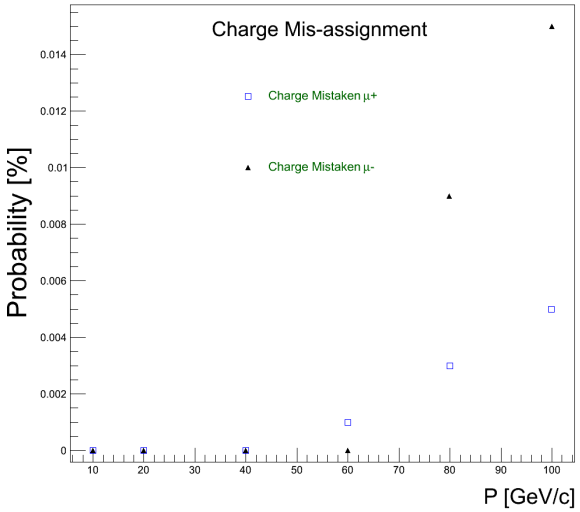

Figure 5.13: μ^+/μ^- mis-assignment probabilities as a function of the momentum.

increases with the momentum and the behavior is shown in Fig.5.13.

The correction of the ratio R for these two effects is calculated with the equation :

$$R_{\mu^+/\mu^-} = \frac{N_{\mu^+}}{N_{\mu^-}} = \left[\frac{(1-q_{\mu^+})N^{Obs.}_{\mu^+} + q_{\mu^+}N^{Obs.}_{\mu^-}}{(1-q_{\mu^-})N^{Obs.}_{\mu^-} + q_{\mu^-}N^{Obs.}_{\mu^+}}\right]\frac{\varepsilon_{\mu^-}}{\varepsilon_{\mu^+}} \tag{5.1}$$

where, $N^{Obs.}_{\mu^+}, N^{Obs.}_{\mu^-}$ are the number of muons μ^+ and μ^- observed after the correction for the migration effect, q_{μ^+}, q_{μ^-} is the misassignment probability for μ^+, μ^- and $\varepsilon_{\mu^+}, \varepsilon_{\mu^-}$ is the efficiency for μ^+, μ^-. The mis-assignment probability and efficiency values are taken using the central value of the momentum bins.

The main results are summarized in Table 5.3. For each bin is given the uncorrected and corrected measurements as well as the mis-asignement probabilities and efficiencies.

	P[GeV/c]	10-20	20-40	40-60	60-80	80-100	10-100
Uncorrected	N_{μ^+}	94213	55896	18139	7868	3340	179456
Data	N_{μ^-}	73162	44033	13994	5889	2472	139550
	R_{μ^+,μ^-}	1.287	1.269	1.296	1.336	1.351	1.286
Corrected	N_{μ^+}	99333	62490	20919	9406	4245	196393
Central	N_{μ^-}	77123	49687	16555	7352	3367	154084
Value	R_{μ^+,μ^-}	1.287	1.257	1.263	1.279	1.260	1.275
	ε_{μ^+}	0.94	0.89	0.86	0.83	0.78	
Central	q_{μ^+}	0	0	0.0005	0.002	0.004	
Value	ε_{μ^-}	0.94	0.88	0.86	0.80	0.73	
	q_{μ^-}	0	0	0	0.0045	0.012	

Table 5.3: Summary of the main results of the Monte Carlo simulations for each momentum interval

The final result of R with all the corrections is given in Fig. 5.14 with the comparison with the uncorrected ratio.

The corrected value of the ratio $R_\mu(\mu^+/\mu^-)$ at ALICE level in the range $10 < P < 100$ GeV/c is then given by the ratio between the number of corrected positive muons $N_{\mu^+} = 196393 \pm 443$ and negative muons $N_{\mu^-} = 154084 \pm 392$, therefore $R = 1.275 \pm 0.006$ where the error is only statistical.

5.5.2 Estimate of the systematic uncertainties and final results

Systematic uncertainties in the ratio can arise to all possible effects that give an asymmetry in the detection and measurements between μ^+ and μ^-. The main asymmetries have been corrected using Monte Carlo simulation, but the uncertainties on these corrections are sources of systematic errors. The instrumental effects like misalignment, acceptance, trigger inefficiencies and uncertainties in the knowledge of the magnetic field map are other sources of systematic errors.

The lower cut in momentum, with the request $P > 10$ GeV/c, removes most of the systematic uncertainties due to a different acceptance between the two types

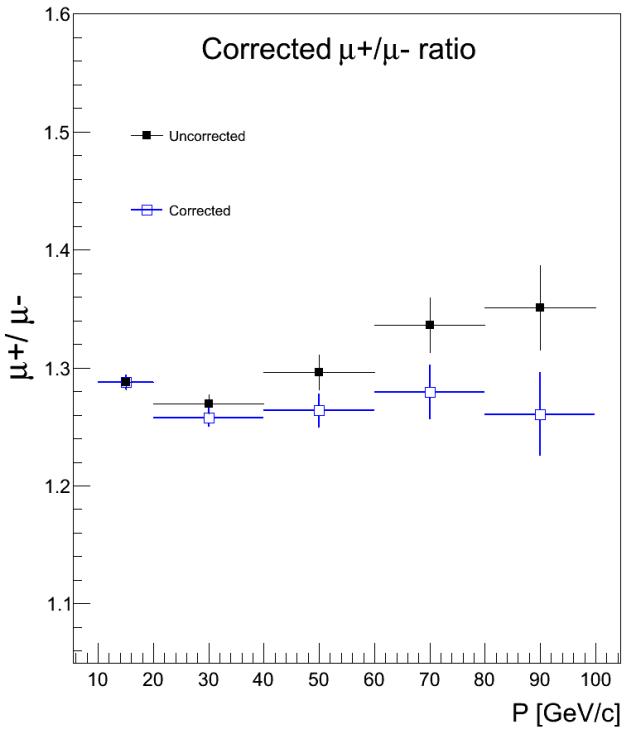

Figure 5.14: Comparison between uncorrected and corrected μ^+/μ^- ratio as a function of the momentum.

of muons, while the upper cut $P < 100$ GeV/c is to keep at an acceptable value the systematic uncertainty due to misalignment. In this interval of momentum the trigger inefficiencies do not affect the ratio and the systematic due to uncertainties in the magnetic field map is negligible.

In order to give an estimation on the systematic errors the analysis has been repeated by calculating the corrections for the efficiency and charge mis-assignment two times : the first time with the values obtained in the lower limit of the bin, the second time using the values of the upper limit.

The results obtained following this method are summarized in Table 5.4. For each bin is given the values of the measurements corrected using the lower and upper limits of the momentum bins for the mis-asignement probabilities and efficiencies. The difference of μ^+/μ^- ratio in each bin is used to evaluated the systematic errors.

The final results with statistical and systematic errors for each interval of

	P[GeV/c]	10-20	20-40	40-60	60-80	80-100	10-100
Uncorrected	N_{μ^+}	94213	55896	18139	7868	3340	179456
Data	N_{μ^-}	73162	44033	13994	5889	2472	139550
	R_{μ^+,μ^-}	1.287	1.269	1.296	1.336	1.351	1.286
Corrected	N_{μ^+}	102815	63809	21148	9634	4421	201828
Upper	N_{μ^-}	80132	51101	16864	7624	3551	159273
Limit	R_{μ^+,μ^-}	1.283	1.248	1.254	1.263	1.244	1.267
Corrected	N_{μ^+}	96080	61223	20694	9189	4083	191269
Lower	N_{μ^-}	74332	48350	16257	7098	3201	149237
Limit	R_{μ^+,μ^-}	1.292	1.266	1.272	1.294	1.275	1.281
	ε_{μ^+}	0.913	0.876	0.857	0.817	0.754	
Upper	q_{μ^+}	0	0	0.001	0.003	0.005	
Limit	ε_{μ^-}	0.910	0.861	0.830	0.775	0.700	
	q_{μ^-}	0	0	0	0.009	0.015	
	ε_{μ^+}	0.977	0.913	0.876	0.857	0.817	
Lower	q_{μ^+}	0	0	0	0.003	0.005	
Limit	ε_{μ^-}	0.981	0.910	0.861	0.830	0.775	
	q_{μ^-}	0	0	0	0.009	0.015	

Table 5.4: Summary of the main results for each momentum interval taken the upper and lower limit of the bin momentum.

momentum is summarized in Tab. 5.5, while in Fig. 5.15 is shown the ratio with the total error for each been. The total error has been calculated adding in quadrature the statistical and the systematic errors.

P[GeV/c]	R_{μ^+/μ^-}	R_{μ^+/μ^-}
10-20	1.288±0.006(stat.)±0.01(syst.)	1.288±0.01(tot.)
20-40	1.258±0.008(stat.)±0.02(syst.)	1.258±0.02(tot.)
40-60	1.264±0.014(stat.)±0.02(syst.)	1.264±0.02(tot.)
60-80	1.279±0.023(stat.)±0.03(syst.)	1.279±0.04(tot.)
80-100	1.261±0.036(stat.)±0.03(syst.)	1.261±0.05(tot.)
10-100	1.275±0.006(stat.)±0.01(syst.)	1.275±0.01(tot.)

Table 5.5: Final results of the $R_\mu(\mu^+/\mu^-)$ ratio for each momentum interval

The final value of the ratio $R_\mu(\mu^+/\mu^-)$ at ALICE level in the range $10 < P < 100$ GeV/c with its statistical and systematic error is : $R_\mu = 1.275 \pm 0.006 \pm 0.01$.

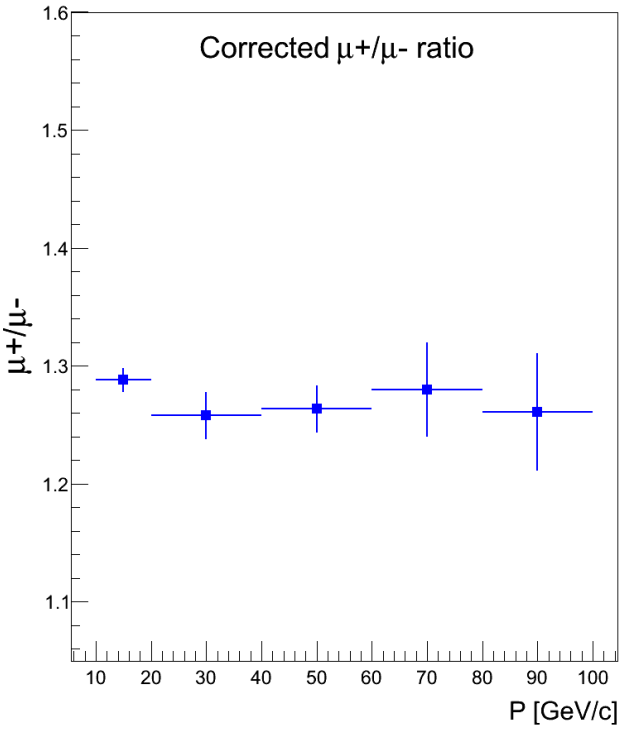

Figure 5.15: Final result of the corrected μ^+/μ^- ratio as a function of the momentum with the total error (statistic and systematic).

Chapter 6

Analysis of Atmospheric Near-Horizontal Muons

Contents

This chapter is dedicated to the analysis of the muons with large zenith angles within the range $70^o - 85^o$, that we call *near-horizontal muons*. These events collected during the Summer 2009 were detected with the Forward Muon Spectrometer (FMS). The selection of a good sample of horizontal events and their main characteristics will be described in order to measure the μ^+/μ^- ratio over a large interval of momentum at surface level.

6.1 Data Sample

During the period of alignment, calibration and commissioning of the FMS detector, an amount of data corresponding to about 9 days of live time have been collected. Due to the geometry of the detector, all the events are muons coming with very large zenith angle ($60^o - 90^o$) after crossing a big amount of atmosphere and of rock above ALICE. In our sample only single muon events have been found. A big dipole magnetic field $B_{Dipole} = 0.7$ T is suitable to distinguish μ^+ from μ^- and to measure their momentum with good resolution up to about 200-250 GeV/c at the level of the apparatus. A summary of the main characteristics of the data can be found in Table 6.1.

We have analysed 51 runs which corresponds to the whole sample of good quality for a total number of events of 207000, with a mean trigger rate of about 25 Hz, while the events with at least one muon reconstructed are only 8192 (4 % of purity). The little number of reconstructed muons is easily understandable if we look at the arrangement of the various tracking chambers with respect the two trigger stations

(see Layout of the muon spectrometer Fig. 3.9), and keeping into account that atmospheric muons are not generated near the collision point and can hit the muon trigger stations without passing in the spectrometer. Another important reason of the low purity is that only muons crossing all the five tracking stations are reconstructed, this is a very stringent cut decided at the reconstruction level to have high resolutions in the measured quantities.

6.2 Event Selection

Two internal variables are defined and recorded in the ESD (Experimental Summary Data) after the tracking reconstruction in the FMS. The first is Θ_x the angle between the z-axis and the projection of the muon track in the xz plane, the second is Θ_y the angle between z-axis and the muon track projection in the yz plane. The connection with the momentum is given by the following equations :

$$\Theta_x = \arctan(P_x/P_z), \tag{6.1}$$

and,

$$\Theta_y = \arctan(P_y/P_z). \tag{6.2}$$

The two trigger stations are located below the tracking chambers and the muon-filter wall looking at the apparatus from the collision point (centre of the experiment). With this arrangement they can trigger atmospheric muons coming from two directions :

- muons coming from side A to side C (see Appendix A) that we denote $A \rightarrow C$, which have a $\Theta_y > 0$ (see Fig. 6.1).
- muons coming from the side C to side A, $C \rightarrow A$, which have a $\Theta_y < 0$ (see Fig. 6.1).

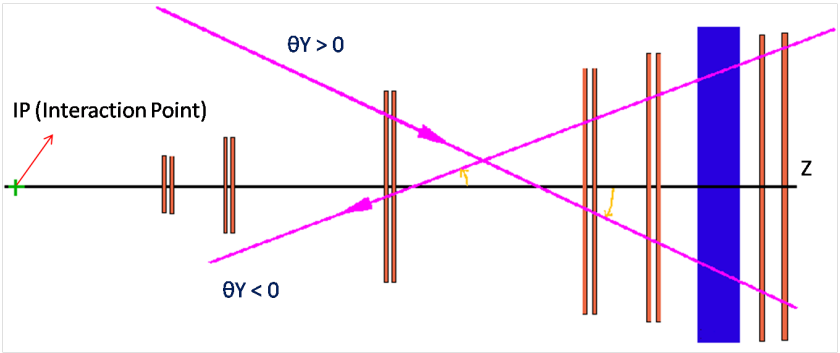

Figure 6.1: The two types of atmospheric muon directions detected in the FMS.

Date	Run	Time[h]	Rate[Hz]	Tot. Events
24/08/09	81185	3	0.24	2560
"	81249	4	0.28	3604
"	81278	1	0.27	1036
25/08/09	81282	2	0.27	2108
"	81286	2	0.26	1882
"	81292	3	0.27	2544
"	81298	1	0.27	1310
"	81315	3	0.27	2625
"	81391	6	0.27	5761
"	81516	4	0.26	4157
26/08/09	81540	4	0.27	3807
"	81544	1	0.23	877
"	81545	4	0.25	3528
"	81683	5	0.25	4032
"	81771	3	0.25	2829
"	81812	3	0.24	2612
"	81818	5	0.28	5104
"	81827	4	0.28	4368
"	81937	4	0.27	4088
"	82118	2	0.27	1734
"	82164	1	0.28	1339
28/08/09	82172	8	0.27	8023
"	82281	3	0.25	2454
"	82339	2	0.26	2255
"	82439	4	0.26	3622
29/08/09	82461	6	0.26	5476
02/09/09	83745	6	0.22	5055
"	83814	2	0.22	1469
"	83822	6	0.26	6044
03/09/09	83845	4	0.26	3621
"	83909	3	0.26	2420
"	83997	5	0.28	4676
04/09/09	84039	5	0.28	4637
"	84046	5	0.28	9819
"	84141	3	0.29	6922
05/09/09	84201	5	0.29	5288
"	84209	3	0.30	3316
"	84228	6	0.28	6625
"	84392	6	0.29	5762
06/09/09	84447	8	0.27	8275
"	84464	6	0.26	5857
"	84585	8	0.27	7622
07/09/09	84643	8	0.27	7692
"	84660	1	0.27	915
"	84815	3	0.27	3237
"	84854	4	0.26	3384
08/09/09	84888	7	0.27	7157
"	85014	1	0.25	1153
"	85021	6	0.24	5541
09/09/09	85052	8	0.25	6778
Total		207		207000

Table 6.1: Summary of the main characteristics of the whole data sample taken during Summer 2009 with the FMS

The direction of the collision events is from the interaction point to the trigger stations, in our notation $A \rightarrow C$. The apparatus is optimized for the events with these directions. Atmospheric muons arriving from the other directions $C \rightarrow A$ in principle should not trigger the apparatus because they fire the second trigger station before the first one. The electronic of the trigger stations requires a charged particle arriving first at the station 1 and then at station 2, but sometimes the temporal interval between the two signals is so close that the trigger fires also for the opposite case (wrong trigger). This is a rare situation for collision events but not for the atmospheric muons, and several of them fire the trigger and cross all the spectrometer being reconstructed as standard muons. In principle they could be analysed, but because the apparatus was designed for muons coming in the opposite directions we have decided to cut these events reducing the statistics but gaining a better sample. We can distinguish them because they have a Θ_y distribution with all negative values while the other directions have positive values as it is shown in Fig. 6.2.

Selecting only events with positive Θ_y values we have reduced the total sample of 8192 events at 5876 events, with total number of positive and negative muons respectively $N_{\mu^+} = 4131$ and $N_{\mu^-} = 1745$.

In Fig. 6.3 is shown the zenith (left) and azimuth (right) distribution of the selected muons. Almost all of the muons have the zenith angle confined within the range $[60^o - 90^o]$, and the azimuth angle within the range $[70^o - 110^o]$. Since the number of muons with zenith angle less than 70^o or greater than 85^o are very little, we have decided another cut in our sample in such a way to analyse only muons in the zenith range $70^o - 85^0$.

6.3 Charge Ratio Measurement

In this section we will give the results of the μ^+/μ^- ratio measurement for *near-horizontal* muons at surface level with a detailed description of the methods followed during the analysis for further cuts, selection bins and correction of the raw data.

As discussed in the previous section, the data sample selected are those events which are within the zenith range $70^o - 85^o$ and $\Theta_y > 0$. Moreover, to avoid a large difference in the acceptance between μ^+ and μ^- for those events with large curvature in the dipole magnetic field only muons with momentum $P > 10$ GeV/c are taken, reducing the sample at 4681 events.

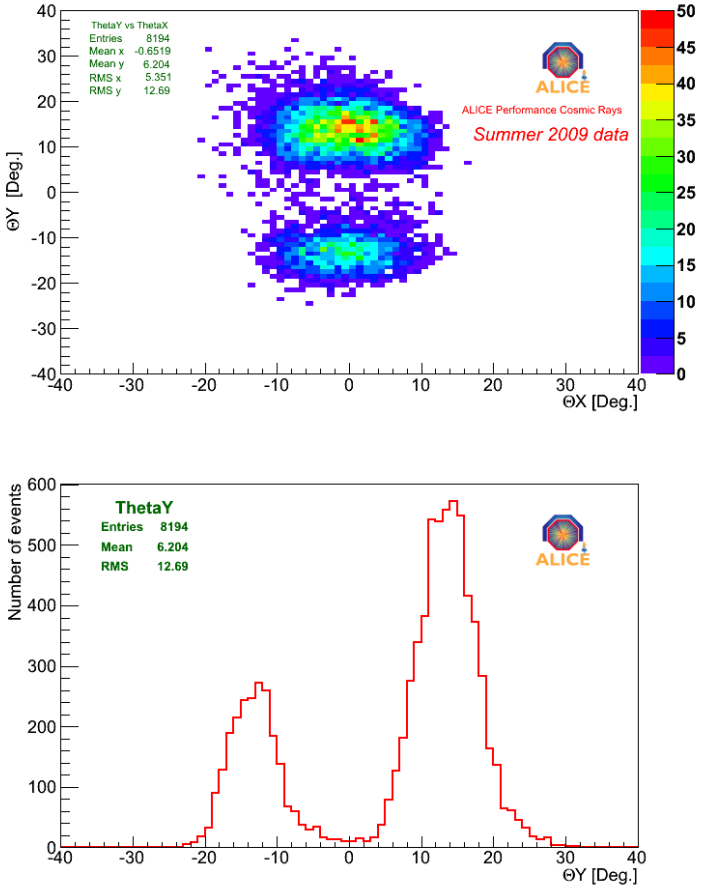

Figure 6.2: In the upper part the Θ_y vs Θ_x distribution, in the lower part the Θ_x distribution, both with all the muons taken with the FMS. A cut $\Theta_y > 0$ selects the events coming from $A \rightarrow C$.

6.3.1 Momentum distribution at ALICE level

The uncorrected momentum distribution for μ^+ and μ^- at ALICE level of our sample, after the cuts described in the previous sections, is shown in Fig. 6.4. We note the large difference in the distribution between μ^+ and μ^- at low momenta that can be explained from the path of the muons. Horizontal muons arrive from the surface, cross the rock above ALICE, enter in the central barrel being affected by its magnetic field and finally after passing through the absorber reach the muon spectrometer. Low momentum muons are strongly affected by the combinations of the L3 magnetic field (central barrel) and the dipole field. Depending on the charge and the orientation of the L3 magnetic field, muons of low momentum are bent a lot and can be swept away before reaching the FMS. While the cut $P > 10$ GeV/c assures a good symmetry in the acceptance for those muons reaching the muon spectrometer it is not sufficient to obtain a symmetric behaviour regarding the muon path before

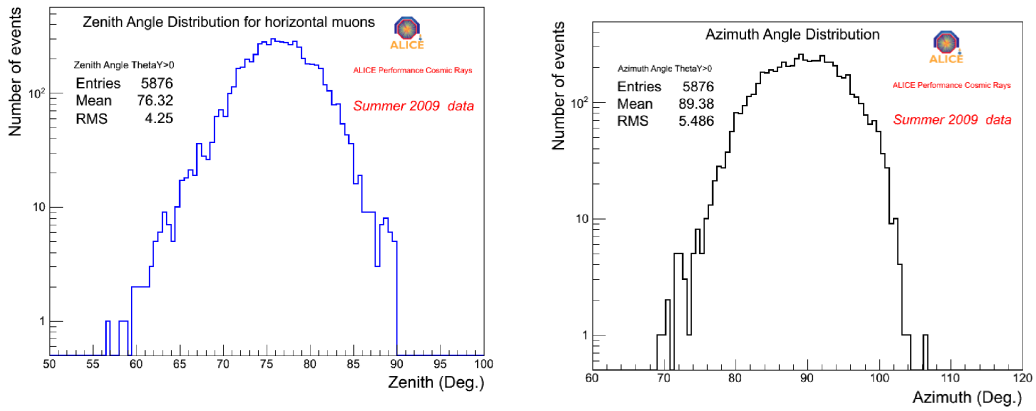

Figure 6.3: Zenith distribution (left) and azimuth distribution (right) for the data sample with $\Theta_y > 0$.

the FMS. This effect influences especially the low momentum muons and should be corrected with simulations. We have seen via Monte Carlo studies (see the next section for details) that with the current polarity of the two magnetic fields (L3 and dipole) we loss many negative muons μ^- of low momentum especially in the range close to zenith angle $\theta_c = 70^o$, the effect is opposite by changing the polarities.

6.3.2 Energy loss

The muons arriving from the surface to the FMS travel a long way in the rock and loss several GeV of energy that depends on the zenith angle. Since we are interested in the value of the μ^+/μ^- ratio at surface level, we have to correct the momentum measured in ALICE for this loss. We have to choose a proper area at surface from which generate muons to calculate this effect and the other corrections discussed in the next sections. This area, shown in Fig. 6.5, has been obtained extrapolating, from the ALICE level up to surface, the coordinates of each muon detected in the real data.

We have generated 5000 μ^+ and 5000 μ^- in this area for each value of zenith angle in the interval θ_c from $70^o - 85^o$ with $\Delta\theta_c = 1^o$, and for 7 different fixed momenta, to obtain the average momentum loss and its fluctuations. The fixed momenta are : 80, 120, 160, 200, 240, 280 and 320 GeV/c. The average value has been calculated from the most probably value of the Landau distribution that fits the simulated points, an example of the fit is shown in Fig. 6.6 for $P = 200$ GeV/c and $\theta_c = 77^o$.

In Fig. 6.7 the mean momentum loss for μ^+ and μ^- for 3 fixed energies is given as a function of zenith angle. The values of the mean momentum loss in the whole angular range are obtained by fitting them with a function of the type:

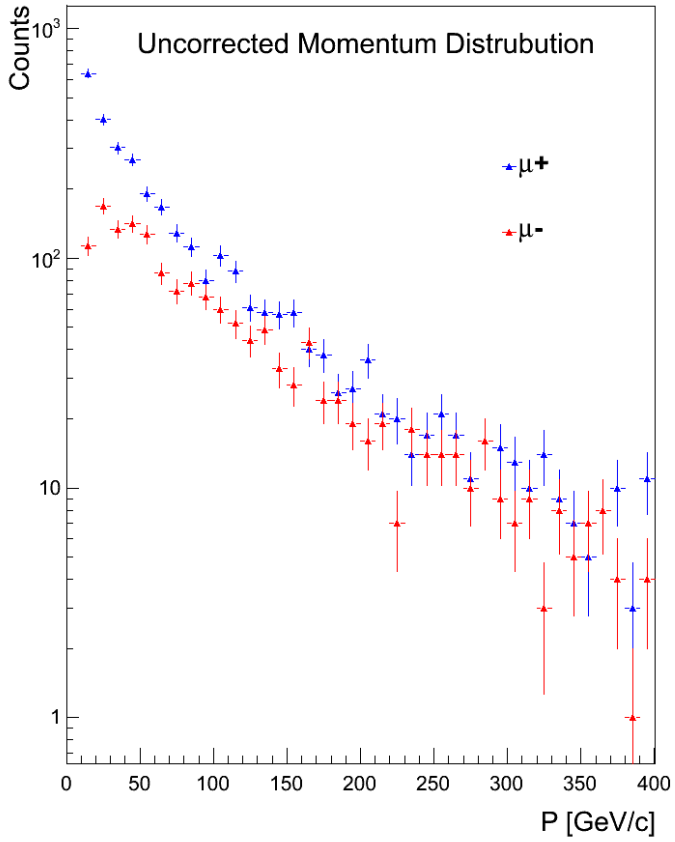

Figure 6.4: Uncorrected momentum distribution for horizontal μ^+ and μ^- up to $P = 400$ GeV/c at ALICE level.

$$\frac{dP_\mu}{d\theta_c} = a + b(1/\cos(\theta_c)) \tag{6.3}$$

As we can see the difference between μ^+ and μ^- in very low and can be neglected in the analysis. To obtain the momentum at surface level, for each measured momentum and zenith angle of the real muon we calculate the momentum loss, keeping into account the fluctuations and using the previous fitted curves, and add this value.

6.3.2.1 Momentum distribution and uncorrected ratio $R_\mu(\mu^+/\mu^-)$ at surface

The uncorrected momentum distribution for μ^+ and μ^- at surface level, after adding the momentum loss as described in the previous section, is given in Fig. 6.8. As explained before for the case of the momentum distribution at ALICE level (see

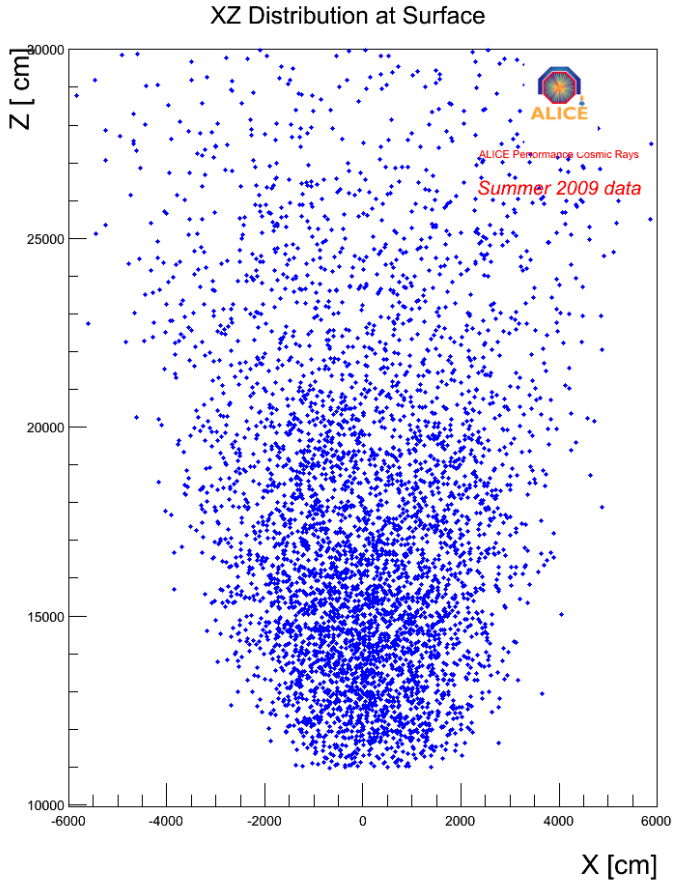

Figure 6.5: X vs Z distribution at surface level of the real data selected. In the simulations every muon is generated at surface according to this area.

Fig. 6.4), the difference between μ^+ and μ^- distributions are big for low momentum muons. This effect is reflected in the same distribution at surface level (see Fig. 6.8) especially for those muons with momentum less than 80-100 GeV/c. Hence, to avoid this large asymmetry we analyse the horizontal muons with momentum at surface greater than $P > 80$ GeV/c, while the upper limit is chosen, keeping into account the resolution and the effects of possible mis-alignment of the tracking chambers, at $P = 320$ GeV/c.

Since the statistics of the horizontal events is reduced we measure the ratio $R_\mu(\mu^+/\mu^-)$ in the momentum range $80 < P < 320$ GeV/c with momentum bin of $\Delta P = 40$ GeV/c. The uncorrected ratio $R_\mu(\mu^+/\mu^-)$ as a function of momentum at surface level is shown in Fig. 6.9.

In the whole range of our analysis ($80 < P < 320$ GeV/c) the value is $R_\mu = 1.396 \pm 0.037$ where the error is only statistical.

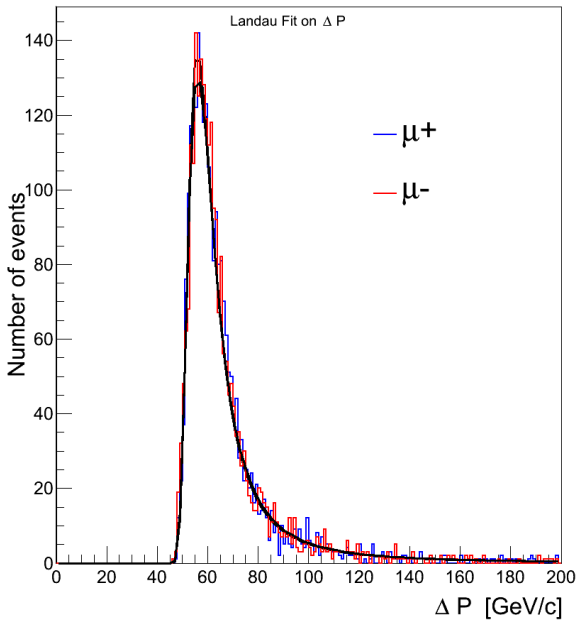

Figure 6.6: Momentum loss for muons generated at surface level with zenith angle 77^o and $P = 200$ GeV/c with the curve obtained by fitting the points with a Landau distribution.

6.3.2.2 Corrections for momentum resolution, efficiency and charge mis-assignment

As in the case of the vertical muons we have to study the effect of the migration of the entries in the momentum bins due to momentum resolution. At this purpose the muons simulated at fixed energies at surface, as discussed in the previous sections, have been detected and reconstructed with the same off-line programs adopted for real events. These simulated events have been analysed to obtain for both the muon charge : the momentum resolution, the efficiency and the charge mis-assignment in the whole range of our studies ($80 < P < 320$ GeV/c).

In Fig. 6.10 the resolutions are given for μ^+ and μ^- for the 7 fixed momenta, in the whole range of our analysis the resolution is calculated by fitting these points.

We have corrected the number of positive and negative muons in each momentum bin, for the migration effect due to the resolution, with the same method employed and explained for the vertical muons. The effect of this correction in the measurement of the ratio is very low as we can see in Fig. 6.11.

The efficiency in the muon detection has been evaluated, at fixed energy, for each zenith angle, as an example in Fig. 6.12 is given the efficiency for μ^+ and μ^- with $P = 200$ GeV/c. The efficiency is low for zenith angle about 70^o in which the

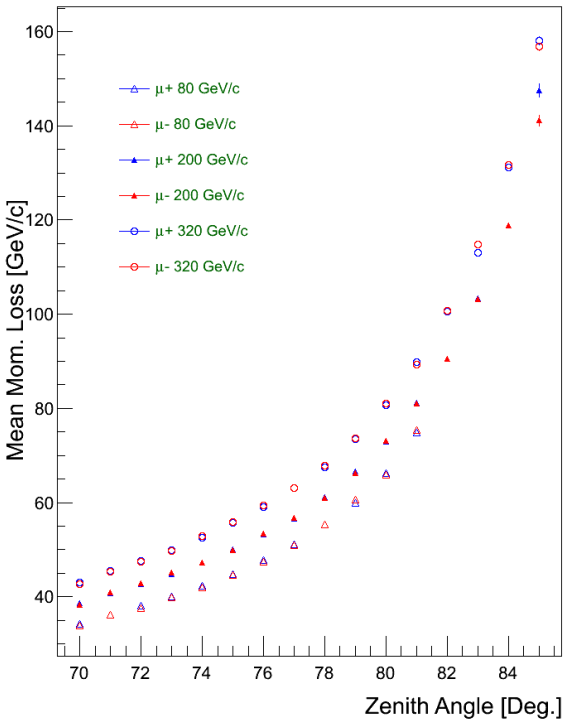

Figure 6.7: Mean momentum loss as a function of the zentih angle for 3 fixed energies.

muons arrive in the apparatus with a not large inclination, and more easily can miss to hit one of the chambers, while the low efficiency at high zenith angles is due to the large energy loss along the way.

The charge mis-assignment has been estimated from the same simulations for each fixed energy summing and averaging the contribution of all the zenith angle. In our range of momentum it is found negligible, but in the Monte Carlo the misalignment of the chambers could be underestimated inducing a low estimation of charge mis-assignment for high momentum muons. This effect will be keep into account in the evaluation of the systematic errors.

The final results of the ratio $R_\mu(\mu^+/\mu^-)$ at surface level for near-horizontal muons with all the corrections is given in Fig 6.13 and summarized in Tab. 6.2. In the range $80 < P < 320$ GeV/c the value is : $R_\mu = 1.27 \pm 0.04$ where the error is only statistical.

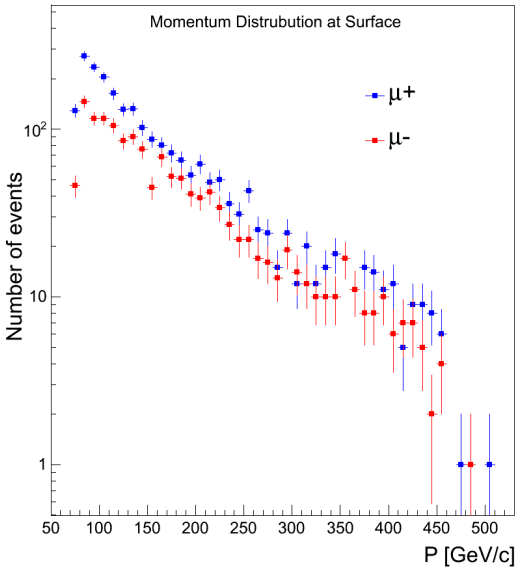

Figure 6.8: Momentum distribution at surface level for $\mu^{\pm}$.

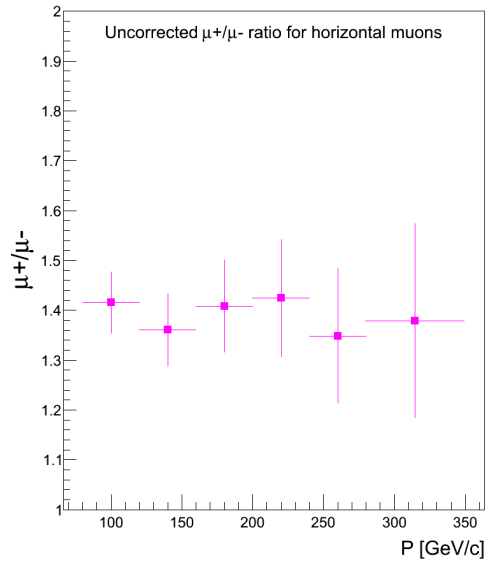

Figure 6.9: Uncorrected μ^+/μ^- ratio for near horizontal muons at surface level.

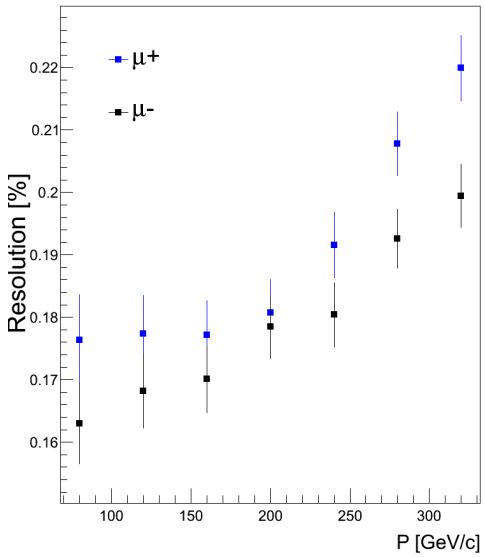

Figure 6.10: Momentum resolution for μ^+ and μ^- measured at surface.

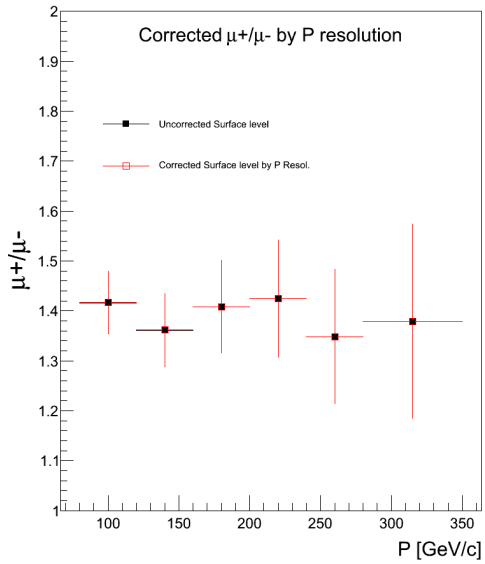

Figure 6.11: μ^+/μ^- ratio corrected for the migration effect and comparison with the uncorrected ratio for near horizontal muons at surface level.

6.3.3 Estimate of the systematic uncertainties and final results

As in the case of vertical muons the systematic uncertainties in the ratio can arise to all possible effects that give an asymmetry in the detection between μ^+ and μ^-.

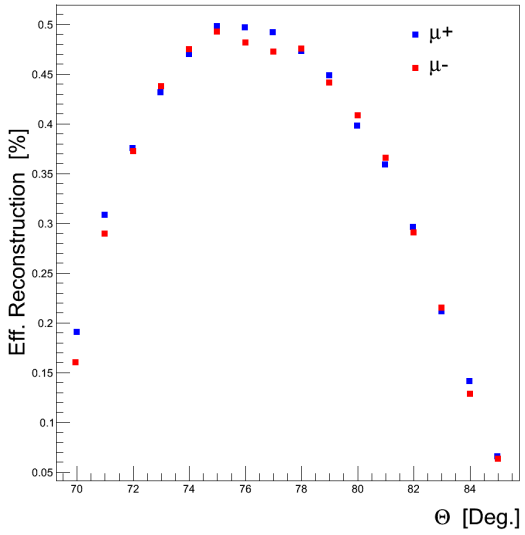

Figure 6.12: μ^+ and μ^- efficiencies as a function of the zenith angle for fixed momentum $P = 200$ GeV/c.

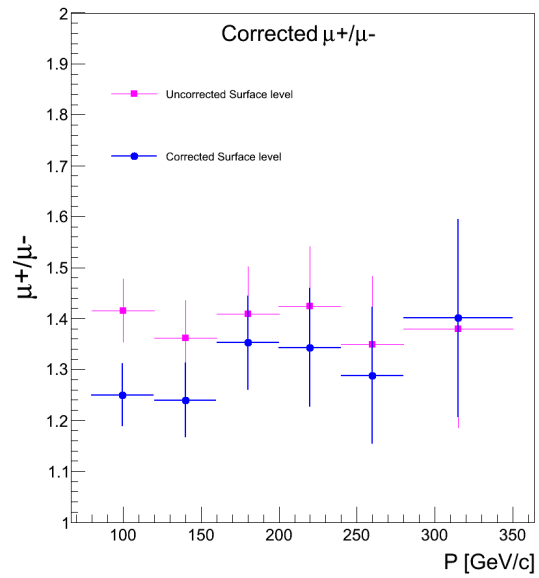

Figure 6.13: Comparison between corrected and uncorrected μ^+/μ^- ratio as a function of the momentum.

The range of momentum of our measure has been chosen to minimize the

	P[GeV/c]	80-120	120-160	160-200	200-240	240-280	280-320
Uncorrected	R_{μ^+,μ^-}	1.416	1.361	1.409	1.423	1.348	1.396
Corrected	R_{μ^+,μ^-}	1.249	1.239	1.352	1.343	1.288	1.401
Eff.	ε_{μ^+}	0.177	0.278	0.386	0.456	0.503	0.521
Eff.	ε_{μ^-}	0.156	0.253	0.370	0.431	0.480	0.530

Table 6.2: Summary of the main results for each momentum interval

systematic uncertainties. The cut $P > 80$ GeV/c removes the difficult corrections coming from the detection inefficiencies at low momentum, source of errors in counting the ratio. At high momentum a possible underestimation of the misalignment of the muons chambers affects the estimate of the the charge mis-assignment.

Adopting the same procedure as for the vertical muons, the evaluation on the systematic errors has been obtained by calculating the ratio at each extreme of the energy bin and comparing these values with the final results given in the previous section. The misalignment of the chambers have been supposed to give a charge mis-assignment of 5% in all the bins. The systematic errors are calculated from the difference between the ratio obtained by evaluating the momentum resolution, the efficiencies and the charge mis-assignment at lower limit of the bin and the ratio in the center of the bin (final value). In Table 6.3 are summarized the results of the ratio calculated with the simulation quantities taken from the upper and lower limit of the momentum bins.

	P[GeV/c]	80-120	120-160	160-200	200-240	240-280	280-320
Upper limit	R_{μ^+,μ^-}	1.228	1.210	1.356	1.191	1.285	1.319
Lower limit	R_{μ^+,μ^-}	1.177	1.184	1.247	1.322	1.140	1.308
Eff.	ε_{μ^+}	0.177	0.278	0.386	0.456	0.503	0.521
Eff.	ε_{μ^-}	0.156	0.253	0.370	0.431	0.480	0.530
$[Mis-ass]$	q_{μ^+}	0.05	0.05	0.05	0.05	0.05	0.05
$[Mis-ass]$	q_{μ^-}	0.05	0.05	0.05	0.05	0.05	0.05

Table 6.3: Summary of the main results for each momentum interval taken the upper and lower limit of the bin momentum

The final results of the ratio $R_\mu(\mu^+/\mu^-)$ at surface level with statistical and systematic errors is given in Table 6.4, and shown in Fig 6.14, the total errors are calculated adding in quadrature the statistical and the systematic errors.

The value $R_\mu(\mu^+/\mu^-)$ in the whole range $80 < P < 320$ GeV/c is : $R_\mu = 1.27 \pm 0.04 \pm 0.1$.

The large systematic error is mainly due to the uncertainties in the estimation of the muon chamber misalignments.

P[GeV/c]	R_{μ^+/μ^-}	R_{μ^+/μ^-}
80-120	1.249±0.062(stat.)±0.07(syst.)	1.249±0.094(tot.)
120-160	1.239±0.073(stat.)±0.06(syst.)	1.239±0.094(tot.)
160-200	1.352±0.093(stat.)±0.1(syst.)	1.352±0.136(tot.)
200-240	1.343±0.117(stat.)±0.1(syst.)	1.343±0.154(tot.)
240-280	1.288±0.134(stat.)±0.1(syst.)	1.288±0.167(tot.)
280-320	1.401±0.194(stat.)±0.1(syst.)	1.401±0.218(tot.)
80-320	1.27±0.04(stat.)±0.10(syst.)	1.27±0.10(tot.)

Table 6.4: Final results of the $R_\mu(\mu^+/\mu^-)$ ratio for each momentum bin

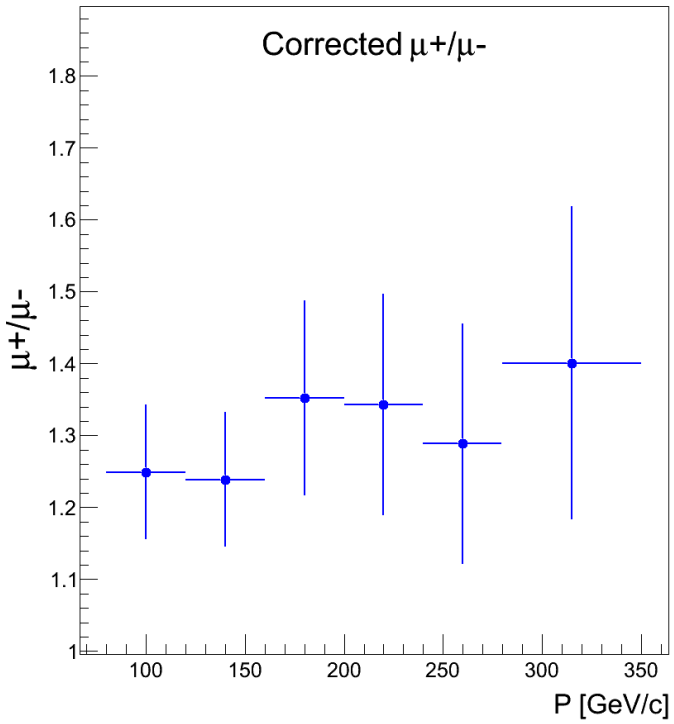

Figure 6.14: Final result of the corrected μ^+/μ^- ratio as a function of the momentum at surface level with the total error (statistic and systematic).

Chapter 7

Summary & Conclusions

Contents

In this thesis we have analysed the atmospheric muon data collected during Summer 2009 and February 2010 with various sub-detectors of ALICE experiment, mainly to study the muon charge ratio $R_\mu(\mu^+/\mu^-)$ for *near-vertical muons* and *near-horizontal muons*.

7.1 Near-vertical muons

In Chapter 5 the analysis of the *near-vertical muons* has been presented. The central detectors of ALICE experiment employed are : ACORDE (Alice Cosmic Ray Detector), TOF (Time of Flight), SPD (Silicon Pixel Detector) for the trigger, and TPC (Time Projection Chamber) for the muon tracking. Although, TPC was designed for the tracking of the particles coming from the collision point, it has been employed for the atmospheric muons, which have a different topology, adapting the reconstruction programs with ad hoc algorithms for them.

By using these new reconstruction algorithms it was possible to achieve the muon multiplicity distribution also for events with very high multiplicity. Although the short live time of the data taken ($\sim$ 2.5 days) makes difficult to perform studies concerning composition, the data sample was compared with Monte Carlo simulations done to predict the muon multiplicities in ALICE, considering pure iron and pure proton primary, for 30 days of data taking. We have seen that 2009 data have a standard behaviour with respect the expectation, while February 2010 data reports two events with a very high multiplicity : 89 muons which gives a local density of $\sim 6\mu/m^2$ and 182 muons with a local density of $\sim 12\mu/m^2$. We have estimated, that these two events should be produced from a primary with an energy greater than 10^{16} eV, being the probability to get these kind of events very

low, about one event in three years. All these measurements were done to check the performance of the TPC for high multiplicity and also high momentum tracks, that we considered a preliminary work to start an accurate measure with the sample of single muon events.

The charge muon ratio was studied selecting the sample of single muons with two tracks in the TPC (up and down as explained in Section 4.1.1) with the trigger given by TOF (TOF Single OB3) that gives the largest number of events. Furthermore, it is required muons with zenith angles range $0^o - 20^o$ (defined here as *near-vertical muons*) to avoid those crossing the ALICE shafts (see Fig. 5.7), in such a way to get a very clear sample. The analysis is given in the momentum region $10 < P < 100$ GeV/c divided in five bins. Momentum larger than 10 GeV/c have been selected to avoid big differences in the efficiencies between μ^+ and μ^-, due to the effect of the magnetic field on the muon tracks with very low momentum, as well as to eliminate the threshold effects of the rock overburden the ALICE cavern. The upper limit of the momentum have been chosen at 100 GeV/c, because at this value the error is reasonable $\sim 30\% - 35\%$ as seen Fig. 4.10 and the migration effects of the entries from each bin to bin is very low.

Taking into account all the corrections made for the efficiency and charge mis-assignment (detailed in Section 5.5.1) to get a corrected value of the μ^+/μ^- ratio from the raw data, as seen in Section 5.5.2 the final result, considering the statistic and systematic errors yields: $R_\mu = 1.275 \pm 0.006(stat.) \pm 0.01(syst.)$ integrated in the momentum range $10 < P < 100$ GeV/c.

Systematic uncertainties have been estimated considering all possible sources of asymmetries in the measurements and detections of $\mu^\pm$, like mis-alignment, acceptance, trigger inefficiencies and the uncertainties in the knowledge of the magnetic field map. Detailed studies based on Monte Carlo simulations have been performed in order to get the corrections of the main asymmetries, but these corrections could be source of systematic uncertainties.

The cut in momentum $P > 10$ GeV/c, removes most of the systematic uncertainties due to the different acceptance of $\mu^\pm$, as well as the upper cut $P < 100$ GeV/c avoids the systematic uncertainties due to mis-alignment of the tracking detector. An estimation of the systematic uncertainties has been given in two steps: in the first step, the corrections for the efficiencies and mis-assignment were calculated considering the lower limits of each momentum bin, in the second step with the upper limits (see Section 5.5.2).

7.1.1 Comparison with other measurements

Since the muon charge ratio measurement presented in this thesis was obtained considering the low momentum region, hence the final results will be compared

taking into account the momentum region $P < 100$ GeV/c.

The most significant results were obtained by L3+C collaboration which published the value 1.285±0.003(stat.)±0.019(syst.) [Archard 2004], and a more recent and accurate measurement repoted by CMS (Compact Muon Solenoid) experiment, with the charge ratio value of 1.2766±0.0032(stat.)±0.0032(syst.) considering six P bins for $P < 100$ GeV/c [CMS-Collaboration 2010]. In Fig 7.1 are shown the results of the present study together with L3+C collaboration and CMS collaboration results. We can see that our results are in good agreement with the two quoted experiments in the region $P < 100$ GeV/c.

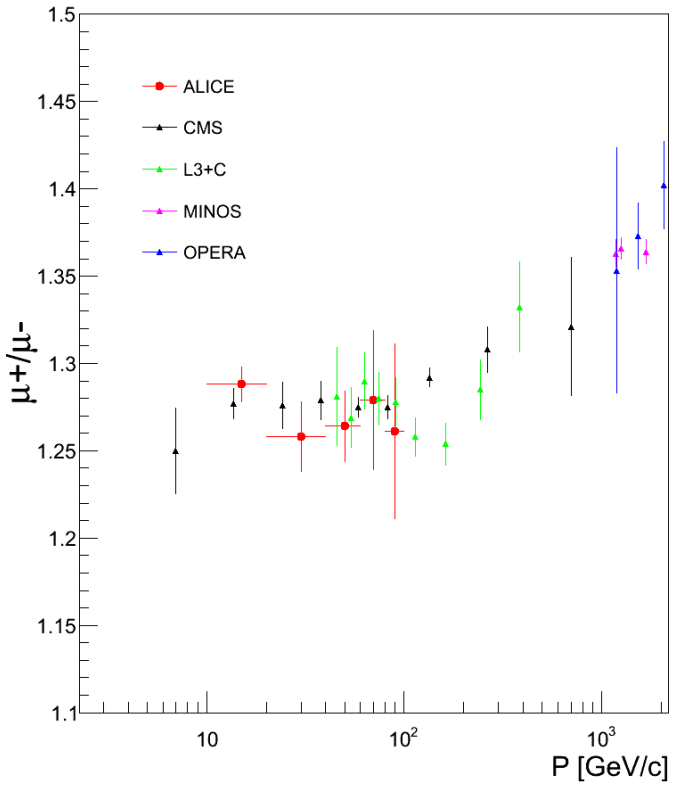

Figure 7.1: Comparison of the μ^+/μ^- ratio measurement with other experiments.

7.2 Near-horizontal muons

In Chapter 6 is presented the analysis of the *near-horizontal muons* for a preliminary measurement of the charge muon ratio. For this purpose, the data collected by the Forward Muon Spectrometer (FMS) during the Summer 2009, which concern

about 9 live days of data taking, have been analyzed.

Although, the FMS was optimized for forward muons coming mainly from meson decays produced by heavy ion collisions, it becomes a detector with excellent capabilities to detect high energy atmospheric muons with large zenith angles (defined here as *near-horizontal muons*) within the range $70^o - 90^o$ as seen in Chapter 6. In addition, due the big dipole magnet located between the second and fourth station, which produces a magnetic field of 0.7 T, it makes possible to perform precise high momentum measurements. We have estimated a momentum resolution at 100 GeV/c of about 18% (see Fig. 4.12) a factor two better than for vertical muons in the central barrel.

In this analysis only single muons crossing the whole FMS, that is at least nine hits in the ten planes of the five tracking stations, are used. A low momentum cut of $P < 10$ GeV/c at ALICE level has been done to remove asymmetries in the detection of positive and negative muons due to large curvature of low momentum tracks in the magnetic field. These stringent selections assure a good evaluation of the observables, fundamental to measure the ratio in a large momentum range.

Accurate studies of the $\mu^{\pm}$ energy loss in rock as well as their efficiencies, charge mis-assignment have been performed with Monte Carlo simulations. The systematic errors have been estimated supposing mis-alignment of the tracking chambers as the main source and giving an evaluation of the ratio changing the momentum resolution and the efficiencies for each bin.

The μ^+/μ^- ratio for *near-horizontal muons* reported in this thesis is given in the momentum region at surface $80 < P < 320$ GeV/c divided in 6 bins of $\Delta P = 40$ GeV/c.

The final value in the whole interval is $R_\mu = 1.27 \pm 0.04(stat.) \pm 0.1(syst.)$

7.2.1 Comparison with other measurements

The experiments, MUTRON and DEIS-Spectrometer dedicated to study the muon charge ratio in the horizontal direction have been considered for the comparison with our results in the momentum interval corresponding to present study (see Fig 7.2). The value reported by MUTRON in the momentum region $100 < P < 600$ GeV/c within zenith angles 86^o - 90^o was $R_\mu = 1.251 \pm 0.005(stat.)$ [Matsuno 1984] while for DEIS was $R_\mu = 1.25$ [Allkofer 1979] within zenith angles 78^o - 90^o.

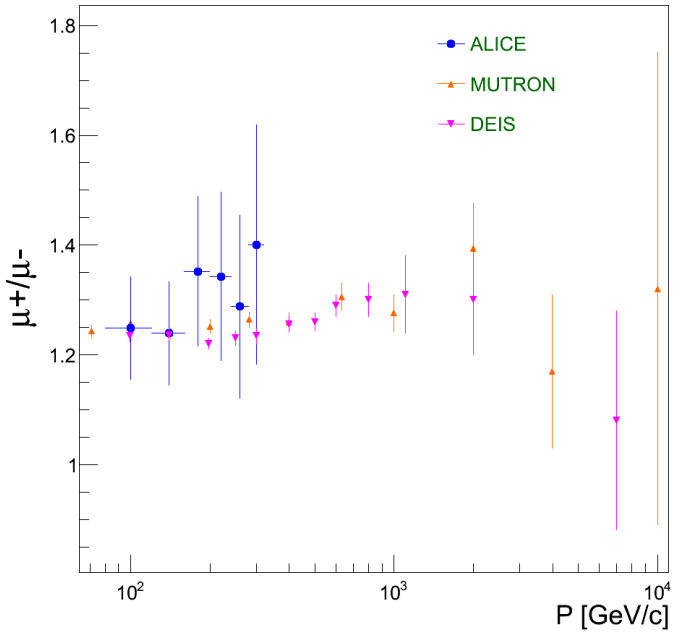

Figure 7.2: Comparison of our μ^+/μ^- measurement with MUTRON (1984) and DEIS (1979) experiments.

7.3 Conclusions

The measurement of the ratio $R_\mu(\mu^+/\mu^-)$ performed with the ALICE central barrel detectors for *near-vertical muons* and with the FMS for *near-horizontal muons* are in good agreement with all the previous measurements done by the experiments CMS and L3+C for vertical and MUTRON, DEIS for horizontal direction.

It is clear that our measurements have to be considered preliminaries for three main reasons :

- The events collected correspond to 2.5 days for vertical muons compared with around 30-40 days for the quoted experiments, while for horizontal muons (9 days) we have a factor 30 less events than MUTRON. Therefore the statistics has to be increased a lot if we want to be competitive with these experiments.

- The data have been taken during commissioning and did not have a level of calibration and alignment of the detectors comparable with nowdays.

- The data was taken always with the same polarity of the two magnetic fields, while it is possible and necessary to reverse the polarity to decrease the systematic uncertainties in the ratio measurement.

The first point decreases the statistical errors while the other two are fundamental to decrease the systematic errors. In spite of all these improvements that should be do in the future, with this work we have demonstrated that accurate measurements in the cosmic ray physics can be preformed with the ALICE experiment. In particular the situation is evolving and new cosmic data taking are planned during 2011 and following years. These new data allow a more accurate measure of the ratio and to touch other topics connecting with cosmic ray physics and hadron interactions at very high energies.

Appendix A

ALICE Coordinate System

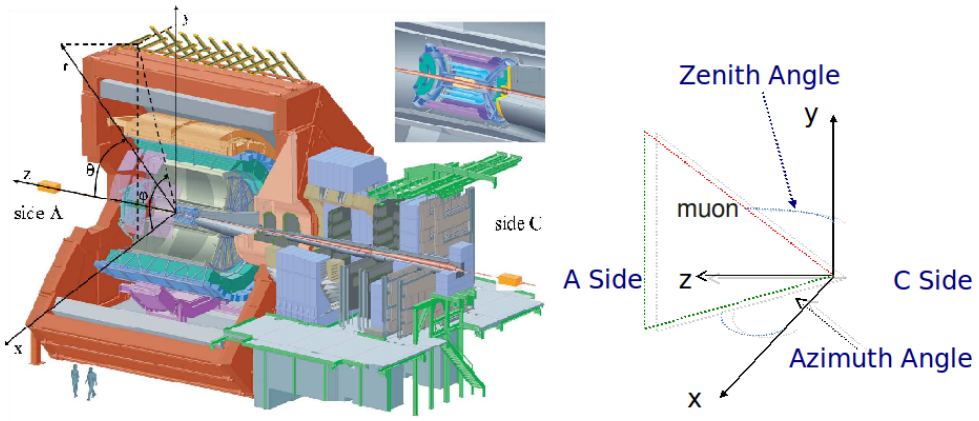

Figure A.1: A schematic view of the ALICE global coordinate system on the rigth for the cosmic rays case.

ALICE has a global and local coordinate systems. The global coordinate system is a right-handed orthogonal cartesian system with the origin et the beam interaction point. The parameters are defined as:

- **x axis** is lying in the local horizontal accelerator plane, perpendicular to the mean local beam direction and pointing towards the center of the LHC ring. The side with positive x values (from the point of origin towards the accelerator center) is labeled as Inside (I), the oppsite as Outside (O);
- **y axis** is perpendicular (vertical) to the x axis and the mean local beam direction, pointing upward;
- **z axis** is parallel to the mean local beam direction, pointing towards the side A. The muon arm is at negative z (side C);
- **azimuthal angle** ϕ increases counter-clockwise from $x(\phi = 0)$ to $(\phi = \pi/2)$ to $x(\phi = 2\pi)$ with the observer looking from side A towards C;
- **polar angle** θ increases from $(\theta = 0)$ to xy plane $(\theta = \pi/2)$ to $-z(\theta = \pi)$

Due to the azimuthal segmentation of the central tracking detectors (ITS. TPC, and TRD) the reconstruction software uses a local coordinate system related to a given sub-detector (TPC sector, ITS module, etc.). Therefore the local and global systems can be transformed into other by a simple rotation of the angle α around the z axis.

A.1 Coordinate system for cosmic rays

Cosmic rays coordinate system is based in ALICE global coordinate system. Therefore, xyz axis are the same described above, but we have a transformation for azimuthal and polar angles ϕ, θ, and are described as follows:

- **Zenithal angle** θ_c increases from ($\theta_c = 0$) in the xy plane to ($\theta_c = \pi/2$);
- **Azimuthal angle** ϕ_c increases clockwise from $x(\phi_c = 0)$ to ($\phi_c = \pi/2$) to $x(\phi_c = 2\pi)$ with the observer looking from side C towards A

A sketch of the golabal coordinate system for both cases are given in the Fig. A.1

Bibliography

[Abbasi 2008] R. Abbasi. *et. al.*, HiRes Collab., Phys. Rev. Lett., vol. 10101, no. 100, 2008. 2

[Abdallah 2007] J. Abdallah. *et. al.*, Astropart. Phys. *Study of multi-muon bundles in cosmic ray showers detected with the DELPHI detector at LEP*, no. 28, pages 273–286, 2007. 62

[Abraham 2008] J. Abraham. *et. al.*, Pier-Auger Collab., Phys. Rev. Lett., vol. 061101, no. 101, 2008. 2

[Abu-Zayyad 2000] T. Abu-Zayyad. *et. al.*, HiRes-MIA Collab., Phys. Rev. Lett., no. 84, page 4276, 2000. 2

[Abu-Zayyad 2001] T. Abu-Zayyad. *et. al.*, HiRes-MIA Collab., Astrophys. J., no. 557, pages 689–699, 2001. 2

[Adamson 2007] P. Adamson. *et. al.*, (MINOS Collaboration), Phys. Rev., vol. D76, no. 052003, 2007. 8

[Adir 1977] Adir. *et.al.*, Phys. Rev. Lett., no. 39, page 467, 1977. 9

[Adriani 2002] O. Adriani. *et.al.*, Nucl. Instrum. Meth. *L3+C detector, a unique tool-set to study cosmic rays*, no. A488, page 209, 2002. 34

[Aglietta 1995] M. Aglietta. *et. al.*, (LVD Collaboration), Astropart. Phys., vol. 3, no. 311, 1995. 12

[Ahn 2003] H.S. Ahn. *et. al.*, ATIC Collab. in: Proc. of 28th Int. Cosmic Ray Conf., Tsukuba, page 853, 2003. 2

[Akindinov 2004] A. Akindinov. *et.al.*, Eur. J. Phys. *Particle identification with the ALICE TOF detector at very high particle multiplicity*, no. C32, page s165, 2004. 31

[Akindinov 2006] A. Akindinov. *et.al.*, Eur. J. Phys. *Study of QGP signatures with the $\phi \to K^+K^-$ signal in Pb-Pb ALICE events*, no. C45, page 669, 2006. 31

[Alessandro 2006] B. Alessandro. *et.al.*, J. Phys. *ALICE: physics performance report, volume II*, no. G32, page 1295, 2006. 31, 34

[Allkofer 1979] O.C. Allkofer. *et.al.*, ICRC, 1979. 94

[Allkofer 1985] Allkofer. *et.al.*, Nucl. Phys., no. 1, page B259, 1985. 10

[Alvarez 2002] J. Alvarez. *et.al.*, Phys. Rev. D, no. 66, 2002. 5

[Amenomori 2008] A. Amenomori. *et. al.*, Tibet ASγ Collab. Astrophys. J., no. 678, pages 1165–1179, 2008. 2

[Amsler 2001] C. Amsler. *et. al.*, Phys. Lett. B *(Standard rock is described in section 24.4 on p. 256)*, no. 667, pages 1–5, 2001. 9

[Antoni 2005] T. Antoni. *et. al.*, KASKADE Collab. Astropart. Phys., no. 24, pages 1–25, 2005. 2

[Archard 2004] P. Archard. *et. al.*, (L3+C Collaboration), Phys. Lett., vol. B598, no. 15, 2004. 7, 12, 20, 22, 93

[Arteaga-Velazques 2008] J.C. Arteaga-Velazques. *et. al.*, KASKADE-Grande Collab. in: Proc. of 15th Int. *Symposium on Very High-Energy Cosmic Ray Interactions, Paris*, 2008. 2

[Avati 2003] V. Avati. *et. al.*, Astropart. Phys. *Cosmic multi-muon events observed in the underground CERN-LEP tunnel with the ALEPH experiment*, no. 19, pages 513–523, 2003. 15, 16, 62

[Ayre 1975] C.A. Ayre. *et. al.*, J. Phys., vol. G1, no. 584, 1975. 7

[Bellotti 1996] R. Bellotti. *et. al.*, Phys. Rev., vol. D53, no. 35, 1996. 5

[Bellotti 1999] R. Bellotti. *et. al.*, Phys. Rev., vol. D60, no. 052002, 1999. 5

[Beuermann 1968] K.P. Beuermann and G. Wibberenz. Can. J. Phys., vol. 46, no. S1034, 1968. 6

[Blümer 2009] Johannes Blümer. *et. al.*, *Progress in Particle and Nuclear Physics.*, no. 63, pages 293–338, 2009. 2, 3

[Boezio 2000] M. Boezio. *et. al.*, Phys. Rev., vol. D62, no. 032007, 2000. 5

[Carminati 2004] F. Carminati. *et.al.*, J. Phys. *Technical proposal for a Large Ion Collider Experiment at the CERN LHC*, no. G30, page 1517, 2004. 34

[C.Gabaratos 2004] C.Gabaratos. *Nucl. Instrum. Meth. The ALICE TPC*, no. A 535, page 197, 2004. 30

[Chabratova 2003a] G. Chabratova. *et.al.*, Alice Internal Note *Development of the Kalaman filter for tracking in the forward muon spectrometer of ALICE*, no. ALICE-INT-002, 2003. 37, 46

[Chabratova 2003b] G. Chabratova. *et.al.*, ALICE internal note *Further development of the Kalman filter for the muon spectrometer of ALICE and its comparision with the default method*, no. 053, 2003. 46, 47

[CMS-Collaboration 2010] CMS-Collaboration. **arXiv:1005.5332v1 [hep-ex 28 May]**, 2010. 20, 21, 93

[Collaboration 1995] ALICE Collaboration. *et.al.*, CERN-LHCC *Technical proposal for a Large Ion Collider Experiment at the CERN LHC*, no. 71, 1995. 31

[Costa 2001] C.G.S. Costa. Astropart. Phys., vol. 16, no. 193, 2001. 8

[Courtat 2004] P. Courtat. *et.al.*, Alice Internal Note *The electronics of ALICE dimuon tracking chambers*, no. ALICE-INT-026, 2004. 40

[Coutu 2000] S. Coutu. *et. al.*, Phys. Rev., vol. D62, no. 032001, 2000. 5

[Daniel 1974] R.R. Daniel and S.A. Stephens. Revs. Geophysics & Space Sci., vol. 12, no. 233, 1974. 6

[Derbina 2005] V. Derbina. *et. al.*, Astrophys. J., no. 628, page 141, 2005. 2

[D.Heek 1998] D.Heek. *et.al.*, Report FZKA 6019, Forschungszentrum Karlsruhe, *A Monte Carlo to Simulate EAS*, 1998. 62

[Diggory 1974] I.S. Diggory. *et. al.*, J. Phys., vol. A7, no. 741, 1974. 6

[D.Zimmermann 2004] D.Zimmermann. *et.al.*, Nucl. Inst. Meth. Phys. Res. A, no. 141, page 525, 2004. 17

[Fernandez 2007] A. Fernandez. *et.al.*, Nucl. Instrum. Meth. *ACORDE a cosmic ray detector for ALICE*, no. A572, page 102, 2007. 34

[Frankenfeld 2002] U. Frankenfeld. *et.al.*, Alice Internal Note *The ALICE TPC inner readout chamber: results of beam and laser tests*, no. ALICE-INT-030, 2002. 30

[Gaisser 1990] T.K. Gaisser. *Cosmic Rays and Particle Physics Cambridge University.* 1990. 6

[Gaisser 2007] T.K. Gaisser. *and T. Stanev Bartol Research Inst. Univ. Delawere,* Cosmic Rays Review. 2007. 3, 5, 7

[G.K.Ashley 1975] G.K.Ashley. *et.al.*, Phys. Rev. D 12, no. 1, page 20, 1975. 12, 22

[Gluckstern 1963] R. L. Gluckstern. Nucl. Instrum. Methods, no. 24, page 381, 1963. 48

[Grieder 2001] P.K.F. Grieder. *Cosmic Rays at Earth.* Elsevier Science, 2001. 6, 7

[Grigorov 1970] N.L Grigorov. *et. al.*, Yad. Fiz., no. 11, page 1058, 1970. 2

[Grigoryan 2002] S. Grigoryan. *et.al.*, Alice Internal Note *Contribution of Secondary Pi/K Mesons, produced in the Absorber, into the Dimuon Background in Pb-Pb Collisions*, no. ALICE-INT-06, 2002. 37

[Groom 2001] D.E. Groom. *et. al.*, Data Nucl. Tables *Muon Stopping power and range tables*, no. 78, 2001. 9

[Haino 1999] S. Haino. *et. al.*, (BESS Collaboration), Phys. Lett., vol. B594, no. 35, 1999. 7

[Hayakawa 1969] S. Hayakawa. *Cosmic Rays Physics*, Wiley, Interscience, New York, 1969. 6

[Hebbeker 2002] T. Hebbeker. and C. Timmermans, Astropart. Phys., no. 18, page 107, 2002. 17

[Heitler 1944] W. Heitler. 1944. 4

[H.Stelzer 2003] H.Stelzer. *et.al.*, Alice Internal Note *The ALICE TPC readout chamber: from prototypes to series production*, no. ALICE-INT-017, 2003. 30

[Jokisch 1979] H. Jokisch. *et. al.*, Phys. Rev., vol. D19, no. 1368, 1979. 7

[J.Wiechula 2005] J.Wiechula. *et.al.*, *Nucl. Instrum. Meth. High-precision measuremtn of the electron drift velocity in* $Ne - CO_2$, no. A 548, page 582, 2005. 30

[Kremer 1999] J. Kremer. *et. al.*, Phys. Rev. Lett., vol. 83, no. 4241, 1999. 7

[L3Collaboration 2004] L3Collaboration. Phys. Lett. B, no. 598, pages 15–32, 2004. 18, 19, 20

[Lipari 1993] P. Lipari. Astropart. Phys., vol. 1, no. 195, 1993. 6

[M.Ambrosio 1999] M.Ambrosio. *et.al.*, Astropart. Phys., no. 10, page 11, 1999. 10

[Matsuno 1984] S. Matsuno. *et.al.*, Phys. Rev. D, vol. 29, no. 1, 1984. 94

[Matthews 2005] J. Matthews. *et.al.*, Astropart. Phys., no. 22, pages 387–397, 2005. 4

[MINOS-Collaboration 2007] MINOS-Collaboration. *Measurement of the atmospheric muon charge ratio at TEV energies with MINOS*, Phys. Rev. D **arXiv:0705.3815**, no. 76, 2007. 12, 22

[N.Agafonova 2010] N.Agafonova. *et.al.*, *Measurement of the atmospheric muon ratio with the OPERA detector*, Eur. Phys. J. C **arXiv:1003.1907v1**, no. 67, page 25, 2010. 12, 22

[Nagano 1984] M. Nagano. *et. al.*, J. Phys. G, no. 10, page 1295, 1984. 2

[N.N.Kalmykov 1989] N.N.Kalmykov. *et.al.*, Sov. J. Nucl. Phys., no. 50, pages 315–318, 1989. 62

[O.C. Allkofer 1971] K. Carstensen O.C. Allkofer and W.D. Dau. Phys. Lett., vol. B36, no. 495, 1971. 7

[P.Adamson 2010] P.Adamson. *et.al.*,**arXiv:0805.2545 [hep-ex 30 Dec]**, 2010. 11

[Pascale 1993] M.P. De Pascale. *et. al.*, J. Geophys. Res., vol. 98, no. 3501, 1993. 7

[Peyré 1998] J. Peyré and J. Pouthas. Alice Internal Note *A full-scale prototype for the tracking chambers of the ALICE muon spectrometer. Part I: mechanichs, anode and cathode plane design, assambly and construction*, no. ALICE-INT-28, 1998. 37

[Pillot 2005] P. Pillot. *et.al.*, Alice Internal Note *The geometry monitoring system of ALICE dimuon spectrometer simulation results*, no. ALICE-INT-020, 2005. 39

[P.Lipari 1991] P.Lipari and T. Stanev. Phys. Rev., vol. D44, no. 3613, 1991. 8

[P.Lipari 2000] P.Lipari. Astropart. Phys., no. 14, page 171, 2000. 10

[Rastin 1984] B.C. Rastin. J. Phys., vol. G10, no. 1609, 1984. 7

[Rimai 1997] A. Rimai. *et.al.*, Alice Internal Note *Spatial resolution studies in cathode pad and in cathode strip chambers*, no. ALICE-INT-23, 1997. 37

[Sanuki 2007] T. Sanuki. *et. al.*, Phys. Rev., vol. D75, no. 043005, 2007. 6

[Schreiner 2009] P.A. Schreiner. *et. al.*, Astropart. Phys. *Interpretationof the undreground muon charge ratio*, no. 32, pages 61–71, 2009. 11

[Tieulent 2005] R. Tieulent. *et.al.*, Alice Internal Note *The geometry monitoring system of the ALICE dimuon spectrometer overview*, no. ALICE-INT-009, 2005. 39

[W. Blum 2008] W. Riegler W. Blum and L. Rolandi. *Particle Detection with Drift Chambers*, page 448, 2008. 48

[Wurzinger 1997] A. Wurzinger. *et.al.*, Alice Internal Note *Monte Carlo studies on cathode strip/pad chambers for the ALICE di-muon arm*, no. ALICE-INT-10, 1997. 37

[Zintchenko 2003] A. Zintchenko. *et.al.*, Alice Internal Note *A new approach to cluster finding and hit reconstruction in muon chambers of ALICE*, no. ALICE-INT-006, 2003. 37